PROCESSING OF POROUS HIGH MELTING TEMPERATURE METALS

USING A REMOVABLE SECOND PHASE

Mark Taylor

January 2017

A thesis presented for the degree of
Doctor of Philosophy

Department of Materials Science and Engineering

I. ABSTRACT

The production of high melting temperature porous metals using a removable second phase has been conducted using two different methods with two different categories of second phase. The first of these is the production of a porous high temperature metal using a nickel copper alloy which has undergone solidification-induced phase separation, followed by phase removal. In this system, the removable phase is an intrinsic part of the alloy (formed as part of the microstructure during solidification) which has been removed using a ferric chloride solution. The alloy has been processed using three different solidification regimes which have in turn resulted in the production of three distinct porous structures, and pore sizes. For comparison with this method (offering different capabilities for pore and sample size, and scale up), the replication process has also been used, in which the removable phase is a secondary material extrinsic to the alloy. Significant modifications to standard processes were needed to overcome the challenges of high melting temperature metals in order for porous samples from titanium alloy (Ti-811) to be produced. An iterative experimental approach to development of replication processing has been trialed. The procedures used comprised three methods for alloy melting and two methods for applying the required infiltration pressure. The porous metal produced using this method has shown that replication casting is a possible manufacturing route, but significant hurdles are still present before a large scale porous component can be produced and tested.

II.   CONTENTS

III. TABLE OF FIGURES

IV.   TABLE OF TABLES

V. ACKNOWLEDGEMENTS

My greatest thanks go to my supervisor Dr Russell Goodall, whose boundless patience I have put to the test at times, I will be forever grateful for his advice, support and words of encouragement.

I would also like to thank all the technical and support staff of the Department of Material Science and Engineering, in particular, Mr Stuart Bater and Mr Ian Watts from the Quarrel Laboratory. Also, I wish to thank Dr Andrew Cunliffe for his help getting to grips with temperamental lab equipment.

A special appreciation goes to my D1 colleagues, whose tea runs, conversation and distractions helped the tough days seem easier.

Finally, my deepest thanks go to my close friends and family, for their much needed help and support.

I would like to dedicate this thesis in loving memory to my grandparents David and Gwen Suckling,

1   INTRODUCTION

The aim of this thesis is to investigate the current materials and methods used in the production of porous metals (metal foams), and how they may be improved and adapted to meet the needs of processing metals with higher (>1000°C) melting point. A review of the current methods and materials was first undertaken to identify areas for which further research would be beneficial.
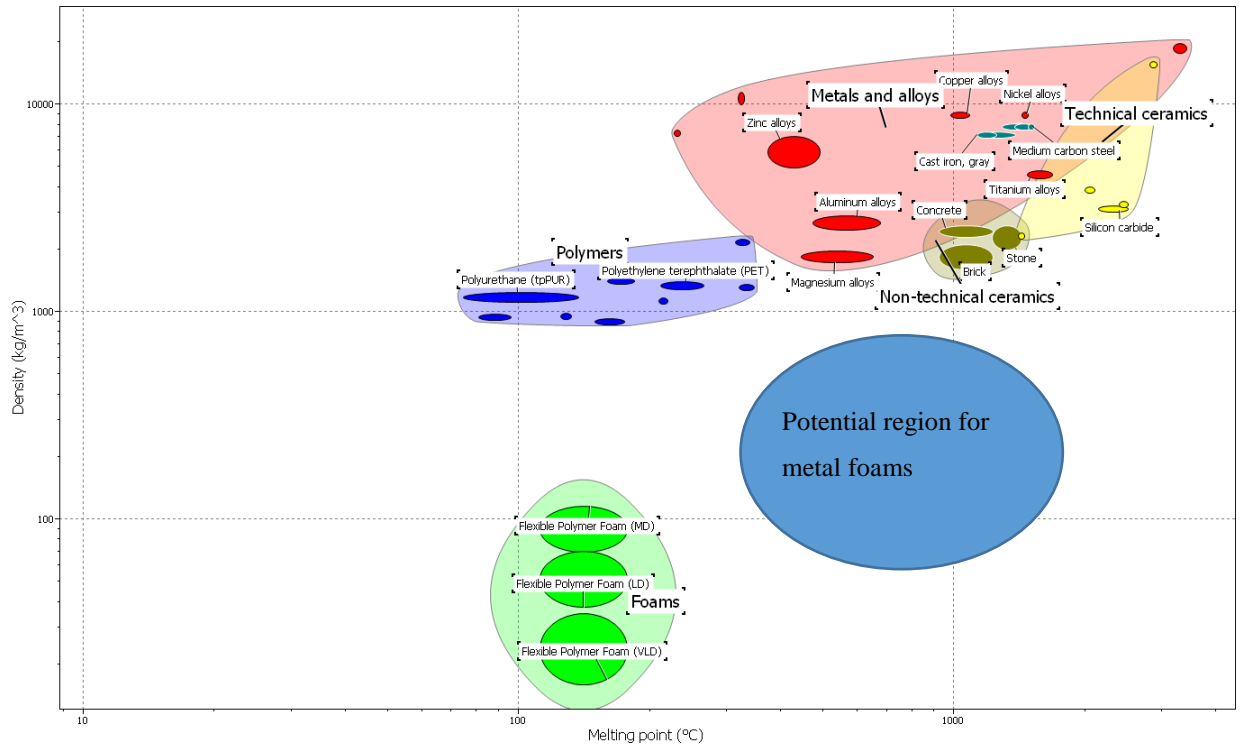
Figure 1. A graph showing the location of various engineering material on a plot of melting temperature vs density, with a representation of the potential region that metal foams could occupy, generated using CES Selector software [2].

The investigation was focused with the help of the plot of melting temperature vs density in Figure 1, the plot contains regions that depict common engineering materials broken down into the main groups of metals, polymers (with polymer foams also identified) and ceramics. A clear region is sparsely occupied where a high melting temperature material combined with a low density would fit. A small number of materials have been developed and do fit onto this region most notably aluminium, nickel and titanium alloys. The bulk of current research has been focused on the production of aluminium foams this is primarily due to the easy and relatively low cost that aluminium can be processed from the liquid state, from bubbling gas into the liquid melt to form closed porosity, through to casting the aluminium into a preform to generate open porosity, there are many processing options available and hence a large number of research areas. Nickel and titanium foam are more difficult to produce; however, nickel foams are

currently produced using electrolytic deposition methods not available for aluminium or titanium. The techniques used to process foams from titanium require the titanium to be in powder form, whether it is relatively simple partial sintering with/without a space holder or the complex using of additive manufacturing techniques.

The start of the art method for manufacturing porous metal structures from high melting temperature (>1000°C) metals is additive manufacturing; these structures are designed and topologically optimized and are often referred to as lattice structures. Lattice structures are used to provide structural support and weight reduction. The process of design and manufacture is expensive and time consuming, as such the uses are limited to those industries where cost is not main the driving factor. The aerospace and high end automotive sectors are two markets where the weight saving offered by a lattice structure can show benefits even at the high cost.

If a manufacturing route could be developed for a high melting temperature metal that resulted in a porous structure at a lower cost it would open up the market for other uses that would benefit from the additional temperature capability while also reducing the weight. Methods offering potential low cost productions routes will use already existing processing equipment and be easily adaptable for larger volumes (scale up). Casting is one such process.

To meet the aims the following objectives were set:
- Investigate current and novel porous metal manufacturing methods.
- Select at least one method which could be used directly or modified for use with a high temperature metal.
- Produce porous metal using the methods selected, and select appropriate testing methods to characterise the porous metal produced.

2　LITERATURE REVIEW

The literature review will set the current understanding of and production routes for porous metals.

2.1　Porous Metals (Metal Foams)

A porous material can be characterised as one of two distinct types, open celled and closed celled. In a closed celled foam, each cell is a distinct unit wholly surrounded by the material making up the porous structure, like a bubble, the cell will contain the gas used during the foaming process. In contrast, an open celled porous structure contains a series of struts and nodes interconnected to form a framework of the base material. Foams can also be produced at nanoscale using chemical rather than physical methods. An example of open and closed cells is shown in Figure 2.
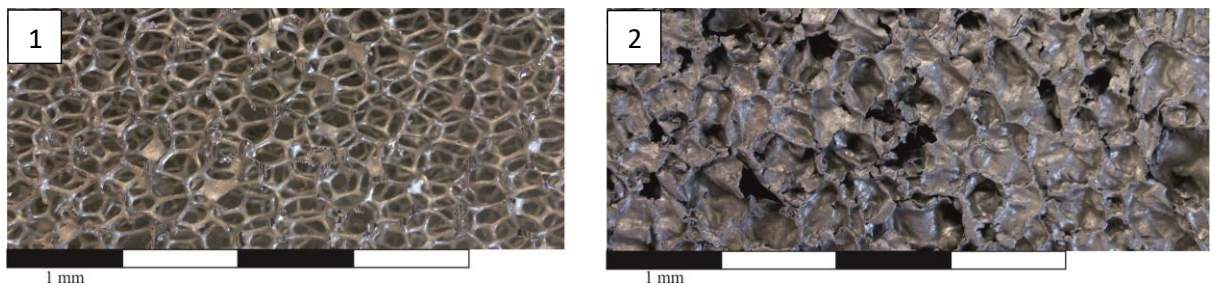
Figure 2. Photographs demonstrating the differences between open (1) and closed (2) celled foam. The open celled foam is Duocel and the closed cell is Alporas.

The difference in structure and form leads the two different cell types to find use in different areas of science and technology, with closed cellular structures focusing on the structural rather than functional advantages of foams, for example providing required mechanical properties with reduced weight when compared to a solid, with a specific example being the creation of a closed cell steel foam [3, 4]. It is possible to produce closed celled foam industrially and is commercial produced in aluminium. The disadvantage of closed celled foams is the random nature a distribution of the cells due to manufacturing process and that each cell must contain a gas to inflate it. As a result, the foam can only be used where the pressure is similar to atmosphere, otherwise the cells can be damaged. The cell walls are thin and can be damaged generating a weak point in the structure and reducing the overall strength of the foam, this type of foam is almost always used where the load is applied in compression. Consistent, inspectable and reproducible properties are difficult, with a range for properties often quoted [5].

Open celled foams have the advantage of a very large surface area to volume ratio and this leads to their use in more functional roles, although where these are combined with structural roles where weight saving is a key parameter [4, 6] they may give added advantage and value. One of these areas where the open cells are an advantage in is biological implants are the open pores allow bone etc. to grow into them [7]. The disadvantage open celled foam, as the foam porosity both size and percentage goes up the strength of the foam goes reduces, the foam structure is also random but to a lesser degree than in closed cell foams.

An advantage of both types of foam is the ability to have some level of control (this varies on manufacturing method) over the size and distribution of the pores produced. However, both types of foam can be difficult to join particularly to a solid often the foam is joined during manufacture but brazing can be used post manufacture. Once damaged neither type of foam can be repaired and inspection is difficult. A review of foam manufacturing methods follows in section 2.2.

The level of porosity, and hence density, of these materials becomes a useful performance indicator, as the density can be used to predict properties; for example Young's modulus. Both open and closed cell foams have been proposed for use as both sound absorbing and electromagnetic shielding materials [8], although experimental validation of these proposals is, as yet, limited.

The methods used to assess the level of porosity in sample vary depending on the whether the porosity is open or closed, the size of the pores expected and whether information beyond percentage porosity required. All the methods summerised in Table 1, are suitable for metal foams under the correct conditions (see comments in table).

Table 1. Methods commonly used to measure the porosity of porous metals

Method	Open or closed	Pore size range measurable	Comment
Mercury porosimetry	Open only	1 nm -10+mm	Requires whole sample to be porous and is a destructive measurement. Can only give information on pore size on density %
He pycnometry	Closed only	N/A	Test measures the volume of a sample using Boyle law, and calculates the density, if the whole sample is not porous or open pores are present incorrect values can be given.
Envelope volume	Closed only	N/A	Test measures the volume of a sample and calculates the density, if the whole sample is not porous or open pores are present incorrect values can be given.
Archimedes method	Both	N/A	Test measures the volume of a sample using the Archimedes buoyancy principle. For open celled foams the fluid (typical deionized water or ethanol) used must wet and impregnate the full depth of the pores.
Visually using computer image analysis	Both	Any	Careful preparation of the samples is required tailored to the analysis method used in order for the software to be accurate.
Visually using manual point or line counting	Both	Any	Careful preparation of the samples is required, but poor samples can be used but will have increased human error if the pore boundaries are poorly defined.

X-ray tomography while not strictly designed to directly measure density or porosity like these other techniques it can also be used for the detection and porosity within a sample [9, 10]. The technique is expensive and requires a greater level of analysis to get a result than the more conventional methods for measuring porosity.

Foams based on polymeric materials are the most widely used type of porous material, however the engineering use of polymeric foams concentrates on closed celled foams used for passive

protection, for example, from impact damage in packaging applications [11], or as thermal insulation [12, 13]. Open cell polymer foams are less commonly used, although they have some applications as sponges.

In contrast, foams based on metallic materials show some benefits over polymeric based foams. These benefits come from the use of metal as the material the foam is made from. The higher strength, higher Young's modulus and higher melting temperature that are found in most metal foams are among the most important properties which can be improved by the use of a different material to make it from, along with those properties relating to the specific behaviors of metals, such as high electrical and thermal conductivity.
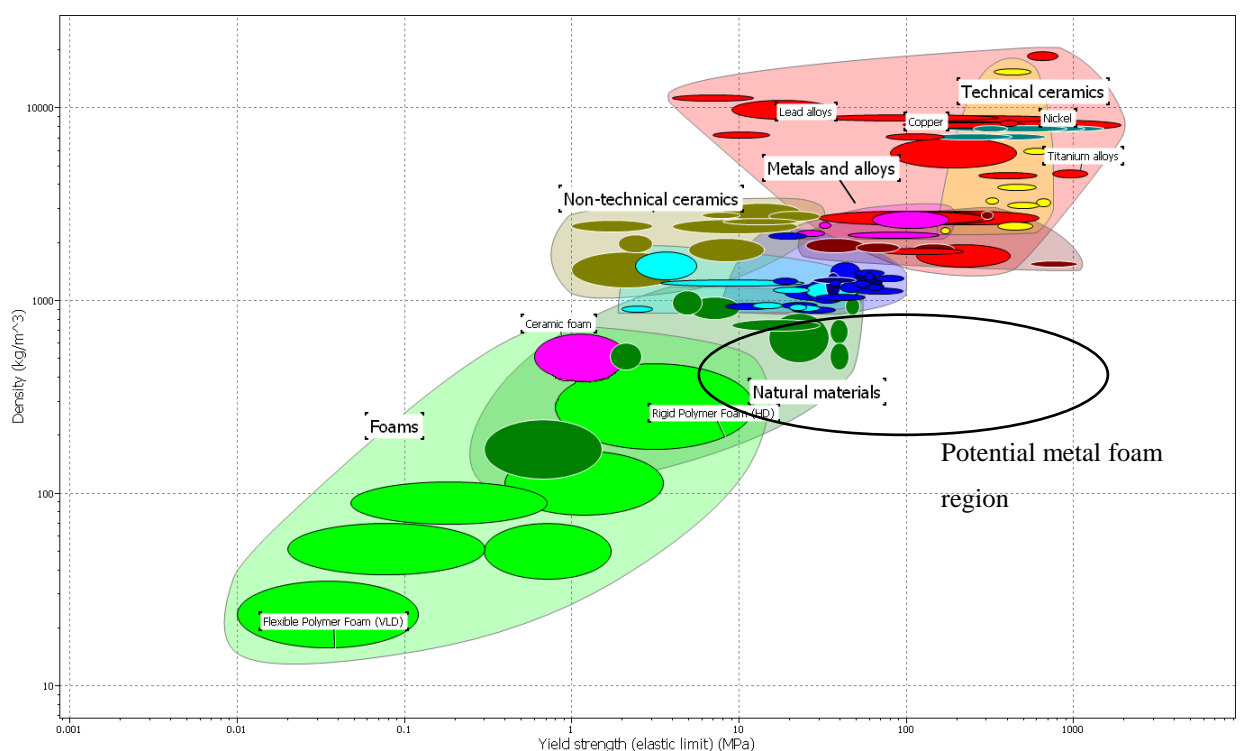
Figure 3. A graph showing the location of a range of engineering materials on a plot of yield strength vs density, with a representation of the region of the graph that metal foams could occupy [2].

It is clear from Figure 1 and 3, that metallic foams are placed in a region of the plots previously unoccupied, resulting in a new class of materials with a combination of properties which have not been available to engineers previously. These combinations, such as low density and relatively high stiffness while retaining strength have made the use of foam structures of aluminium relatively widespread (if still involving only low volumes of material), particularly as sandwich structures, which have found their way into most sectors from aerospace to automotive [14], for example as crash energy absorbing structures in cars [6]. Specifically aluminum foam

technology is a good starting point when discussing metallic foams, not only because it is the most highly developed form of metallic foam, finding use in practical applications, but also because aluminum foams can be produced using the widest range of techniques, with good control over the final macro/meso-structure. However this advantage is also the biggest limitation of aluminum; the reason behind the ease of production and high level of control is down to the relatively low melting point of aluminum (660°C). As metals with higher melting temperature are required for some applications (for example those where the material will be exposed to high temperature environments), the techniques which are simple and cheap for aluminum become complex and expensive when dealing with the restrictions of higher temperature processing.

2.2 Porous Metal Processing
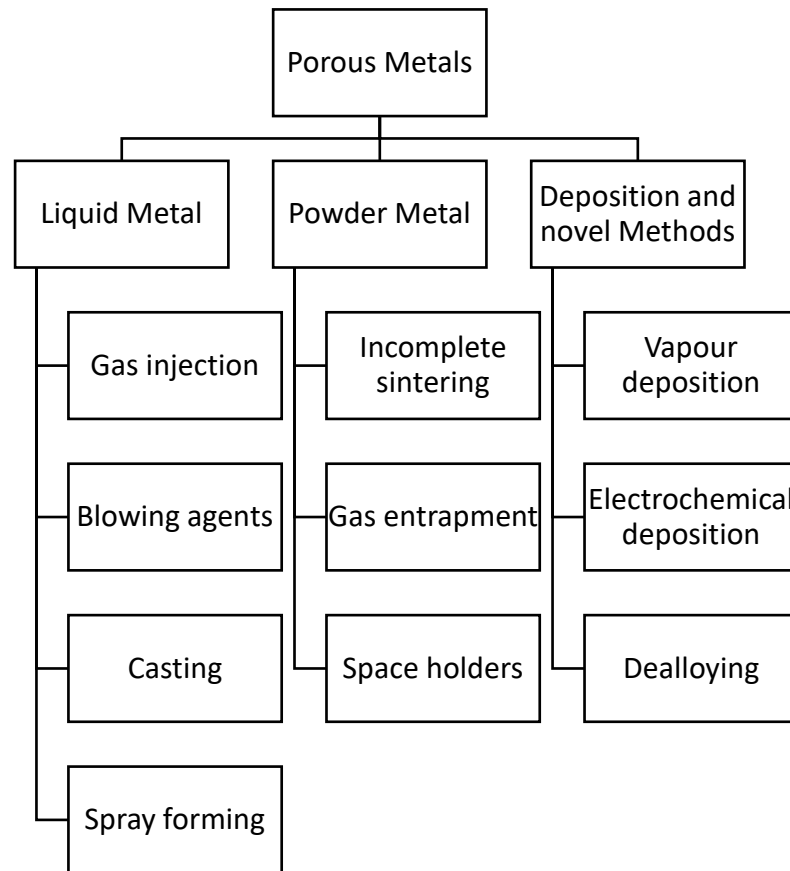
Figure 4. A diagram depicting a breakdown of the major porous metal manufacturing methods. [15, 16]

Porous metals are produced using a wide variety of methods, which many people have classified in different ways [1, 15, 17-20]; a common theme is to separate the methods by the physical state of the starting material that goes on to make up the foam. Commonly this is either as a liquid or as a solid powder; however, there are additional methods which make use of deposition techniques with the base metal starting as a vapour or in a chemical solution. This same classification will be used here to survey the different methods that have been employed.

2.2.1 Gas Injection Methods

When starting with metal in the liquid state it is possible to produce porous metals by directly foaming the molten metal. This is achieved by either bubbling an external gas through the melt or via the incorporation of a chemical blowing agent into the liquid (in the form of a powder) which then decomposes on heating releasing gas; as this gas must be retained in the structure to avoid the porosity generated being lost, utilising these methods it only possible to produce a porous metal with closed cells see Figure 5.

The process of bubbling a gas through a liquid metal to produce a porous solid is hampered when pure metals and alloys that are fully liquid at the foaming temperature are used, as once a bubble has formed it quickly rises to the surface of the melt and bursts releasing the gas. An equally valid picture to the rising of bubbles is the idea that the bubbles are stationary and the liquid is draining down between them. This process of drainage gives a clearer picture of what will happen when the bubbles collect at the surface: the liquid will continue to fall and thus some bubbles will burst. Drainage of the liquid is therefore an important process as it can control the formation of instabilities and the bursting of bubbles and gas release. In order to increase the stability of the bubbles and allow sufficient time for solidification to take place trapping the gas inside, insoluble or slow dissolving particles are added at levels up to 30 vol%. The volume fraction of the reinforcing particles typically ranges from 10 to 20% and the mean particle size from 5 to 20 μm [15, 16, 21]. Typical additions include aluminium oxide (particularly when an aluminium alloy is being used), silicon carbide or magnesium oxide. The key function of these particles is to increase the surface viscosity of the melt to allow more time for solidification to take place by slowing down the rate of drainage, and thereby the bursting of bubbles. After these particulates, have been distributed homogenously throughout the molten alloy, the gas injection can take place. The gas injector is often combined with a rotating impeller, whose function is to control the size and uniformity of the bubbles by breaking up the incoming gas stream, and to distribute them evenly. This uniformity in bubble size and distribution is required to achieve consistency in structure both throughout a single piece and between batches, which is of course essential for commercial use. This method is one of the easiest to scale and industrialise.
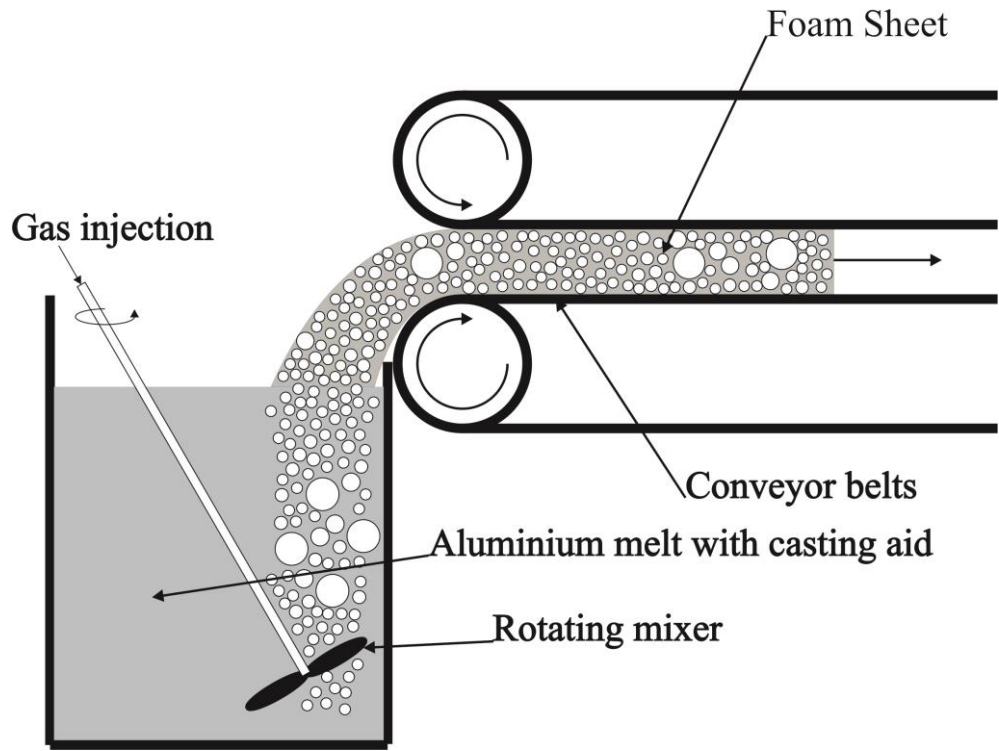
Figure 5. A schematic diagram showing porous metal produced using gas injection. [5, 15, 18]

2.2.2 Gas Release Agents

An alternative method for producing a closed celled foam where the pore volume is occupied by a gas is to use a gas releasing agent. These are compounds which thermally decompose to release bubbles within the metal. The advantage of this approach is that the gas release agents can be more homogeneously mixed into the metal before foaming, producing a more uniform distribution of pore shape and size after the foaming process (unlike direct injection, gas is generated throughout the liquid, not just at a single point). Typical gas release agents, and their products include [22],

$$TiH_2 \rightarrow Ti + H_2 \tag{1}$$

$$CaCO_3 \rightarrow CaO + CO_2 \tag{2}$$

$$ZrH_2 \rightarrow Zr + H_2 \tag{3}$$

The process of bubble formation can be controlled using a number of factors; these include the decomposition temperature of the compound used, the temperature of the foaming operation and cooling rate [23] and the addition of viscosity aids, in some cases enhanced by the by-product of the decomposition of the gas release agent ($CaCO_3$) [24-26]. The range of gas release agents that have been experimented with is large [18], not limited to the three examples shown above, mostly being based on simple metal halides [MH_2 (M=metal)] with work on more complex systems which evolve more hydrogen also conducted. The range of materials used as gas release agents even extends to natural materials, which may lower cost compared with processed chemicals when required in large amounts for large scale processing, with dolomite [$MgCa(CO_3)_2$] having been shown to be effective both as a foaming agent and stabiliser [25, 27].

The use of gas release agents can be further broken down into two types, methods where the agent is added to the molten metal and methods where a precursor is produced combining solid metal and un-decomposed foaming agent and then foamed in a separate operation.

An example of the first method is the ALPORAS aluminium foam [5]. By the nature of the manufacturing route this is a batch process, in which the desired amount of aluminium is melted, and taken to 680 °C. Then 1.5 wt% calcium is added to increase the viscosity, which occurs as the calcium reacts with trace amounts of oxygen present to form solid calcium oxide particles,

and the mixture is vigorously stirred for 6 minutes to evenly disperse the calcium through the melt. Next, the foaming agent, TiH_2 (1.6 wt%), is added with the mixture continuously stirred, again to evenly disperse the foaming agent. The expansion takes about 15 minutes, during which time the foamed metal fills the mould, and once this stage is reached the mould is cooled. The final size of an ALPORAS cast block produced in this way is $450 \times 2050 \times 650$ mm, which weighs 160 kg. For most applications this block is machined in to smaller blocks or plates.

It is also possible to produce foams from metal matrix composites where, in addition to the reinforcement, (which acts to increase the viscosity when in the liquid state), foaming agent is incorporated into the solid. An example is the FOAMCARP process [10] in which metal is induction melted before the gas releasing agent is added, but crucially using a gas release agent, $CaCO_3$, that breaks down at a temperature above the melting point, so that it can be mixed with the metal and solidified before gas is released. This method was built on the FOAMGRIP process [28] whereby the TiH_2 powder is treated in such a way that it foams an oxide layer on the surface. This surface layer acts to delay gas release for enough time so that the TiH_2 can be homogeneously mixed with the metal.

This delay allows the FOAMGRIP process [28] to produce a foamed material via the intermediate stage of a precursor before a second, independent foaming step. The metal is melted before the TiH_2 is introduced, and is then mixed and cooled to prevent hydrogen evolution. The precursor has limited porosity due to the rapid cooling with only a limited amount of hydrogen being released. When it is desired to produce the foam, the precursor is placed into a graphite mould and heated until it melts, at which point the hydrogen evolves and creates the porous structure, acting in a very similar way to other closed pore foam processing methods.

2.2.3 GASAR or Lotus-Type Porous Metal

As well as generating hydrogen from the decomposition of an added material, it is possible in some cases to produce hydrogen from the liquid metal itself, see Figure 6. In metals which form a eutectic with hydrogen (such as Al, Cr, Cu, Fe, Mg, Mn or Ni) [29-34] any gas contained in the metal itself will be released on solidification (at it undergoes the eutectic phase transformation). The metal is taken above its melting temperature in a high pressure (up to 50 atm) hydrogen atmosphere, which results in the molten metal becoming saturated with dissolved hydrogen. The melt is then directionally solidified; during cooling it undergoes a eutectic transformation forming two phases, the metal and the hydrogen gas, which forms the pores. Care is taken with the process parameters to ensure the bubbles are trapped by the solidification front and do not float out of the melt. Further complications arise as for bubbles to form in the first place a balance between system pressure, external pressure and hydrogen content is needed. The nature of the solidification results in pores being elongated along the solidification direction (very high aspect ratios are possible). Porous metals formed in this way are called gasars or lotus-type porous metals, but the use of this method commercially is limited due to safety concerns of very high pressure hydrogen and molten metal. However is has been successfully used to produce foams from steel, nickel, copper, aluminium and magnesium [16, 29, 32-34].
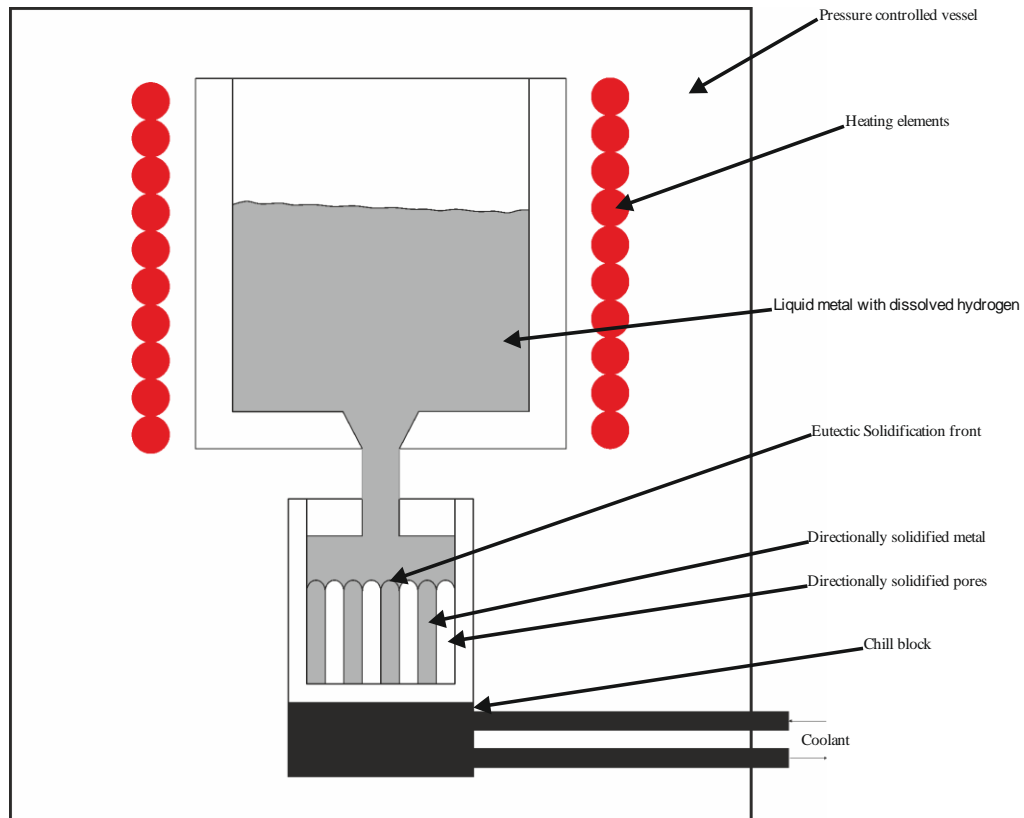
Figure 6. A schematic showing the GASER process, reproduced from [15]

2.2.4 Powder Methods

Porous metal can be produced without the need for processing in the liquid state. Commercially this process is acceptable for metals that are difficult or expensive to melt and use in a liquid state. Any metal which meets these criteria and can be formed into a powder can use this route. The best type of powder and most widely available for these methods is vacuum melted, gas atomised. This powder production route processes spherical powder, with minimal segregation, has higher packing efficiency, good flow properties all while minimising the surface oxide formation. These characteristics all aid in the processing of the powder into a foam particularly sintering.

The whole process can be broken down into three steps, shown in Figure 7, though there are some variations on the technique that give rise to different structures.
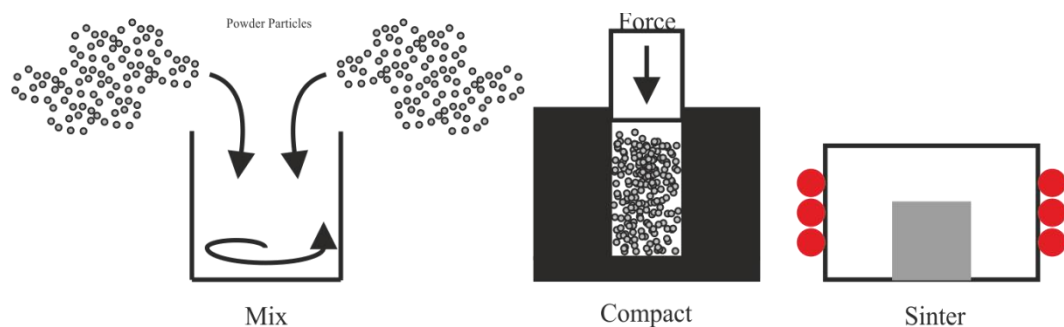
Figure 7. A schematic showing a method for producing a porous metal from metallic powder. [15, 16]

Powder metallurgy methods can be employed to produce porous metals, known as 'sinter metals'. The simplest of these methods is to use incomplete sintering by finishing the process before full theoretical density is reached; in this case the voids present between the powder particles form either the closed cells or the open porous network (with the type of porosity present dependent on the extent of sintering before the process is interrupted).

To perform this process green compact is heated to a point where mass transport can occur in the solid particles. The driving force behind sintering is the excess free energy present in fine

powders due to their high surface area to volume ratio. The two main mechanisms for mass transport during sintering of metals are grain boundary diffusion and surface diffusion [35-39]; both will be present in fine powders. Which one of the two dominates is dependent on the particle size and temperature (if any external pressure is applied then plastic deformation or creep may also contribute). In surface diffusion atoms move from the particle surface to the contact area between the particles increasing the neck size until it is the same as the particles. In this case the centre to centre distance of the particles remains the same, and in essence the gap between them is filled. In grain boundary diffusion atoms from move to the surface of the particles at the neck. This motion will pull the two particles together reducing the centre to centre distance as a result. If the centre to centre distance is reduced this will in turn reduce the open cavities within the foam's porous structure, which will make the foam denser and also restrict flow of fluids through the foam [38, 39].
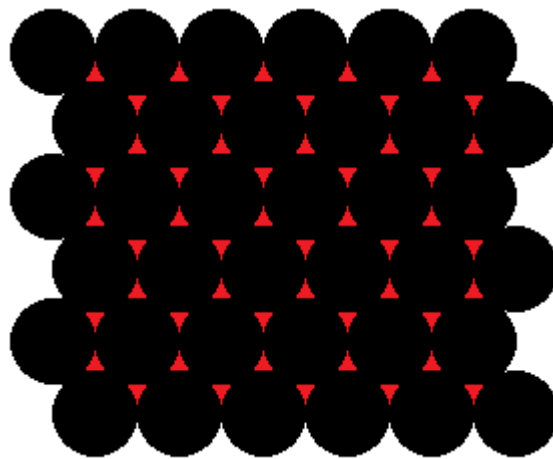
Figure 8. A diagram showing the maximum packing possible when same sized spheres (black) are used and the unfilled reaming space (red)

As can clearly be seen from Figure 8, showing a close packed layer in 2D, if spheres of the same size are used and packed as closely as possible in a confined volume, the amount of porosity is low (indicated by the red sections; note that porosity will be open in a 3D version of this structure). This method of producing a porous metal requires incomplete consolidation of the powder, and as such the resulting final structure suffers from the same restrictions and compromise in properties associated with partial sintering [40-42]. Increasing the sphere diameter will increase the individual pore size however the pore volume fraction will be the same.

Packing density of close packed spheres is a maximum of 74% of the space filled (this assumes touching hard spheres with zero necking or mass transfer between the spheres), which indicates the approximate porosity that would be expected at the start of sintering (and would decrease during the sintering process).   However, this is not always a good approximation in real situations, see the schematic diagram in Figure 9.Random packing will not reach 74% space filled. The use of different particle sizes and geometries can alter the packing density, making it either larger or smaller [43-45]. Nevertheless, the degree of control using this method is limited.
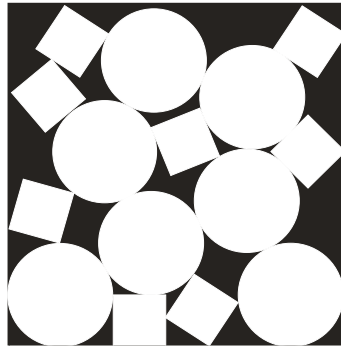
Figure 9. A diagram showing how changing the particle geometry can affect the packing density

In any sintering technique in the absence of a gas release agent of some kind the porosity of the foam can only be less than or equal to the porosity of the green body. In order to increase the level of porosity and specifically to create open cells, the use of second (removable) phase particles is needed. These particles act as space holders, holding the metal powder particles apart during green body formation and the early stages of sintering. Space holder materials fall into two categories, those materials that are removed before or during sintering and those materials that are removed after sintering. The space holder material is selected based on the properties of the metal being used, with key considerations being relative melting temperature and reactivity between the space holder and metal. Secondary considerations are based on the removal method of the space holder and whether that will occur before or after sintering.

If second phase particle removal is to occur before sintering the following considerations need to be taken into account; firstly the volume fraction of metal left must have sufficient green strength to support itself after the space holder has been removed. The removal method itself, whether the space holder is dissolved chemically (e.g. NaCl [46-48]) or removed thermally (e.g. Polyurethane [49, 50]), and what effect the removal process will have on the metal, for example if the dissolution product is corrosive to the base metal.

A space holder material which is removed after sintering must withstand the sintering conditions required (temperature, pressure and atmosphere), but also go through a removal process. after solidification. This removal step must be chemical as in this case the space holder is by definition, thermally stable. the space holder is removed in conjunction with the metal sintering, eliminating the need for a separate processing step.

The green strength of the space holder metal mixture is improved with the addition of polymer binders to the system, which are blended with the powders until a homogenous mix is obtained, after which point they can be processed. Compaction of the blend is the most common method, which can be through uniaxial pressing, hot or cold isostatic pressing and even metal injection moulding (MIM) to form a green body [51, 52]. Various materials have been successfully used as space holder materials from expanded polystyrene [53], and even other metals such as magnesium have been used [54]. Esen [7] used large (425-600 µm) magnesium powders mixed with smaller Ti powders (45-150 µm) and polyvinyl alcohol (PVA) and water solutions as a binder. The mixture was cold pressed into a green body and heated to 1200 °C in argon to debind the PVA, sinter the Ti powder and evaporate the magnesium, resulting in a porous structure. Typically, however, organic compounds are used as the space holder with ammonium hydrogen carbonate $(NH_4)HCO_3$, carbamide and PMMA particles all having been used successfully [51, 52, 55-57], more recently even tapioca starch has been used with titanium powders [58] to produce porous titanium. The reason behind this search for simple and low cost space holders is to reduce the cost of processing and the resulting material.

The table from [58] shows types of space holder and removal method.

Table 2. Typical space holder in titanium and alloy foaming. [58]

Metal Powder	Space Holder	Removal Method
Titanium	Magnesium	Thermal
Titanium	Carbamide	Thermal
Ti-6Al-4V	Carbamide	Thermal
Ti-6Al-4V	Magnesium	Thermal
TiNi	NaF	Solvent
TiNi	NaCl	Solvent

2.2.5   Additive Layer Manufacturing (ALM) and Structured Cellular Metals

Additive layer manufacturing is a relatively new technology for producing metal parts. It builds on the success of rapid prototyping technology used to produce 3D parts from polymers. A computer aided design (CAD) model is produced of the part, this is then fed into a software package designed to slice the model up into layers, such as Magics by Materilise [59]. These software packages produce and allow editing of STereoLithography (STL) files, which are in turn uploaded to the ALM machine to produce the part.

Various methods exist to transform this STL information back into a physical object replicating the part modelled. One method is to extrude a slurry containing a metal (powder or fibers) and carrying agent. A height adjustable platform with an x-y stage is used to control the location of the deposits, this method is similar to piping icing. The layers are built up on top of each other. Due to the deposition method each layer is responsible for supporting all those above; once the structure has been fully deposited, a vacuum furnace is used to drive off the remaining moisture and sinter the powder. This method has been used to produce parts suitable for biomedical applications using Ti6Al4V [60].

The most commercially advanced method for producing metallic parts is to use a powder bed technique. The principle used for producing a metallic part involves laying down a thin layer or bed of metal powder, then using a directed energy beam to melt a small area of the powder before moving on to the next drawing out a pattern of molten material which then solidified. The part is moved down and another thin layer of metal powder is spread on top and the process is repeated for thousands of layers until a component has been build up, the depth of the layers and the size of the powder is the ultimate factor in the resolution or minimum sized feature that can be produced. The operation takes place in an inert atmosphere to minimize oxidation, the powder bed also requires a degree of preheating and post process cooling to manage stresses which build up in the components during the building process. These systems again utilise CAD models and software packages to slice the parts before being transfered to the machines. This method of production is ideal for the production of very complex parts. Structured cellular parts are relatively easy to design using CAD software. With some limitation in geometry the powder bed provides support for overhanging and freestanding features within parts; once processed the partly sintered support material needs to be removed and internal cavities require openings to allow for the powder inside to be removed. The powder that is removed may be sieved and reused to increase material use efficiency. Two main sources of energy are used to melt the powder, a focused electron beam, as used by Arcam AB (www.arcam.com), or a focused laser

beam employed by both EOS (www.eos.info/en) and Renishaw (www.renishaw.com). Electron beam melting (EBM) is the more commonly used technique for producing structured cellular parts and metallic lattices [61-64], with titanium and its alloys seeing the most research and investment as to bring down the high associated cost of fabricating parts from titanium alloys. Lattice structures can be produced with strut arrangements ranging from simple squares and cubic geometries to more complex tetragonal arrangements. It is even possible to have graded densities and changes in strut geometries produced in the same component [65] to give different physical properties at different locations in a single component.

2.2.6　Porous Metal Produced by Deposition on to a Substrate

Polymeric foams again prove to be very useful in the processing of porous metal products, in this instance an open celled polymer foam is coated in metal (foam polymer must be open celled to allow access to internal structure). The methods for coating the polymer include common deposition methods used on dense substrates such as chemical or physical vapor deposition, the metal also can be deposited electrolytically. A metal powder slurry can also be used to apply a metal layer, but this requires sintering after deposition to form the metallic layer. The polymer will then be removed from within the deposited layer (leached or burnt out) to leave behind a porous metallic structure. In addition to the porous structure replica of the polymer the struts of the structure will also be hollow due to the removal of the polymer from the internal spaces. The porous structure produced using deposition methods onto a polymer will have similar pore geometries to the original template, however they will be smaller and less defined due to the deposition of material onto the struts encroaching into the pore volume. In most cases struts will also be hollow, the space arising from the removal of the template [20, 66].

Open celled nickel foams can be produced using chemical vapor deposition (CVD) the reference [67] describes the process employed commercially by Novamet (www.novametcorp.com) under the trade name Incofoam. Onto a polyurethane (PU) open celled substrate foam nickel carbonyl gas decomposes under catalysis action of hydrogen sulfide into nickel which is deposited onto the PU foam. The system is heated to 180°C to increase the rate of the reaction. Once deposition is complete sintering in a reducing atmosphere removes the PU foam and increases the physical properties of the deposited layer. CVD is used to deposit tantalum onto a vitreous carbon structure [68] to produce orthopedic implants. The carbon scaffold can be replaced with one that is fabricated from Ti64 using EBM to produce a lattice structure. Tantalum pentachloride is reduced by hydrogen atmosphere and tantalum is deposited onto the scaffold which is not then removed [64].

As outlined above for the gas phase deposition production route, the production of a porous metal using an electrolytic technique also starts with a substrate to give the initial structure of the foam which is often a polymer, although in some cases another metal is used, commonly in this latter case to carry a functional layer [69-71]. In the case of the polymer substrate it must first be made conductive. This can be done using CVD to deposit carbon or another metal as previously discussed, once conductive the polymer foam can be coated using traditional electroplating techniques and a range of metals including both copper and nickel [72, 73] . Metals can even be deposited electrolessly, demonstrated for both copper and nickel alloys [74, 75].

Porous metals manufactured using these methods are among the most commercial available in part due to the use of porous nickel in electrode applications in particular NiMH batteries. [69, 76, 77].

The production of a porous metal by deposition onto a polymer substrate either from the gas phase (CVD) or from a liquid phase (electrochemical) is limited by the depth of the effect penetrating into the foam structure (for example, some deposition methods are line-of-sight only) and hence there is a maximum size limitation of the foam that can be produced. These methods rely on transport of the deposition metal and driving force (current or reactant) through the substrate, the thickness of the layer varies edge to center with and upper thickness around 1-2 cm depending on factors including the pore size, substrate material and deposition method [72-74].

2.3   Replication Processing of Porous Metals

Many foam production methods use established processing techniques for dense metals, with a greater or lesser amount of modifications. This theme continues to a modified version of investment casting, which when applied to foams may also be called replication.

With investment casting a model of the final piece is made, often from wax in order to capture fine scale detail, and then coated in a fine ceramic powder (to retain this detail) and further coated with a ceramic slurry. The assembly will then be baked to set the slurry and also melt the wax model to form a cavity, before molten metal is cast into the cavity. The metal solidifies and the mould is removed, leaving behind a replica of the cavity which is the final cast. The same essential process can be used for foams, with the removable former having a foam shape.

The extensive variety of polymeric foams available in terms of materials and morphology, makes them ideal to act as the mould in an investment casting situation. However, to make a polymeric foam suitable for this application it will need to be an open celled foam, which is achieved by the reticulation of a closed celled foam, holding it at elevated temperatures and changing pressures in such a way that the cell walls burst leaving the cell edges to form the open network required [11, 78].

The process involves taking the now open celled polymer foam, (polyurethane is frequently used, for example in the production of magnesium foams [50]) and pouring a ceramic slurry around the foam so that the foam is completely infiltrated; this step effectively limits the method to low density foams where the pores are well interconnected. The ceramic is then baked [79], in conjunction with this step or in a separate heat treatment the polymer precursor is burnt out leaving behind a ceramic mould of the polymer foam. This mould is used to cast the molten metal into. Once it has solidified the ceramic is removed typically using jets of high pressure water or air [49] (this step is dependent on the particular ceramic used) to leave behind a metal foam. As with all castings shrinkage must be considered and depending on the metal used the shrinkage could be large. Duocel foam produced by the ERG Aerospace Corporation [80], although not stated by the manufacturer, appears to be a product produced this way, with similar morphology and structure to foam known to be made using this method [49, 50, 81, 82]. Metals processed in this way and sold commercially by ERG include tin, zinc, nickel and Inconel. One aspect of using a polymer precursor has been exploited to produce a single casting with a gradient in density [81]; the ability of a polymer to be compressed to varying degrees along a

distance by squeezing a cone shape piece into a cylinder lead to a varying density along the length. This varying density is translated to the metal foam cast from this precursor.

The replication process used to produce porous metals is similar to investment casting in that metal replicates the cavity within a mould, however material of the mould, its form and how it is used differ between the two. In replication casting the shape is created by assembling elements to form a mould that represents the pores in the final item, in contrast to investment casting where the precursor defines that shape and morphology that the metal will take after casting.

In order for this mould to be effective it must be removed once solidification has occurred. As such, most of the materials which are suitable to act as space holders are also acceptable for use as mould materials in replication; a critical difference is the melting temperature of the mould material, which must be sufficiently higher than the casting temperature of the metal so that it does not undergo thermal breakdown, volatilisation, melting or mechanical deformation. These conditions reduce the choices of suitable mould materials and requires a more tailored approach to selecting which materials are used for which metals. These strict requirements result in few materials being suitable for this method of production, and they are restricted to metals with relatively low melting temperature such as Aluminium in order for simple salts ($NaCl$, BrF_2 [83]) to be used as the space holder.

2.4   Methods to Produce Metals with Nanoscale Porosity

The methods previously discussed are suited to making porous metals of macro and micro scale, however methods are also available for the production of porous metals of a finer scale with chemical manipulation of the physical structure of materials to result in pores.

2.4.1   Nanoscale Porosity Produced through Spinodal Decomposition and Dealloying

The production of a nano scale porous metal requires manipulation of the microstructure of the metal in order to facilitate the formation of chemically distinct phases. Spinodal decomposition is one such mechanism and is described in more detail in section 2.7.2 Once distinct phases have been formed dealloying may be used to remove one of the phases.

Dealloying is a corrosive process in which the system is placed in a corrosive medium and the least noble constituents are leached out of the system leaving the most noble behind [84]. This can be unassisted, by which we mean that the material is left in the corrosive medium for a set time, or it can be performed with the aid of a potential difference to increase the rate of dissolution. An example of the type of structures which can be produced using this method is shown in Figure 10.
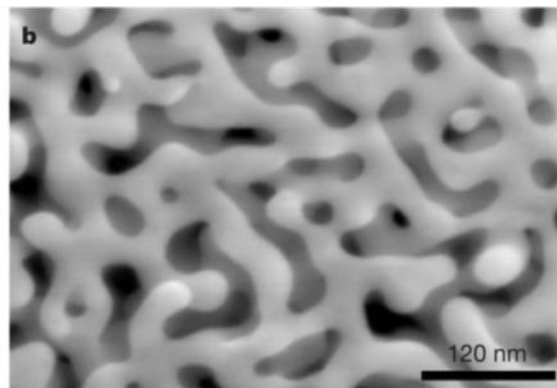
Figure 10. SEM image of nanoporous gold produced by selective dealloying of a Ag-Au alloy in nitric acid under free corrosion [85].

This structure was produced by taking a gold-silver alloy with a composition of 68 at% Ag and 32 at% Au, and placing it into nitric acid under free corrosion. Free corrosion is limited by the depth that it can be effective. It will only affect the surface region, causing pitting rather than through thickness corrosion. If this is required an electrochemical potential can be applied to dealloy the whole thickness of the sample, although this has only been reported experimentally for microscale samples.
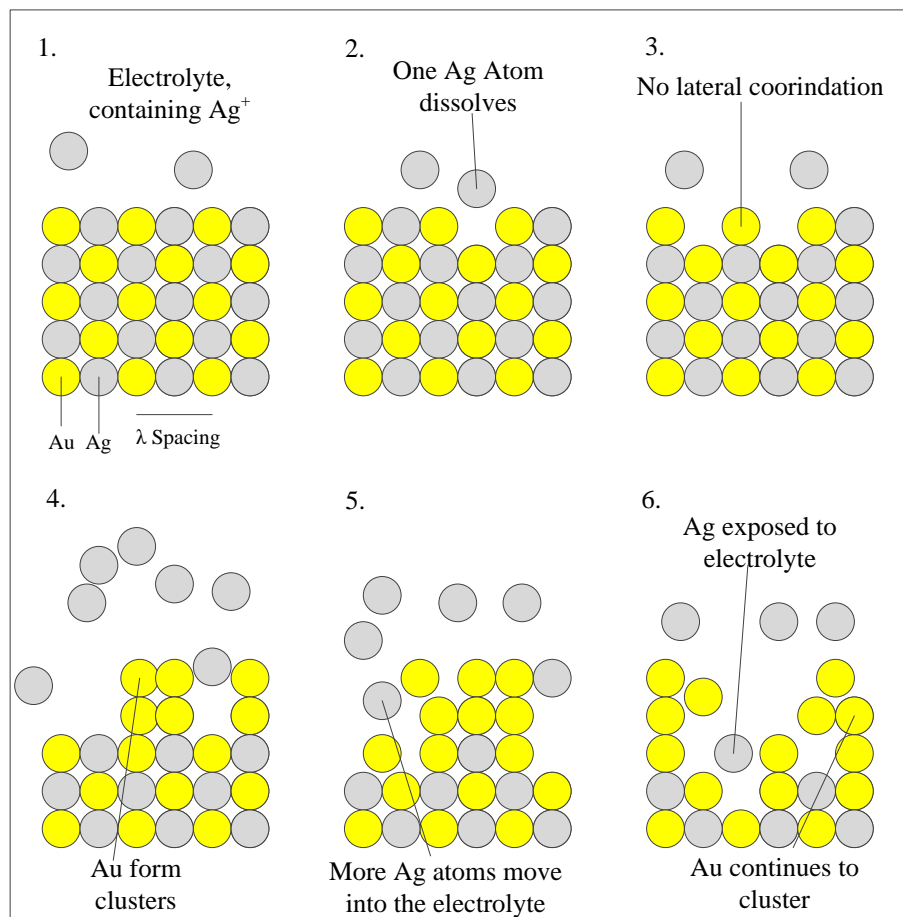
Figure 11. Schematic diagram of the dealloying mechanism in Ag-Au [85].

The dealloying mechanism in Ag-Au proceeds in the following way; the sample is placed in a corrosive electrolyte (Figure 11, 1), in this case nitric acid with an addition of silver ions; a potential is applied and the dissolution begins with a single silver atom moving into solution (Figure 11, 2) leaving the laterally coordinated Ag atoms more susceptible to further dissolution (Figure 11, 3); once dissolution has resulted in a whole terrace of silver atoms being removed this leaves behind gold atoms which have no lateral coordination. These gold atoms now diffuse and agglomerate to form islands (Figure 11, 4). This diffusion results in clusters of pure gold and areas of the original alloy (Figure 11, 5). These areas are now exposed to the corrosive medium which results in further dissolution of the silver atoms, which in turn leads to further diffusion of gold atoms into larger clusters (Figure 11, 6). This process continues until all the silver atoms have moved into solution leaving behind only gold. The spinodal decomposition in the system is concerned with the diffusion of the gold atoms once the silver has been leached from the solid. Spinodal decomposition occurs in two phase systems. In this case the phases are the gold atoms and the silver atoms. Once the silver atoms have been stripped off the surface, this leaves a locally high concentration of gold atoms but with the same site occupancy as the bulk (as no movement has taken place yet). This concentration is however much higher than the equilibrium

concentration (equilibrium of the two phase system), this means there is a driving force (which is very large) for the gold atoms to diffuse, making the system unstable and subject to spontaneous phase separation which results in the formation gold rich clusters. This atomic diffusion is against the concentration gradient in the bulk. The length scale (λ) of this diffusion is important as this determines the final microstructure of the gold nanopores; long length scale growth is slow as diffusion times are much longer. Short length scale growth is inhibited as the small fluctuations in the alloy concentration create a smaller driving force. It is only at intermediate length scales that the diffusion and phase separation occurs at a rapid rate, this length scale equates roughly to the spacing between the gold rich clusters [85].

A variety of alloys and conditions have been used for dealloying and show spinodal decomposition resulting in a nanoporous microstructure. Both galvanostatic and potentiostatic techniques have been used [86], with galvanostatic producing superior results in bulk samples. Alloys which have been successfully processed include Ag-Au and Mn-Cu and are shown below in Table 3, with the type of electrolyte used, if reported.

Table 3. Alloy systems and the corrosive medium used to produce nanoscale porosity using this method.

Metal Alloy	Electrolyte Used
Ag-Au	Nitric acid (galvaniostatic) [85]
Mn-Cu	HCl (free corrosion) Citric Acid (free corrosion) Ammonium Sulphate + Manganese Sulphate (free corrosion) Sulphuric Acid + Manganese Sulphate (free corrosion and potentiostatic) [87]

It is also possible for spinodal decomposition to occur in alloys at elevated temperatures in the absence of an electrolyte. This process allows for more conventional (nucleation and growth) microstructure evolution [88].

The required conditions for spinodal decomposition to result in a single phase nanoporous metal can be summarised as follows:

- The metal alloy must display single phase solid solubility (can be natural or forced using rapid solidification techniques).
- The alloy must contain one component which is less reactive (more noble) than the others, to allow for dealloying to take place.
- A corrosive medium which can preferentially remove one component and hold it in solution must be used.

An electrochemical cell to increase the rate of corrosion and aid in through thickness corrosion is necessary to produce relatively large samples.

The use of dealloying and spinodal decomposition for the production of nano-scale porosity will always be limited to a small selection of alloys that can be used when compared to the less stringent requirements for production methods of macro porosity.

2.4.2 Raney Nickel as a Production Route for Porous Metals

The production of Raney nickel uses the binary alloy precursor NiAl, with the aluminium being removed from the alloy by reacting it with sodium hydroxide solution [89].

$$2\ NiAl\ +2\ NaOH\ \xrightarrow{6H_2O}2\ Ni_{Renay}+\ 2\ Na[Al(OH)_4]+3\ H_2 \qquad (4)$$
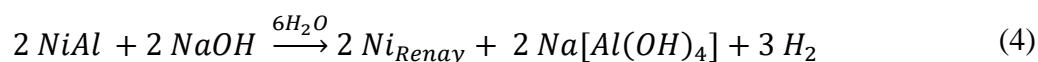
The ratio of aluminium to nickel may be used to control the porosity. During this process the mixture must be kept cool and away from sources of ignition due to the quantities of hydrogen evolved. The result is a nano porous nickel metal which is widely used as a catalyst in hydrogenation reactions [90, 91] and more recently in hydrogen fuel cells [92, 93]. Importantly the porosity can be controlled in Raney nickel by controlling the temperature, time and concentration of the sodium hydroxide used in the leaching operation [94].

2.4.3 Hollow Structured Nano Materials

While not foam in the traditional sense, it is possible to create a solid body containing a level of porosity in the form of a hollow structured nano material. In such structures the porous part takes up majority of the volume of the material. Principally constructed from noble metals such as gold and silver, these structures are termed nanocages and are currently being researched for their suitably in drug delivery and sensors [95-99]. The starting material used in the production of gold nanocages is $HAuCl_4$ nanocubes which undergo a galvanic replacement reaction, this reaction results in a nanocube which has a hollow center. This hollow center can be filled and the outer is coated in a polymer film, a laser with wavelength matching the absorption peak of the gold nanocages is used to heat the
cage which causes the polymer to break down and release through the pores whatever was trapped inside [96, 98].

2.5   Porous Metal Properties

The properties of a porous metal can be broken into two broad classifications, those that are the result of the metal having a porous structure and those that are a result of the base metal that has been used. The properties that come from the pore structure are of a functional nature due to the surface area to volume ratio, which make these materials excellent as substrates for functional coatings or functional with a coating relying on the properties of the metal itself such as thermal and electrical conductivity. This is tied into the second key point regarding the properties of porous metal and that is the importance and effect the metal has on the subsequent properties. The most obvious is melting temperature this is unaffected by the level of pores as adding pores to the structure will not change this fundamental physical property. The mechanical properties of the porous metal can be altered by adding pores to the structure these can be approximately based on scaling laws based on the density change described in [1].
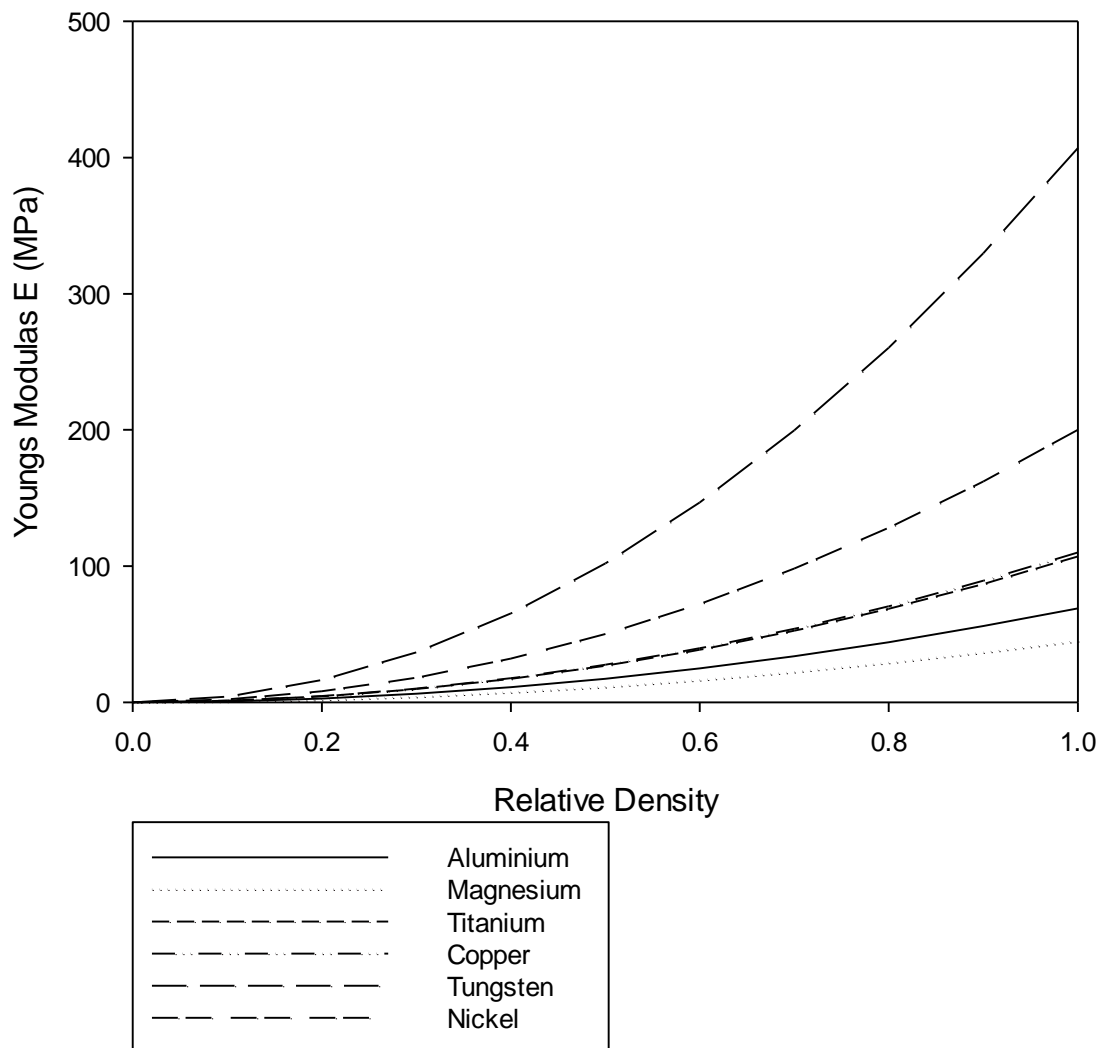
Figure 12. A graph to illustrate the predicted effect of relative density on the Young's modulus of several metals, generated from the Gibson-Ashby model.

In order to show the effect of reducing the relative density on the mechanical properties a series of scaling laws derived by Gibson and Ashby [15] can be applied. These have been developed mainly for polymeric foams and empirically fit to experimental data for metallic foams. The following equation can be used to approximate the change in Young's modulus with relative density. In this example the equation is fitted for an open-celled porous metal.

$$E = (a)E_s \left(\frac{\rho}{\rho_s}\right)^n \tag{5}$$

here E is the Young's modulus of the foam, E_s is the Young's modulus of the bulk solid metal, ρ is the density (subscript s denotes bulk solid), n is a fixed power of 2 and a is an empirically fitted constant (0.1-4). In Figure 12 an arbitrary value of 1 was used for all materials.
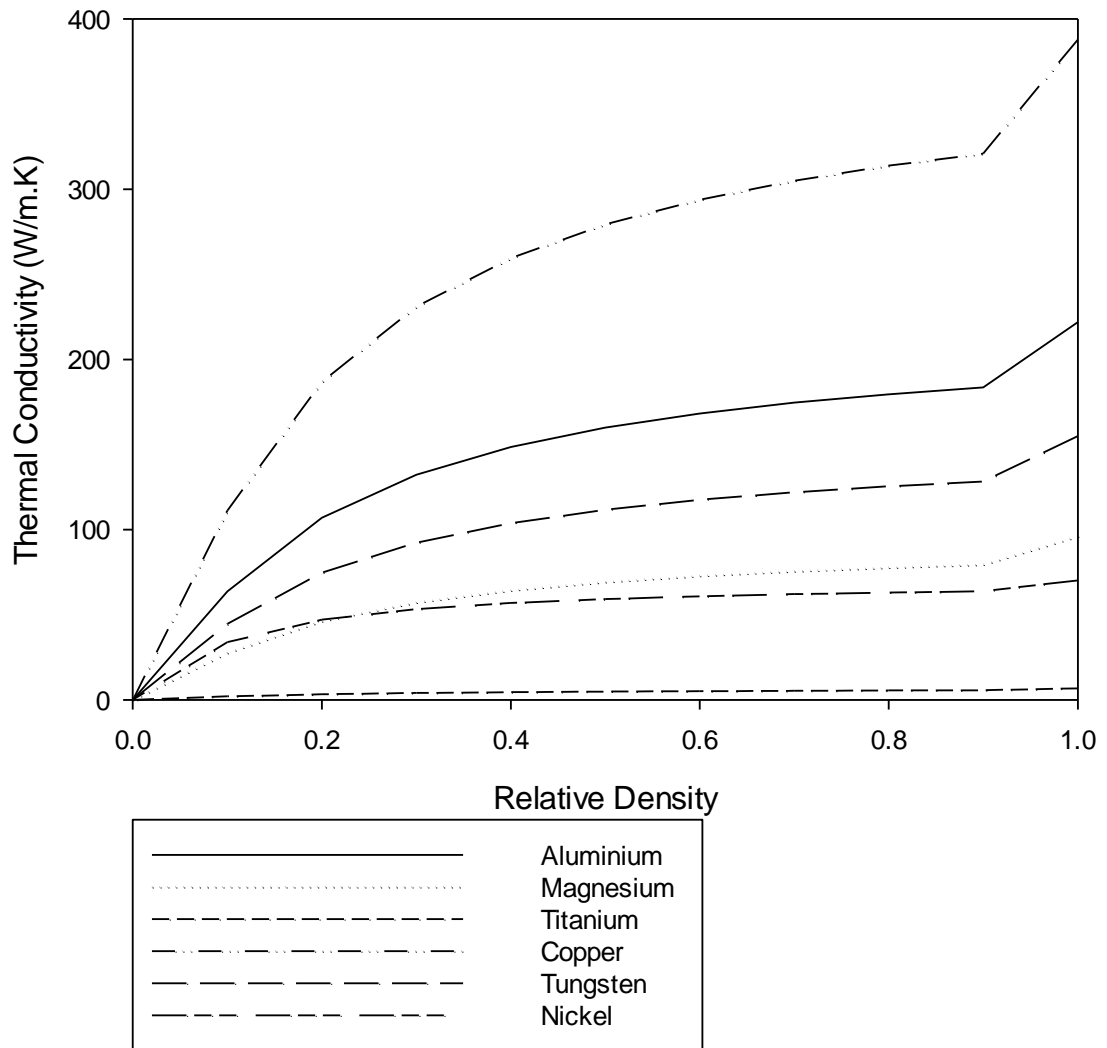
Figure 13. A graph to illustrate the predicted effect of relative density on the thermal conductivity of several metals, generated from the Gibson-Ashby model.

In a similar manner to the mechanical properties, scaling equations have been devised for the thermal properties of materials and how these change in response to changes in the density. In Figure 13 the upper was limit plotted.

$$\left(\frac{\rho}{\rho_s}\right)^{1.8} < \frac{\lambda}{\lambda_s} < \left(\frac{\rho}{\rho_s}\right)^{1.65} \tag{6}$$

where ρ is the density of the bulk solid with subscript s denoting the density of the porous solid, and λ is the thermal conductivity with subscript s denoting the thermal conductivity of the porous solid. The dramatic change from 1 to 0.9 is attributed to formation of pores in the structure and the interruption to pathways for conductivity within the material.

The most widely used mechanical test for assessing the physical properties of a porous metal is compression testing [1, 41, 100, 101]. A schematic of the stress-strain response during a compression test is shown in Figure 14.

ELASTIC-PLASTIC FOAM
COMPRESSION

DENSIFICATION

σ_{pl}^{*}

PLATEAU (PLASTIC YIELDING)

LINEAR ELASTICITY (BENDING)

STRESS, σ

STRAIN, ϵ

0

ϵ_D 1
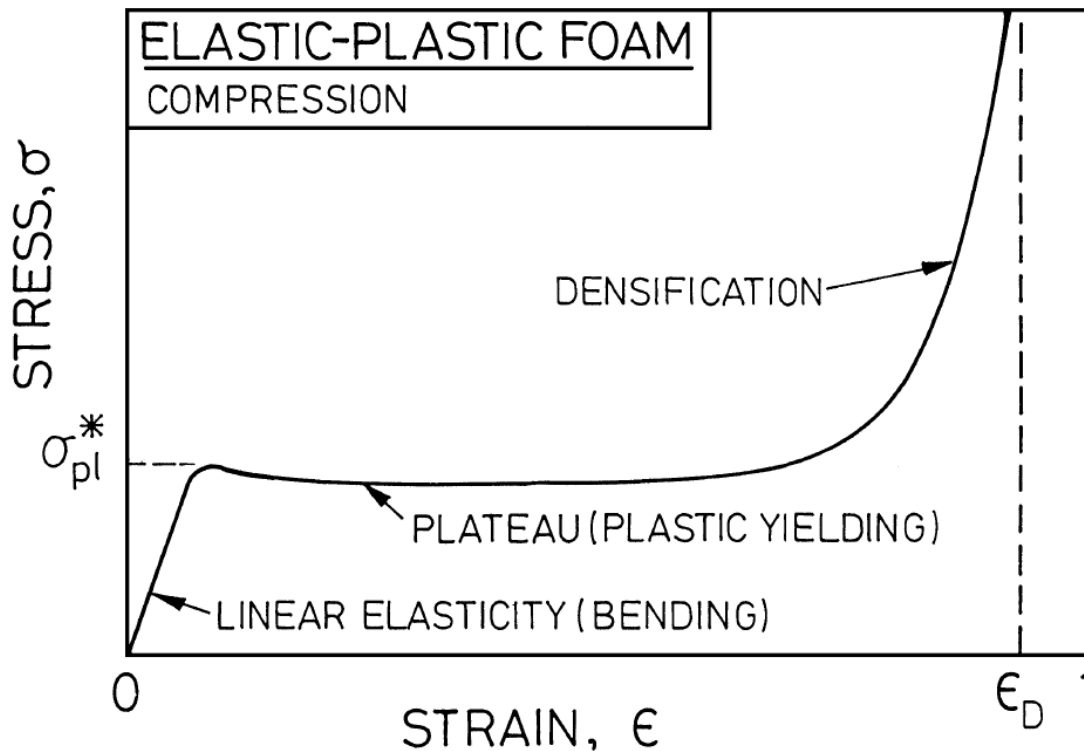
Figure 14. A schematic stress-strain curve for a foam showing the linear elastic, stress plateau and densification regimes [1]

When a porous metal is subjected to a compressive force three distinct mechanisms take place, first the linear elastic bending of the struts occurs. Once force exceeds the elastic limit of the metal plastic yielding occurs and results in a plateau, in the porous metal itself this equates to the collapse of the structure as struts fail progressively. Once all the struts have collapsed a final densification stage occurs. The magnitude of each of these sections is dependent on the properties of the base metal, but it is also highly dependence on the porous structure itself in [102] the same based metal (Ti64) foam was produced with different pore sizes with increasing pore size resulting in a decrease in the Young's modulus and yield strength. Additive manufacturing can be used to produce porous metal with different compression responses in different directions and even research is currently ongoing in tailoring this behavior [103]. As a result of the random nature of some types of porous metal getting repeatability data can be difficult and requires large data sets for confidence in the finding to be established. The majority of the mechanical testing that is currently performed is compression testing as these samples are

the easiest to produce as they do not require the same levels of preparation as tensile or impact samples would. It is difficult to machine and fix porous samples into a testing rig without causing damage which would reduce the performance of the material. Other functional testing such as for energy absorption and shielding, thermal and electrical conductivity [8, 22, 71, 103-105] is conducted when required.

2.6   Porous Metal Applications

Porous metals have a great scope for applications in several areas to which they can bring great benefit. An overview of some of the types of application that have been suggested and the extent of porosity they require can be found in Figure 15, taken from [16].

Currently the most common form of foams used in structural applications is as aluminium sandwich structures. Sandwich panels are used where weight saving is a primary concern, as they can provide the required strength and stiffness but with lower mass, and also in safety applications where the deformation of the foam absorbs impact and energy [1, 6, 8, 14, 23, 105, 106].
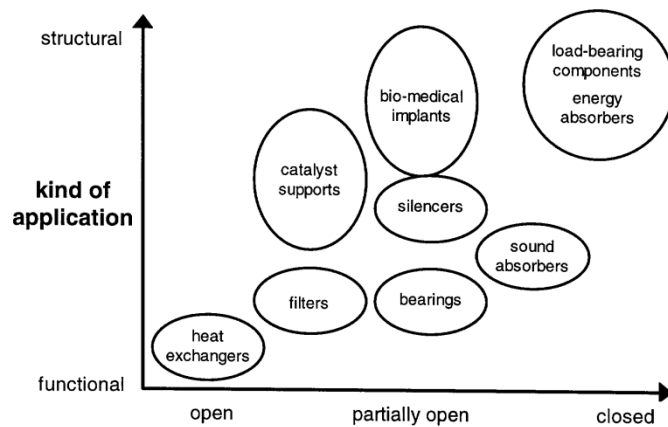
Figure 15. Applications of cellular metals grouped according to the degree of "openness" needed and whether the application is considered to be more functional or structural [15].

These applications include auto body parts, lift panels, ship bulkheads, ballistic armor and flame retardant panels. In applications where greater load bearing capacity or stiffness is required titanium sandwich panels could be used due the better mechanical properties offered by titanium (although available processing routes lack the flexibility of structures that can be achieved with aluminium). Replacing aluminium panels with titanium panels would reduce the thickness considerably but retain the same level of strength. Titanium foam or titanium foam sandwich structures would be an economical (and practical from a toxicity point of view) alternative to beryllium [107].

Porous titanium materials produced from powder have found uses inside the human body as structural bone implants, due to the biocompatibility of titanium and the porous nature of foams meaning bone cells can grow into the foam to hold it in place. One of the unique features of

foams is that the porosity can be tailored, and as such the properties can be tailored to match that of individual bones [108]. High porosity results in reduced strength, so less porosity can be incorporated when higher strength is required. The pore size can also be tailored to promote the distribution and growth of new bone and tissues and also encourage fluid transport [51, 56].

Titanium being corrosion resistant would be expected to give foams which are also corrosion resistant, meaning they can be used as filters and heat exchangers in fluids which could react with other metals. This would be beneficial in the chlorinated environments of desalination plants [109]. The trade off in terms of the lower thermal conductivity of titanium is compensated for by the length of time devices would be able to operate for in the fluid. One increasingly important potential use is as an electrode in fuel cells, the high surface area to volume ratio make foams ideal for this use. The strength of titanium means thinner electrodes can retain an acceptable level of strength. With its low reactivity titanium is able to operate at higher temperatures in more aggressive electrolytes resulting in higher power densities being possible; surface coatings can be applied to further enhance the foams properties [110, 111].   The uses and applications for titanium foams will undoubtedly increase once the production can be more tightly controlled to give dependable results and designers can rely on the properties available to them. Even with the continued move to composite materials, metallic foams will for the foreseeable future be an attractive option for products which need high strength at low weight in high temperature environments and those which require thermal or electrical conduction to be a key property. The uses of titanium are closely related to cost. Titanium tends to be used where increasing the performance is the primary concern not minimising cost. To match the surface area to volume ratio which a foam can achieve would require extensive and expensive machining using a solid titanium block, or forming of sheet, hence it is not used. Cheap foam manufacture could open up a whole new sector for the use of titanium, where previously it would be too costly. Foam production is closely related to near net shape manufacturing, which also aims to reduce the amount of post process machining and shaping so there is a precedent for a move away from heavily machined items.

2.7 Solidification, Binary Alloys and Spinodal Forming Alloys the Formation of Multiphase Structures through Solidification

Solidification is a process where though cooling a liquid undergoes a change of phase to form a solid, and is a key step of much practical metals processing. The solidification of pure metals rarely occurs (impurities will always be present at concentrations which can change the solidification behavior). As such, discussing the solidification of alloys is more appropriate and specifically single phase binary alloys.

Using Figure 16 as an idealised system (with straight lines for the liquidus and solidus) an alloy with composition X_0 can be imagined. The partition coefficient k is the ratio of the mole fractions of solute in the solid and the liquid in equilibrium at a given temperature [112].

$$k = \frac{X_S}{X_L} \tag{7}$$
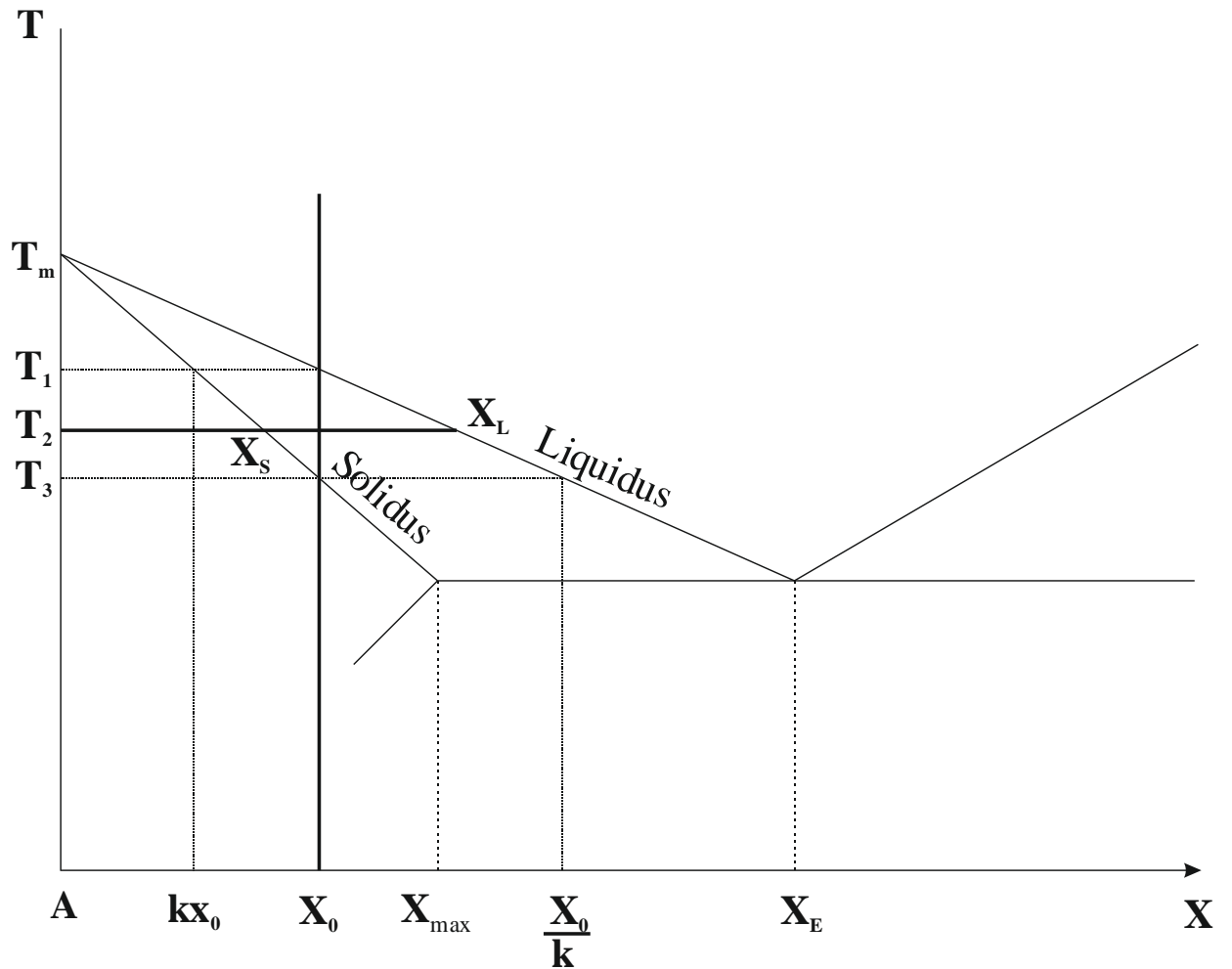
Figure 16. Idealised eutectic phase diagram

In practice the solidification of alloys is a complex event involving temperature gradients, cooling and growth rates, but the system can be simplified by assuming a planar interface, Figure 17, between the liquid and solid phases. The system is modelled as a long bar undergoing directional solidification strictly along its long axis.
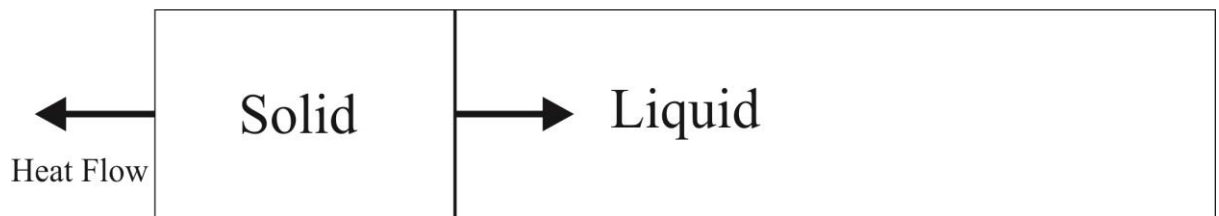
Figure 17. Schematic of a planar directional solidification front

The mechanism for solidification can be broken down into three limiting cases, however in practical terms during solidification all three will contribute in varying degrees depending on the conditions used.

The simplest case is that of infinitely slow solidification. As an alloy with overall composition X_0 is cooled through T_1 the first solid forms. Using the lever rule this can be shown to have composition kX_0. As the alloy is further cooled at an infinitely slow rate, this allows for solid state diffusion to occur; as a result the solid and liquid are always as predicted by the lever rule. As the alloy is cooled to T_3, all the liquid is now solid, with the last liquid to solidify having a composition of X_0/k.

The case shown schematically in Figure 18 depicts what is occurring at an intermediate temperature, T_2
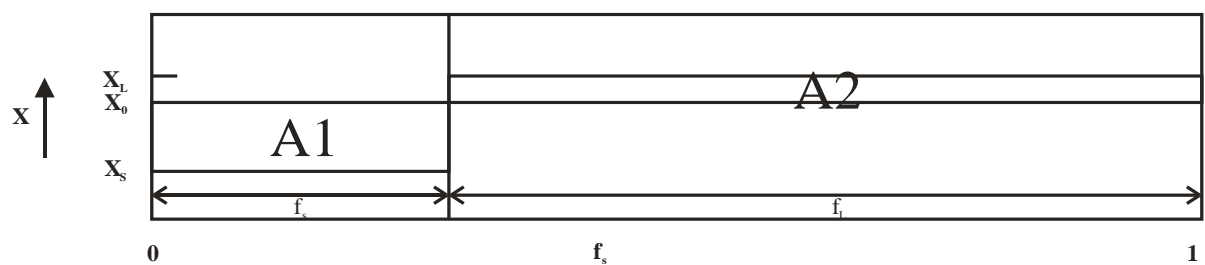
Figure 18. Schematic of a planer solidification front for an intermediate temperature T_2

In this case, there will be initial solute partitioning, however the infinite time for cooling and the solid state diffusion permitted will lead to no net segregation, as we start with $X_L=X_0$ and finish with $X_S=X_0$ throughout. Conservation of solute requires that the area A1=A2 (Figure 18), this follows from the equilibrium lever rule. This is shown in equations 8 and 9

$$(X_L - X_0)f_L = (X_0 - X_S)f_S \tag{8}$$

$$X_L f_L + X_S f_S = X_0(f_S + f_L) \tag{9}$$

The second case involves a situation, Figure 19, where the cooling rate is sufficiently high that there is no diffusion in the solid phase, which results in separate layers of solid which differ in composition; this is known as coring.
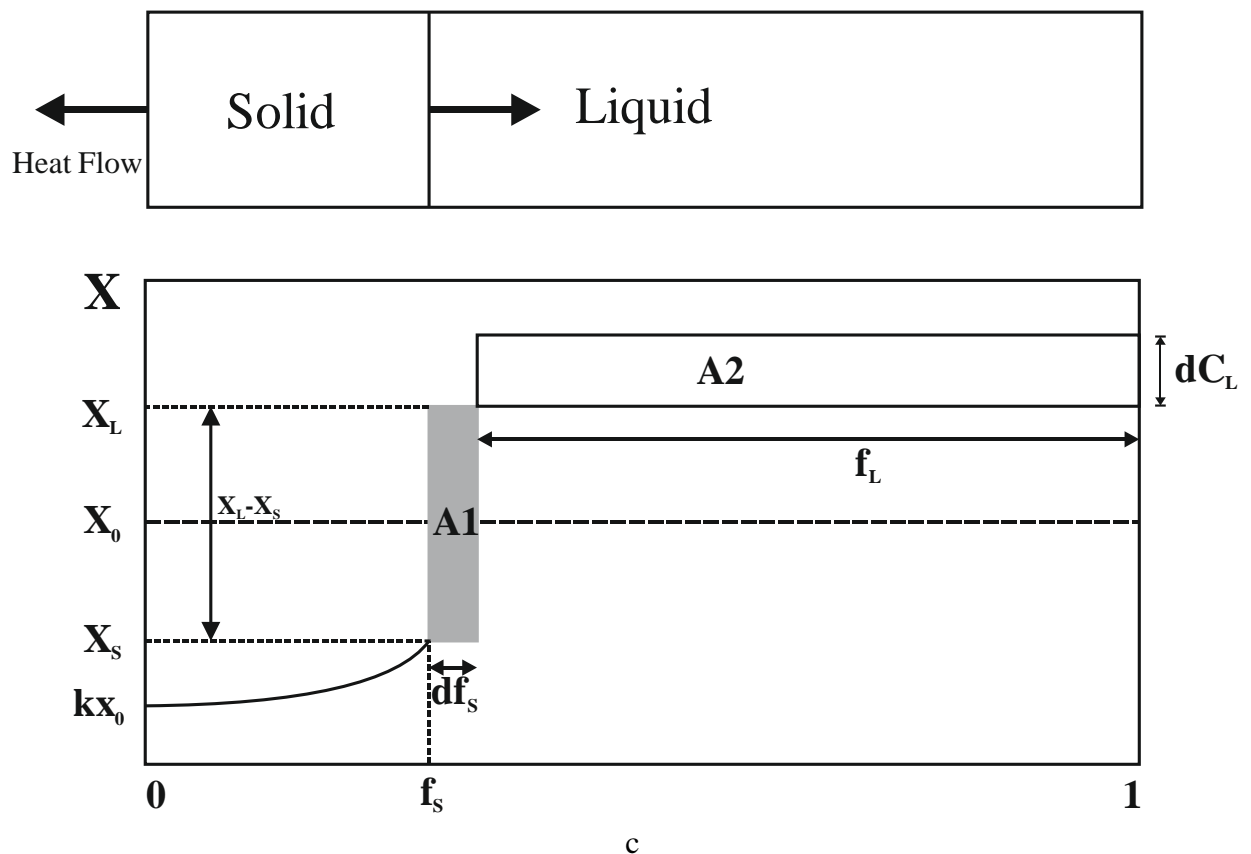
Figure 19. Schematic diagram and graph linking the planer solidification with the change in composition for a situation where there is no diffusion in the solid phase.

Continuing with the assumptions from before that there is a planar solidification front, as we cool the bar and reach T_1 the solid begins to form with composition kX_0. This concentration is lower in solute than the equilibrium concentration X_0. This means the new solid forming is purer than the liquid from which it solidifies, rejecting solute into the liquid and raising the remaining

liquid concentration further above X_0. Further cooling must therefore take place before solidification can continue; the new solid which forms has a higher concentration of solute. This sequence of temperature drop, solidification and solute rejection continues until solidification is complete. The composition of the solid and liquid at the interface at a specific temperature will be given by the equilibrium phase diagram, as there is no diffusion in the solid, this solid will contain the solute concentration it had at the moment of freezing. As a result of the non-equilibrium distribution of solute the mean composition of the solid is always below that of the solid/liquid interface. In order to calculate the relative amounts of solid and liquid at the interface, the mean solid composition and the liquid composition can be applied to the standard lever rule equation. The solute rejection into the liquid increases its concentration above X_0/k, tending towards the eutectic composition X_E at the eutectic temperature T_E where solidification is complete. In this case the final solid will have a eutectic structure.
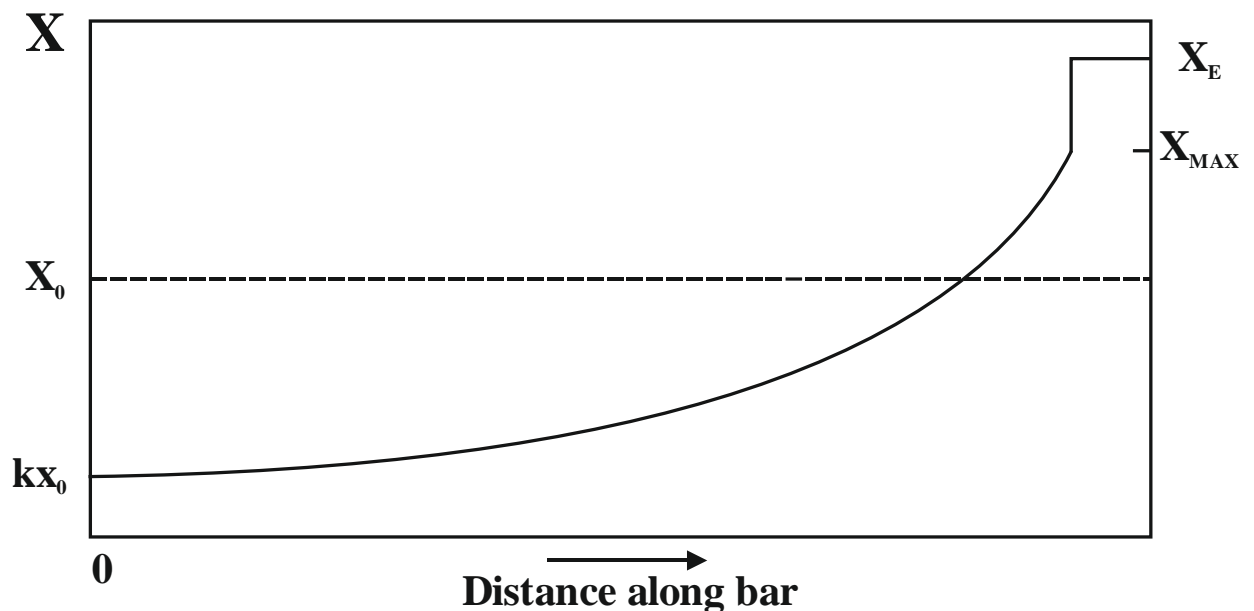
Figure 20. Schematic diagram showing the variation in composition which distance in a eutectic system as it solidifies.

The composition X_S varies along the solidified bar as shown in Figure 20, taking the whole bar the mean composition will be X_0. To calculate the composition of the solid X_S along the bar, again conservation of solute is required. As the rejected solute from the solid goes back into the liquid phase, A2=A1 in Figure 19.

$$A2 = A1 \tag{10}$$

$$(1 - f_s)dX_L = (X_L - K_0 X_L)df_s \tag{11}$$

$$\int_{X_0}^{X_L} \frac{dX_L}{X_L} = (1 - K_0) \int_0^{f_1} \frac{df_s}{(1 - f_s)} \tag{12}$$

$$[lnX_L]_{X_S}^{X_L} = (1 - K_0)[-ln(1 - f_s)]_0^{f_s} \tag{13}$$

$$X_L = X_0(1 - f_s)^{k_0 - 1} \tag{14}$$

$$X_S = K_0 X_0(1 - f_s)^{K_0 - 1} \tag{15}$$

This is known as the non-equilibrium lever rule or the Scheil equation.

The final distinct case of solidification is one with no diffusion in the solid and limited diffusion in the liquid, see Figure 21. As the melt cools below T_1 and solid begins to form, solute is rejected into the liquid phase but can only move into the bulk via diffusion which leads to a rapid increase in the local concentration ahead of the solidification front. This is known as the initial transient. If a constant rate of cooling is applied, the system will reach a steady state at the temperature T_3 where the liquid at the interface will have composition X_0/k and the solid forms with the bulk composition X_0. The conditions of steady state solidification require that the rate with which solute is rejected into the liquid phase is equal to the diffusion rate of the solute away from the solidification interface. In the final stages of solidification the remaining solute causes the concentration to rapidly increase to a eutectic composition X_E, which is known as the final transient.
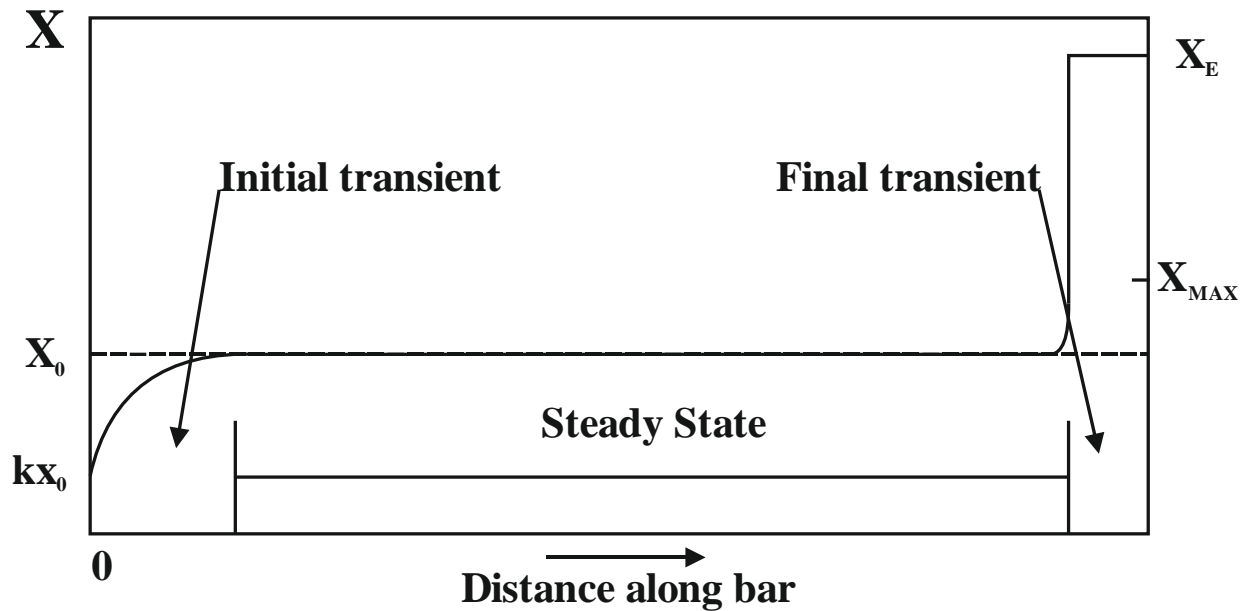
Figure 21. Schematic diagram showing the variation in composition with distance in a system where diffusion only takes place in the liquid phase.

The cases where we have solid forming sequentially with different compositions leads to a concentration gradient; when the constraint of planar front is removed and we return to more traditional nucleation and growth this concentration gradient manifests itself as coring or micro segregation.

The formation of dendrites occurs when the solidification front velocity (which is driven by the cooling rate) has a small temperature gradient the liquid ahead of the solidification front is constitutional undercooling. This results in the planar solidification front is no longer being stable leading to the formation of coarse cells, if the temperature gradient is further increased (solidification front velocity increased) these cells will further coarsen. When new coarse cell have large enough spacing then a temperature gradient can form between cells promoting the solidification and growth of new cells or secondary dendrite arms. If temperature gradient is increased above a critical value we no longer have constitutional undercooling and the formation of high curvature fine cells is more stable than dendrite forming coarse cell, if temperature gradient is increased even further a planar front again becomes most stable because of surface tension of the melt. The effect of cooling rate on the microstructure is that once a critical cooling rate is reached and constitutional under cooling is present, a planar front no longer forms and coarser (larger) the features will be formed and as the cooling rate increases until no constitutional uncooling is present these features become finer until the surface tension of the melt stabilises a planar solidification front. The cooling rate at which surface tension become

dominate will depend on the strength of the surface at the solidification temperature, the surface tension of metal and alloys is known to decrease as the temperature increases [113]. The surface tension is also strongly affected by the oxygen content of the melt where oxygen content of a few ppm can decrease the surface tension by several percent [114]

The velocity of the solidification front effects the solute partitioning of the alloy, when the velocity is high enough the solute partitioning ratio, at the growth front (k) is greater than 1, rather than being rejected ahead of the front the solute becomes trapped and part of the solid that forms. When k is less than one solute partitioning can take place, the lower k the higher the partitioning.

The formation of dendrites and the subsequent solute partitioning leads to concentration variation from centre to edge (with the composition of the dendrite arms different to that of the inter-dendritic spacing which will have a eutectic composition X_E) are all driven by solute rejection during solidification.

The use of a planar front to describe solidification behavior may appear to over simplify the situation. However on the macroscopic scale the primary and secondary dendritic arms can be seen to have a planar interface with the liquid, see Figure 22.
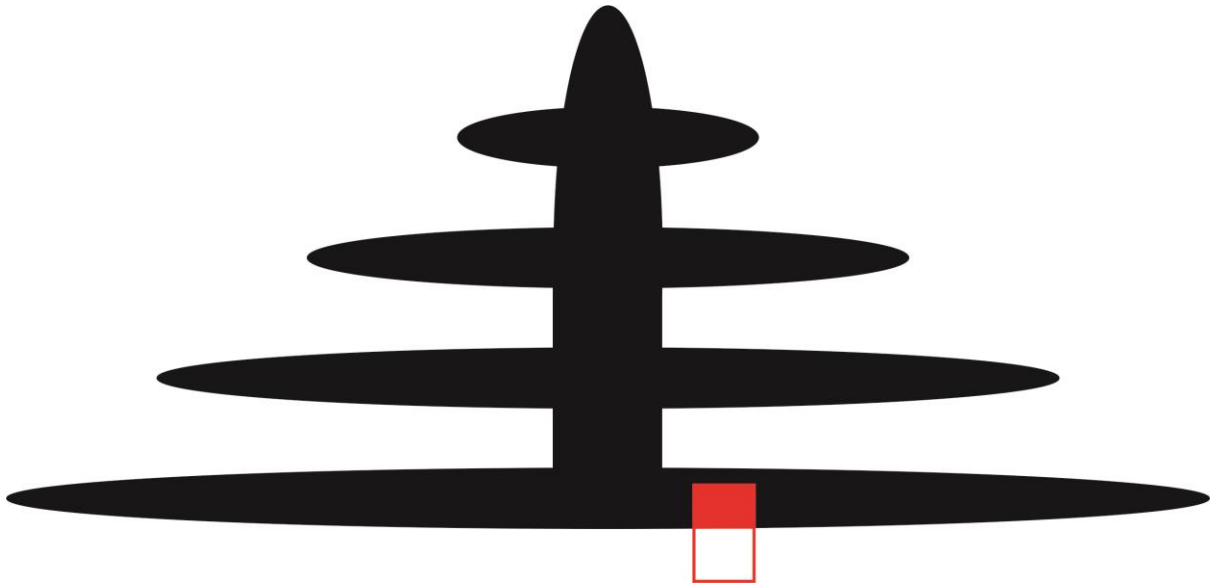
Figure 22. A schematic diagram showing how the planar interface is represented on a dendritic arm.
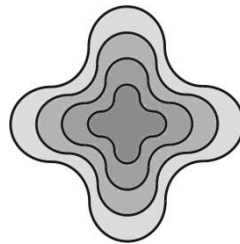
Figure 23. A schematic cross section of a dendrite arm to show the compositional change; different shades of grey represent the increasing level of solute concentration.

The three main factor effecting dendrite size are, the cooling rate on the alloy, a slow cooling rate will allow for dendrites to form and grow. Increasing the cooling rate leads to finer secondary dendrite arm spacing. Increasing the solute content will also lead to finer spacing, finally if the melt is agitated during solidification the dendrites can be broken up on formation this has the weakest effect on the dendrite spacing.

Solidification has only been discussed so far when it occurs homogenously in a free volume, in real life a foreign surface will always be present, i.e. a mould with nucleation occurring heterogeneously. As the melt cools the mould will cause nucleation on its surface in the chill zone (the area in contact with the foreign surface), once nucleation has occurred and heat is directional extracted from the melt a columnar zone is formed, with grains growing parallel to

the heat flow. In the center of the melt, if the under cooling is sufficient grains may nucleate and growth equally in area directions (equiaxed zone).

2.7.1   Binary Alloys

The simplest binary alloy is shown in, Figure 24 (1), a binary isomorphous alloy where complete solubility occurs of the two component metals. In some binary alloys, it is possible for a region of where they no longer form a solid solution and become immiscible, a immiscibility dome is formed in the phase diagram, see Figure 24 (2). It is possible for the immiscibility dome of a binary system to be expanded so that it intersects the solidus and form a simple eutectic This occurs when the components of the system have a maximum solubility in each other. As a result, the composition and temperature of the system dictate which phases form, see Figure 24 (3).
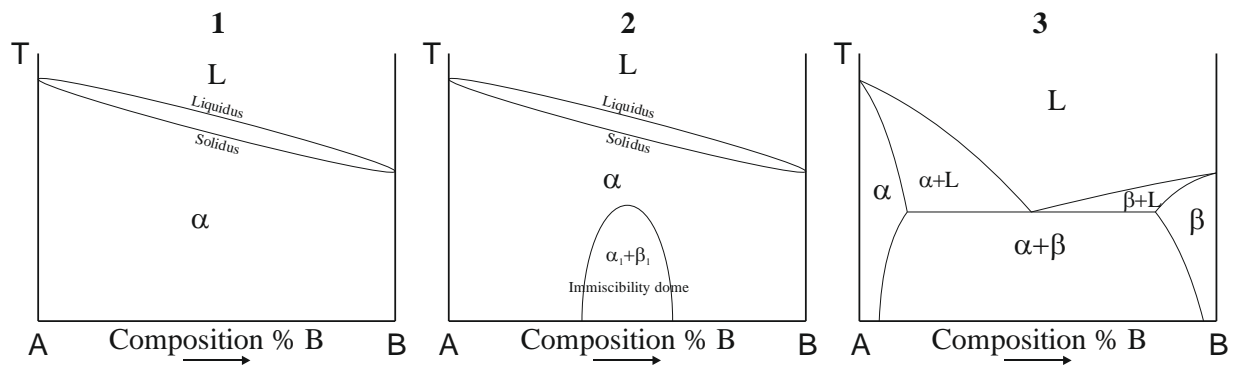
Figure 24. Schematic diagrams showing the evolution from a simple binary phase diagram (1) to one displaying a immiscibility dome (2) to a eutectic phase diagram (3).

2.7.2 Spinodal Forming Alloys

In order to separate the two phases in a binary alloy system it is possible to exploit the miscibility gap in the phase diagram, as this region has very unique properties, using a mechanism known as spinodal decomposition by which a two or more component system will phase separate into two chemically different and distinct regions. Figure 25 shows part of an idealised phase diagram to show where the spinodal region sits within a miscibility gap. It also shows the free energy change with concentration at T=T$_2$ and the spinodal region. Within the region between miscibility gap and the chemical spinodal large composition changes are needed for phase separation to occur the normal nucleation and grow route.
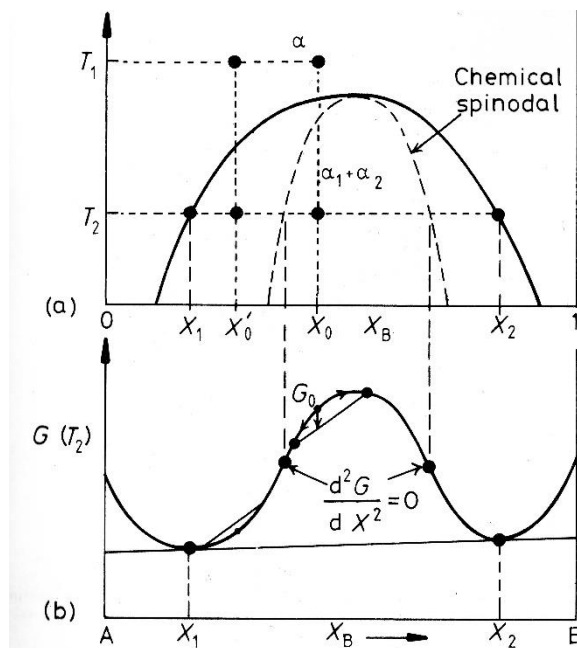
Figure 25. A schematic diagram of the spinodal region of a phase diagram with the corresponding free energy diagram [112].

The spinodal region of the phase diagram corresponds to the special segment of the free energy (G) versus concentration (X), where:

$$\frac{\partial^2 G}{\partial X^2} < 0 \tag{16}$$

Within the spinodal region, the second derivative of the free energy curve is negative.

When a homogeneous alloy is supercooled into the spinodal region extremely small compositional changes occur. These small compositional changes due to the free energy being negative result in uphill diffusion, and the system will spontaneously phase separate with no nucleation required as it is unstable. The driving force for diffusion can be affected by coherency strains which develop due to the variation in parameter that accompanies the variation in composition, slowing diffusion to maintain coherency. If the stain become incoherent the process of nucleation rather and spinodal decomposition will occur. When two phases separate by spinodal decomposition the compositional profile is sinusoidal [115] [88]. This phase separation has two regimes, in the first a dominate wavelength forms and the difference in concentration between the two phases increases exponentially, and is limited by the composition of the miscibility gap. If the alloy is aged coarsening will occur and the wavelength of the spinodal increased however the concentrations of the two phases will remain constant, typical wavelength are in the 1-60 nm range [88, 116].

2.8 Conclusions from the Literature Review

Following the review of available literature on the current production methods and properties of porous materials, it is clear that work in this area has focused on lower melting temperature metals such as aluminium. Figure 1 shows that the region of high melting temperature and lower density is an area that would benefit from further investigation.

The work that has taken place on higher melting temperature metals such as titanium and nickel alloys has taken alternative routes to overcome the challenges presented. In the case of nickel we discovered electrochemical deposition allowed for porous foam production based on a polymer substrate, however this is limited by the structures that can be produced in a polymer. The final size is also limited due the limitations of deposition methods to deposit deep inside large structures. In the case of titanium, porous structures are available in the form of cellular solids produced using additive manufacturing and powder processing methods. Additive manufacturing gives very good control over the final structure and properties but this control comes with a high cost. Powder processing methods are more difficult to scale up than liquid processing techniques. Several potential strategies for the production of foams based on high melting temperature metals have been suggested. Several of these are based on the principle of removing one phase from a multiphase material, this single phase can be one that is introduced externally to the system, or one that is intrinsically in the system.

The principle of dealloying also lends itself as a method for removing one phase from a multiphase system that has been designed to intrinsically separate, this route could offer the potential for several useful attributes. The need to join a porous structure to a solid substrate can be bypassed using this method, with a solid structural substrate that can be subsequently processed to present a porous outer structure by the removal of one of the phases. A search through binary alloy phase diagrams resulted in the alloy selected for investigation using the principle of dealloying to produce a porous metal was nickel-copper, the detailed justification for the section can be found in section 4.1. Nickel and copper are widely available for a competitive cost and while nickel is an allergen its alloys are not.

The process of replication could be adapted for use with metals that have a much higher melting temperature, where the substance removed is a phase that has been externally introduced to form a multiphase system. This process could lead to a low cost production route for high melting temperature porous metal structures where weight saving (from being porous) and ability to survive high service temperatures is of more benefit than the high cost structures that can

currently be produced. A search and down selection for compatible material pairs was conducted which met the criteria for replication casting, the metal selected was titanium 811 (8 wt% aluminium, 1 wt% molybdenum, 1 wt% vanadium, it is an aerospace titanium alloy with a relatively low liquidus of 1540°C (compared with 1660°C of Ti64). A preform material produced from sodium aluminate was selected as it is thermally stable to 1650°C and is water soluble, so easy of removal after infiltration, a detailed justification for the selection can be found in section 5. Titanium alloys have a higher cost than ferrous alloys due to their extensive use in the aerospace sector and the expense of processing, Ti-811 is of comparable cost to other titanium alloys, there are no safety concerns associated with the alloy. However, sodium aluminate is corrosive and can cause burns to skin PPE is recommended during handling.

3 EXPERIMENTAL METHODS

3.1 Arc Melting Procedure for Alloy Production

Small-scale arc melting was used for the production of both titanium and nickel based alloys. The procedure in each case was the same. The centre of the arc melter is a water cooled copper hearth, which has two recesses into which alloy components can be placed. A 12 g piece of CP2 grade titanium was placed in the chamber as a getter. This was positioned on one side with the required additaional elements for the alloy being produced on the other. The chamber was sealed and partially evacuated, and then back filled with argon. This process was repeated three times, and after the third time the chamber was evacuated to a pressure of 5×10^{-5} mbar. Once the chamber reached the required pressure it was then back filled with a small amount of argon in order for a directed electric arc to be formed. This was produced from an electrode in the top of the chamber and was directed manually. The voltage used was 550 V. The arc was first used to melt the titanium getter, so that it would absorb any contaminants which may still be present, and it was then used to melt the alloy components together. As the alloy forms an agglomerated mass, the electric arc was moved over the surface to help form a homogeneous mixture. This button of alloy cooled to a point when it no longer glows, and was then flipped over (all these operations took place in the chamber under evacuated conditions) the getter was again melted first, followed by the alloy button, which was again melted and mixed using the electric arc. The process was repeated a total of three times to ensure good mixing of the alloy components. The chamber was then brought back to atmospheric pressure and the alloy removed.

3.2 Titanium Alloy Production for Replication

The alloy used in replication casting, Ti 811 (8 wt% aluminium, 1 wt% molybdenum, 1 wt% vanadium and titanium to balance) was then produced by arc melting using the following method.

The titanium required was cut from a 25 mm bar of CP2 grade Ti, with the other required elements being weighed out to the correct proportions from 99.99 wt% pure sources. A full list of the exact weights used for each individual cast produced can be found in Table 4.

Table 4. The amount of each element used to produce Ti 811 for replication processing.

Sample	Ti (g)	Al (g)	Mo (g)	V (g)	Total (g)
1	6	0.53	0.07	0.07	6.67
2	8	0.71	0.09	0.09	8.89
3	8	0.71	0.09	0.09	8.89
A	8.27	0.74	0.09	0.09	9.19
B	8.33	0.74	0.09	0.09	9.26
C	9.32	0.83	0.10	0.10	10.36
D	9.73	0.86	0.11	0.11	10.81
E	11.29	1.00	0.13	0.13	12.54
F	9.52	0.85	0.11	0.11	10.58
G	11.95	1.06	0.13	0.13	13.28
H	5.57	0.50	0.06	0.06	6.19
I	4.3	0.38	0.05	0.05	4.78
J	5.4	0.48	0.06	0.06	6.00
K	5.9	0.52	0.07	0.07	6.56
L	6.7	0.60	0.07	0.07	7.44

3.3 Ni-Cu Alloy Production for Selective Phase Removal

The reasoning for the selection of a copper nickel alloy system can be found in following discussion chapter 4, Process Design and Alloy Selection.

The nickel-copper alloy was arc melted from 99.99 wt% pure elements in the amounts given in Table 5, to give a final composition of 65 wt% Ni and 35 wt% Cu. The alloy was then suction cast to produce a cylinder billet.

Table 5. The type and amount of each element used to produce the Ni-Cu alloy

Sample ID	Copper (g)	Nickel (g)
Rapidly Cooled and rapidly cooled and heat treated	3.5	6.5
Slow Cooled	3.5	6.5

3.3.1 Ni-Cu Heat Treatment

For this part of the investigation, rapidly cooled and heat treatment were required. Half of the rapidly cooled sample was removed and placed in a tube furnace under a flowing argon atmosphere and was heated at 5 °C/min to 950 °C, held for 1 hour, removed and ice quenched. The sample was then heated at 5°C/min to 345 °C in an argon atmosphere and held for 2 hours.

3.3.2 Slow Cooled Ni-Cu Sample Preparation

It was also desired to have samples with microstructures that were formed under slow cooling conditions. The restrictions of the arc melting equipment used for alloy production mean that it is impossible to cool a sample with anything other than an extremely fast cooling rate. In order to produce an alloy formed under slow cooling rate conditions, the sample was placed in a boron nitride boat inside a tube furnace in an argon atmosphere. The sample was inductivity heated above the liquidus temperature and allowed to cool and solidify under furnace cooled conditions.

3.4 Replication Casting

Replication casting was carried out based on the procedures reported in the literature ([47, 117]) with significant adaptation to the available equipment.

3.4.1 Preform Production

The sodium aluminate ($NaAlO_2$) anhydrous powder feedstock was supplied by Sigma Aldrich, with the composition given in Table 6.

Table 6. sodium aluminate preform feedstock

Compound	Amount (wt%)
Al_2O_3	50-56
Na_2O	40-45
Fe_2O_3	≤ 0.05

In order for the $NaAlO_2$ to be in a suitable form for processing the required foams (granular particles of around a millimeter in size) it first had to be made into a pellet. Using a 20 mm diameter stainless steel die, shown schematically in Figure 26, 2.0 g of powder was pressed under 4000 kg load to form a final pellet with dimensions 20 mm diameter and approximately 5 mm thickness.
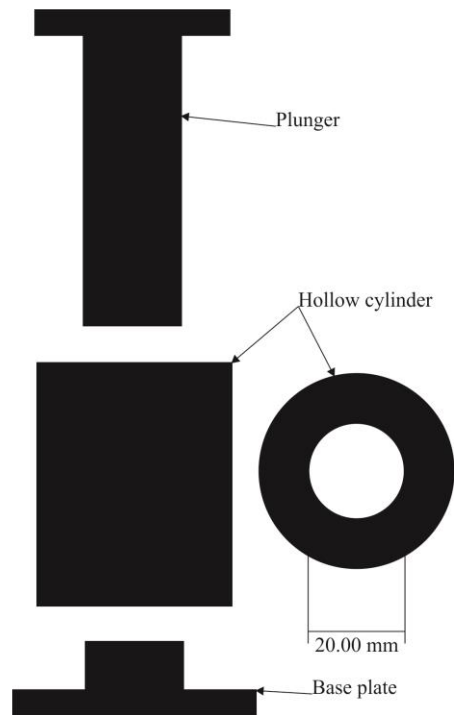
Figure 26. A schematic diagram of the 20 mm stainless steel die used for pressing pellets.

Different preparation methods were used depending on casting method, one smaller (1-1.18 mm) and courser (5 mm) sized particles. The following preparation methods were then followed, which were inspired by the processes reported in the literature [117].
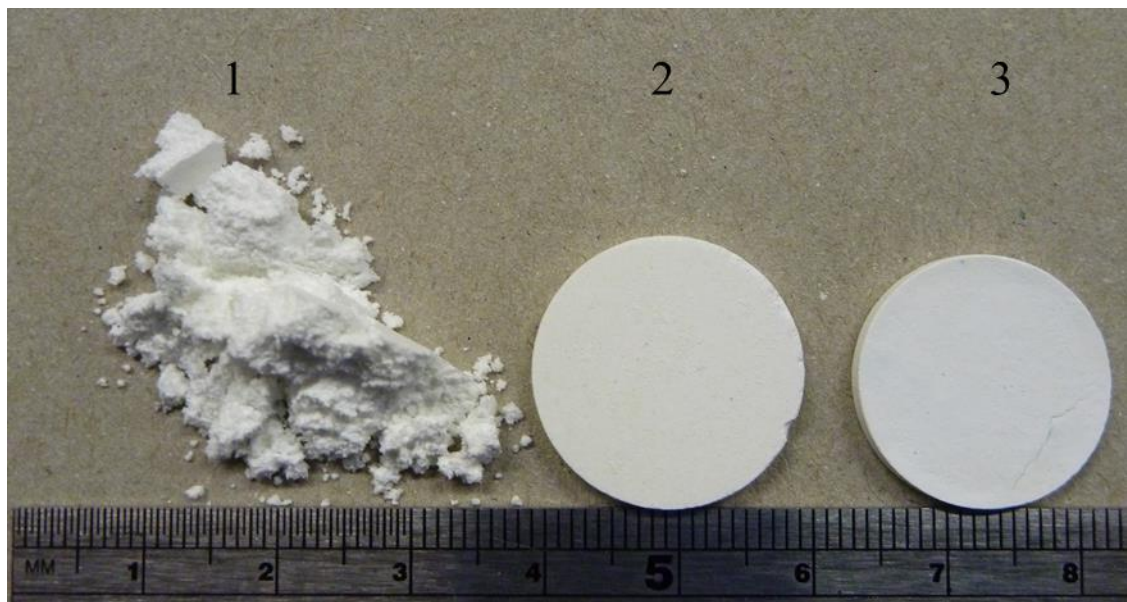
Figure 27. A photograph showing 3 steps in the NaAlO2 preparation, (1) powder feedstock () compacted powder (3) sintered powder compact.

Preforms which required a particle size of 1 mm - 1.18 mm, the powder feedstock, Figure 27 1) was pressed into pellets, Figure 27 (2), these pellets were sintered Figure 27 (3). For sintering the pellets were placed on an alumina block then into a tube furnace and heated using the following schedule: heating rate 6 °C/min (the maximum rate possible in the furnace) in air to 1500 °C, held for 3 hours and furnace cooled to room temperature.

The sintered pellets were then manually crushed and sieved, with particles in the range 1 mm - 1.18 mm selected and used in the next stage of preform production.

In order to create a stable sodium aluminate preform from the particles must be processed, to bond the particles together with sufficient strength for infiltration processing and to ensure that the pores created on infiltration would be interconnected a new final stage of the process had to be devised, differing from the method described in [117], which sinters the sodium aluminate into an alumina crucible prior to casting. For the preform shape used here, this sintering operation would need to take place while the sodium aluminate was in a copper mould, but the temperature for sintering (1500°C) far exceeds the melting temperature of copper (1040°C). The solution that was developed to solve this problem involved using the water solubility of the sodium aluminate and a fixed humidity environment [118] to adhere the particles together.

The copper mould was prepared for the preform by first cleaning using acetone and silicon carbide papers and polished with a diamond paste suspension (3 µm diamond particle size) to minimise contamination from previous casting trials. The copper mould was then filled with the particles of sodium aluminate and the whole assembly was placed in a large sealed glass jar. The inside of the jar was set to have a relative humidity of at least 95%, produced by placing in the jar with the assembly a saturated solution of potassium sulphate. The vapour pressure of the solution controlled the relative humidity in the sealed volume of the jar. The assembly was removed after 24 hours and placed in a drying oven at 50 °C for a minimum of 24 hours to dry out the mould and complete the adhesion of the particles into a usable preform, an example of which within the open mould assembly is shown in Figure 28.

Figure 28. Cross section of the mould assembly with the sodium aluminate in-situ.

For use in processing larger pore size foams (those using particles above around 5 mm^3) sintering of the particles was not necessary, as the compacted particles retained their shape at larger sizes. The pressed pellets were cut by hand to an approximate size of 5 mm^3, as shown in Figure 29.

Figure 29. NaAlO$_2$ particles prepared for use in production of a larger pore size foam. The particles shown have been through a casting cycle, but were then recovered as they were located at the bottom of the crucible and not reached by the metal.

3.4.2 Crucible Selection

A quartz crucible was used, which was selected as it has a high softening temperature (1683°C), low reactivity and being clear and colourless allows for the casting operation to be observed. A 2 mm hole was made in its base to allow gas flow out to prevent pressure build up during infiltration. During the process this hole was covered with 200 µm stainless steel mesh to prevent it being blocked by the sodium aluminate. The particles were then placed randomly by hand into the crucible, settling naturally to an approximate depth of 30 mm, as shown in Figure 30. The filled crucible was then left at ambient conditions (temperature and humidity) for at least 72 hours; due to the larger contact area between the particles a higher level of humidity was not required to bond the particles.
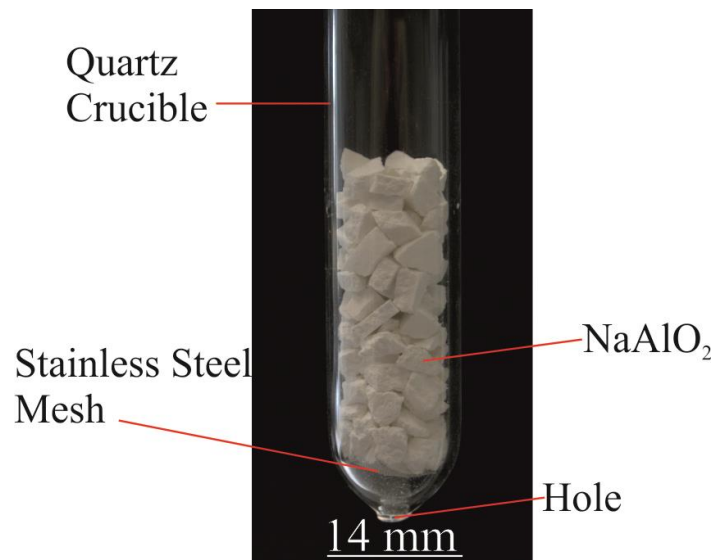
Figure 30. Quartz crucible with sodium aluminate preform material present.

For higher temperature infiltrations, an alternative crucible material was required with a melting temperature above that of quartz. For this purpose boron nitride was selected, as it is chemically inert, has excellent thermal resistance (disassociates at 3000 °C) and, importantly, can be hot pressed and machined into the required geometry. The boron nitride crucible was supplied by Almath Crucible Ltd, pressed and machined to the specification detailed in Figure 31, the dimensions of the crucible were set by the induction melting equipment available. The only dimension with scope for change was the height of the crucible, 70 mm was chosen as it allowed

for the clamp and the induction coil to fit along its length with only a small amount of crucible protruding from the coil, Figure 32.
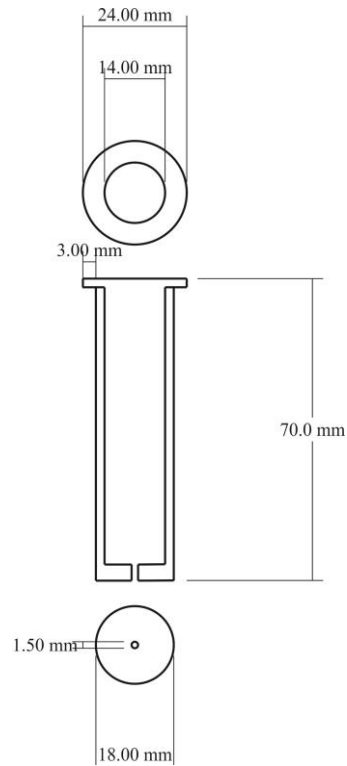
Figure 31. A schematic diagram showing the dimensions of the boron nitride crucible.

Figure 32. A photograph of a boron nitride crucible. This image was taken after an infiltration operation. The outside diameter of the crucible is 18 mm.

3.4.3 Replication using an Arc Melting Suction Casting

The casting procedure in the arc melting equipment uses suction to draw the molten alloy button into a copper mould; in the conventional process this mould is empty, but it can also contain a preform, as shown in Figure 28. The suction for the system is provided in two stages. The first is an evacuated cylinder of 25cm^3 volume (evacuated at the same time as the chamber during preparation for melting) which is connected to the bottom of the mould via an electronically controlled valve. The pressure difference between this cylinder and the argon back filled chamber acts as an initial draw on the alloy into the mould. The second stage is a vacuum pump attached to the opposite end of the evacuated cylinder to the mould, this acts as a constant draw on the molten alloy and acts to pull the alloy deeper into the mould/preform. Due to the nature of the equipment the alloy will be cooled quickly and can be removed within five minutes of casting.

The arc melter processing was used for the replication casting 4 times before being up scaled to the induction melter so that a larger sample could be cast. The conditions used each time are given in Table 7.

Table 7. Process conditions for arc melter replication casting.

Process Iteration Number	Mould Size (diameter mm)	Mass of Ti 811 (g)	Volume of Cylinder (cm^3)	Notes
1	6	6.67	25	
2	6	8.89	250	
3	6	8.89	250	Alloy Reused from casting 2
4	6	8.89	250	*

* A vacuum pump was added into the system to provide a constant draw on the molten alloy during the infiltration.

3.4.4 Replication using Induction Melting

In the induction melting system, rather than using vacuum to draw the metal into the mould against a fixed pressure behind the metal, pressurised gas was used to force the metal in against a fixed pressure within the preform (this is closer to the conventional infiltration process most commonly used in replication). The quartz crucible assembly used had approximately 12 g of Ti 811 alloy placed on top of the $NaAlO_2$ grains. It was clamped into the vacuum chamber of induction melting equipment (originally designed for melt spinning). The crucible was sealed and connected to an argon supply as to provide the infiltration pressure and push the alloy into the preform. The induction coil was placed around the crucible positioned so that the Ti 811 alloy sat at the centre of the coil. The chamber was sealed and flushed with argon three times before being pumped down to a pressure of 1×10^{-9} mbar.

The conditions for the induction melting and infiltration are summarised in Table 8.

Table 8. Conditions used for induction melting and infiltration

Induction Casting Iteration	Power (V)	Ar pressure (bar)	Crucible material	Ti 811 used (Table 4)
1	800	3 (burst)	Quartz	A
2	780	4 (burst)	Quartz	B
3	780	4 (flowing from the start)	Quartz	C
4	780	4 (flowing from the start)	Quartz	H+I
5	780	5 (flowing from the start)	BN	J+k
6	780	4 (Flowing from start)	BN	D
7	780	2 Flowing	BN	E
8	780	1 Flowing	BN	F
9*	N/A	N/A	BN	G

* A vacuum furnace was used to melt the alloy in this case so no induction melting or gas pressure was applied.

3.4.5   Alternative Infiltration Pressure Experiment

An alternative method for generating the infiltration pressure was attempted, using a boron nitride crucible prepared in the same way as when induction melting the alloy. In this case however the infiltration pressure was supplied by placing a tungsten slug on top of the alloy such that when the alloy melted it was pressed into the preform material by the weight of the slug. A 44 g tungsten slug (diameter 12.5 mm and length 18 mm) was used, calculated to exert a pressure of 353 Pa on the liquid beneath it. The crucible was placed upright into a vacuum furnace and heated at 10°C/min to 1600°C (with no dwell) and then furnace cooled to room temperature.

3.4.6   Post Casting Heat Treatments

In some cases it was necessary to heat treat the samples produced after replication processing. It was found after three castings that the alloy produced by replication processing was very brittle. In an attempt to reduce this problem, all castings produced after this point underwent a heat treatment, which was introduced as an aid to reduce any casting-induced residual stresses. The sample was left in the crucible in which it was cast and was placed into a tube furnace on an alumina boat. A heat treatment was performed in an argon atmosphere, with heating at a rate of 5°C/min to 650°C and held for 2 hours followed by furnace cool.

3.4.7   Sodium Aluminate Removal

The first stage in the conversion of the infiltrated sodium aluminate into a foam was the removal of the casting from the crucible. Where the two part copper mould was used, it would be separated and the infiltrated metal / sodium aluminate composite would be removed and placed into a heated (80°C) water bath until all the sodium aluminate was dissolved. The bath needed to be changed every 10 minutes to prevent the water becoming saturated. In the cases where the quartz crucible had cracked due to the thermal shock of the casting operation, it could be removed by hand without the need for the dissolution of the $NaAlO_2$ first. In cases where the crucible was still intact, the $NaAlO_2$ was first removed to facilitate the removal of the porous metal from the crucible. The crucible was clamped and lowered into a water bath at 80°C, heated by a magnetic stirring plate, and a magnetic flea was added to allow the bath to be stirred. The water in the bath was changed every 10 minutes to prevent it becoming saturated with $NaAlO_2$. The setup is shown in Figure 33.
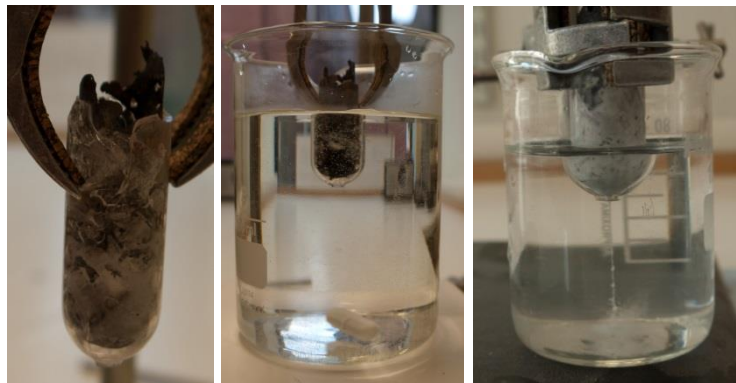
Figure 33. Three stages of NaAlO₂ removal.

Once a large proportion of the NaAlO$_2$ was dissolved away, the porous metal can be removed from the quartz crucible. Residual NaAlO$_2$ was removed by placing the sample immersed in water in an ultrasonic bath for up to 8 hours; again changing of the water in the bath was required to avoid it becoming saturated. The degree of saturation was monitored with a simple pH test as a strong alkaline solution (NaAl(OH)$_2$) forms when NaAlO$_2$ dissolves in water (equation 17).

$$NaAlO_2 + 2H_2O \rightarrow NaAl(OH)_4 \hspace{3cm} (17)$$
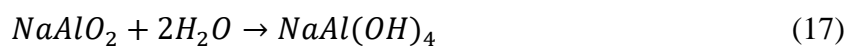
3.5 Selective Removal of Copper

To create a porous metal through this route, the copper rich phase must be removed from the nickel-copper alloy to leave behind the nickel rich phase. In order to remove the copper rich phase from the alloy a suitable etchant (one which would more aggressively and preferentially remove copper from the alloy system), was used. Samples were metallographically prepared to the mirror finish before etching. Alcoholic ferric chloride (reagent grade supplied by Sigma Aldrich) was selected. Each sample was submerged in ferric chloride for 5 minutes, after which it was removed and washed with distilled water. The samples were then wiped repeatedly for 5 minutes with a ferric chloride saturated cotton swab, followed by another wash with distilled water.

3.6 Metallographic Preparation

Samples were prepared using the following procedures for a variety of analysis techniques that required a flat polished surface, including EDS and hardness mapping Where preparation methods differ from these for specific samples it is clearly mentioned in the text. Samples approximately 5 mm thick were cut using a BUEHLER Isomet 5000 precision linear saw. The samples were mounted into 32 mm conductive phenolic resin discs, and were then ground using progressively finer silicon carbide papers (starting at 400 grit, followed by 800 and finally 1200 before moving onto polishing). The samples were then polished using successively finer diamond paste grades, 9 µm, 6 µm, 3 µm and 1 µm, in some cases ¼ µm being used. Porous samples for required mounting using vacuum infiltration of an epoxy resin in a vacuum infiltration unit (Struers Citovac), as the pressures used when mounting in phenolic resin could collapse the porous structure of the sample.

3.6.1 Titanium Etching

In order to reveal the grain structure, the titanium based alloy samples were etched using Kroll's reagent (3 vol% hydrofluoric acid 6 vol% nitric acid and distilled water to balance), the sample was immersed for 15 seconds removed and immediately washed with distilled water.

3.7 Optical Microscopy

The samples were imaged using a Nikon Eclipse LV150 light microscope with images taken in both light field and dark field (the default choice was to use light field; images that were taken in dark field are specified). Etched samples were viewed in profile to measure the depth of the porosity present.

3.8 Scanning Electron Microscopy (SEM) and Energy Dispersive X-Ray Spectroscopy (EDS)

3.8.1 SEM imaging

As the samples had been mounted in conductive resin, there was no need to apply an additional conductive coat to allow SEM imaging. Images of samples were taken using a Joel 6400 Scanning Electron Microscope; general conditions used for imaging were an accelerating voltage 15 or 20 KV with a working distance of between 15 mm to 18 mm, to allow a large field of view.

3.8.2 EDS Mapping

Energy Dispersive X-Ray Spectroscopy (EDS) was used to identify the type and location of elements present within a sample. When a sample is bombarded with electrons in the SEM these primary electrons excite the electrons in the atoms of the sample promoting them to a higher energy level. When the electrons in the atom drop back to their ground state they release an X-ray with a specific characteristic frequency. This X-ray is picked up by the detector and used to identify the atom and its location on the sample.

The mapping process took place at various magnifications and locations to identify the distribution of elements within the sample. Each sample was scanned for at least 15 passes of the electron beam to build up a comprehensive image of the sample.

3.8.3 EDS Quantification

A quantification analysis and EDS element mapping of a selection of the samples was made using a turreted Pentafet detector and ISIS 300 processing unit on the EDS system in order to determine the amount of copper and nickel present. This information was then used to investigate the solidification behavior of the samples. The EDS detector was calibrated using a cobalt standard, software corrected and recalibrated every 5 scans. The quantification scans measured the composition of a 28 μm^2 area. A minimum of 50 scans from random locations on each sample were made, the results used to create a graph plot of increasing copper %.

3.9   Porosity Measurement

In order for the level of porosity in the samples to be measured the volume fraction of the porous phase was calculated using a manual point counting method. In this method a grid is placed over an image of the sample, and when the phase being counted (in this case a pore) falls on an intersection it is counted as 1, those in the bulk are counted as 0 and any point lying on the boundary are counted as 0.5. From this point fraction the volume fraction of the second phase (the porosity in this case) can be calculated. The selection of the grid size is very important in maintaining the statistical integrity of the method, as no single feature should be measured more than once. To ensure this occurs, a grid size in selected so that the spacing is as large as the largest feature (pore). This method allows for the mean porosity to be calculated along with the standard deviation, and from these the standard error and the 95% confidence limits (using the relevant t-value) can be calculated [119].

The standard error in the result is given by:

$$S(\bar{P}_P) = \frac{s}{\sqrt{n}} \tag{18}$$

The porosity is then given in the form:

$$V_V = \bar{P}_P \pm (t_{95n-1})S(\bar{P}_P) \tag{19}$$

A manual method was used instead of computer based image analysis as in some cases the pores do not form a clear and definite boundary as some of the porosity presents as only shallow pores, in these cases the image analysis software may consider these not to be pores and discount them. Other analytical techniques such as pycnometry and porosimetry for accurately measuring the volume and the mass of the sample are used to calculate the density, and how that density varies from the reference value of the bulk (i.e. non-porous) material equates the level of porosity in the sample. These two methods rely on the whole sample, not just the surface, being porous, which means that these techniques were not appropriate for measuring surface (not volume) porosity which has been produced. X-ray tomography is a more advanced technique which could also be applied to measure the amount of porosity in a sample [9] and is a very valuably technique for

advanced characterisation of a porous structure, however this is again best suited to measurement of a sample with is completely porous and not just the surface.

3.10 Hardness Testing

Hardness testing was conducted on the arc melter produced samples of nickel-copper alloy with rapidly cooled, rapidly cooled and heat treated sample and the slow cooled sample using a Struers DuraScan 70 with Vickers pyramidal indenter. All the tests were conducted after the copper rich phase had been etched away, in order to assess the apparent hardness of the resultant porous structure. The scale of the indents applied was significantly larger than the scale of the porosity, so this type of test would be expected to be representative of the compressive strength of the porous material [15]. SEM images of the indents produced were also taken to view the deformation mechanisms operating and to assess the precise location of the indent with reference to the porous structure. Hardness measurements were taken using the scheme outlined in Table 9. The loads used were 1 kg (HV1), 2 kg (HV2) and 3 kg (HV3), with a dwell time of 5 s, the grid size was determined experimentally in order that the indents were located with a separation of at least 3 times the indent diameter.

Table 9. Parameters used in the hardness testing of etched NiCu samples

Sample	HV	No. Points	Grid size (mm)
Rapidly cooled	HV1	25	0.2×0.2
	HV2	10	0.5×0.5
	HV3	5	0.3×0.3
Rapidly cooled and heat treated	HV1	25	0.4×0.4
	HV2	10	0.5×0.5
	HV3	5	0.5×0.5
Slow cooled	HV1	25	0.2×0.2
	HV2	10	0.4×0.4
	HV3	5	0.5×0.5

3.10.1 Hardness Mapping

The slow cooled sample of the nickel-copper alloy was used before etching to produce a hardness map, to see if the copper-rich and nickel-rich areas of the sample could be identified purely based on the variation in hardness caused by the partitioning into two phases.

A hardness map was produced using a Struers DuraScan 70 with a Vickers pyramid indenter, making a series of 100 indents in a 10×10 grid. The Struers DuraScan software automatically calculates hardness via image analysis of the indents produced, some user input was required when it is unable to resolve the image and measure a diameter. The mapping was conducted in 2 locations on the sample. Indents were spaced 60 µm apart centre to centre and were made using 10 g load (HV0.01) for 5 s dwell and observed using an 80× objective lens. The smallest load (10 g) of this machine was used and spacing used ensured that the indents had the required 3d separation to prevent inference from one indent to the next.

4 SELECTIVE PHASE REMOVAL IN A NICKEL-COPPER BINARY ALLOY RESULTS AND DISCUSSION

The following chapter describes the results obtained in the Selective Phase Removal section of this work, and subsequently discusses the findings, focusing on characterising the microstructures produced in the Ni-Cu alloy investigated, and how those structures relate to the potential production of a high melting temperature metallic foam.

The first step in assessing the feasibility of this route for the production of porous high melting temperature metal structures was to focus on the capability to produce the precursor alloy with the required microstructure. The processing of the alloy did not pose any significant problems for technical feasibility, the base elements of copper and nickel were readily available at high purity (99.9+ %) in a wide variety of shapes and sizes, neither are particularly rare or expensive.

In this case the production of the alloy was successful, with the material being cast into a cylinder (8 mm diameter). The use of arc melting as performed here was appropriate for a small volume of material for research purposes. Other vacuum arc melting systems are available, that are more suited to large industrial scale operations, for example Consarc (www.consarceng.com) offer vacuum arc remelting furnaces with capacity up to 30000 kg.

4.1 Process Design and Alloy Selection
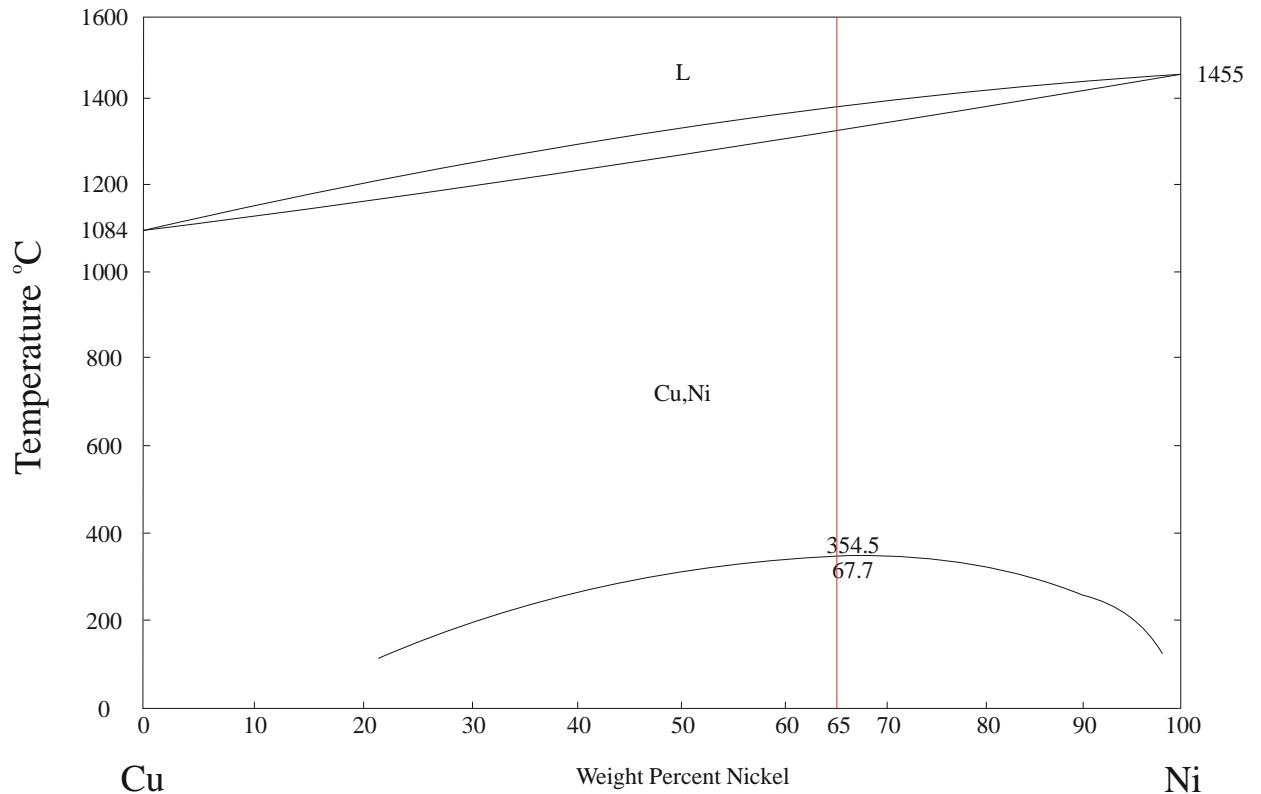
Figure 34. Nickel Copper phase diagram [120].

The aim of the Selective Phase Removal process designed, was to generate a controlled two phase microstructure, where the two phases were mutually interpenetrating and continuous (essential for one of them to be removed leaving a coherent material). If this structure could be obtained in an alloy system where one of the phases could be removed by chemical action while the other was relatively unaffected it would be possible to create an open porous network. The method is similar to dealloying, except that the phase separation has already taken place. This brings the added advantage that the understanding of microstructural control developed over centuries of metallurgical processing can be used to affect the precursor structure and hence the final foam structure to a large degree.

Nickel-copper alloys were explored, as these show a miscibility gap in the phase diagram see Figure 34 and generate two phase microstructures by spinodal decomposition. The alloy composition chosen for investigation had a composition of 65 wt% Ni, 35 wt% Cu. The equilibrium solidification path for the alloy has the composition of the first solid to form 80 wt% Ni, 20 wt % Cu, with the last liquid to solidify having a composition of 49 wt % Ni, 51 wt% Cu,

this gives the solid a potential 31 wt % composition range. During equilibrium solidification the copper concentration along the length of dendrite arms with vary from 20 wt% to 51 wt%.

The 65 wt% Ni, 35 wt% Cu composition rather than a 50/50 composition sits very close the peak of the miscibility gap of the phase diagram at 67.7 wt% nickel. The heat treatment of the rapidly cooled sample would take place within the miscibility gap to enhance the likelihood of phase separation. This low copper composition was chosen as it provides a microstructure to produce low porosity structures if only the copper is removed, but also provides an opportunity for foams to still be made if the phase selectivity were not to be perfect and there was some removal of nickel during the dissolution process.

4.1.1   Alloy Composition and Segregation

Samples of the 65 wt% nickel – 35 wt% copper alloy were produced using three different solidification regimes, rapidly cooled, rapidly cooled followed by heat treatment and slow cooling from the liquid state, as detailed in the experimental methods. This was intended to achieve different microstructures.

The rapidly cooled and the slow cooled samples would allow the solute partitioning to be compared at the extremes, with the heat treatment offering information on diffusion-controlled changes that can occur during a post casting heat treatment to increase the elemental separation, possibly facilitating the second phase removal stage.

4.2 Microstructure of the Nickel-Copper Alloy Produced

The alloy was sectioned, polished and examined at low magnification in the SEM, after treatment with ferric chloride to remove the copper rich phase to produce a porous structure.

4.2.1 Rapidly Cooled Sample

The casting operation was performed in equipment designed for the rapid cooling required to produce bulk metallic glass. When casting a relatively large diameter (for the equipment) ingot, as performed here, the cooling rate experienced will decrease with distance from the outside cooling surface to the centre of the ingot. This is expected to have an impact on the scale of the microstructure and also produce directional columnar growth towards the centre section.
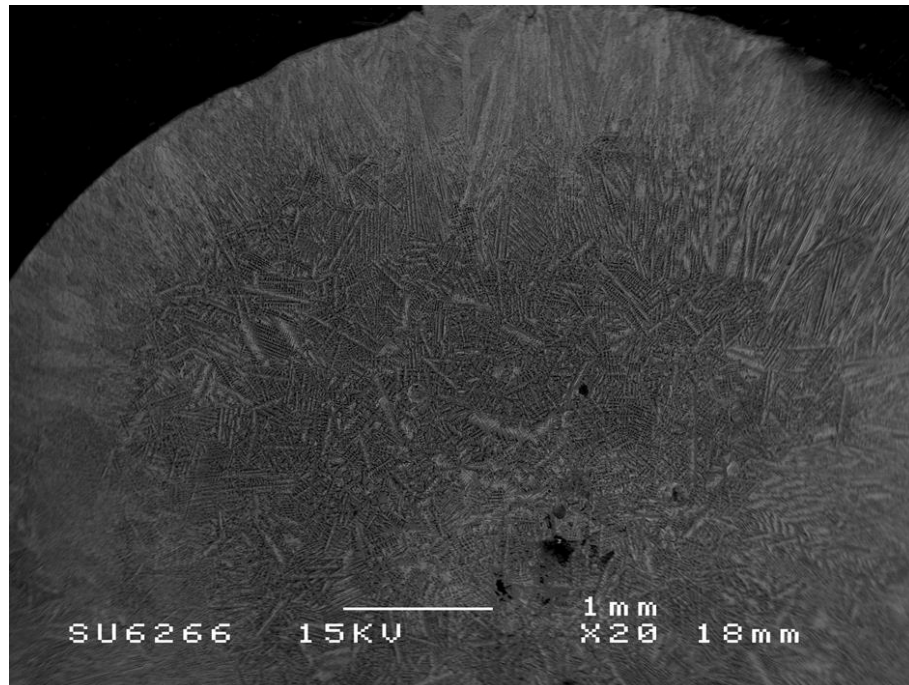
Figure 35. Low magnification SEM image of a cross section of the rapidly cooled sample after etching to reveal the microstructure, highlighting the change in structure from edge to centre.

A visual assessment of the central region of the casting showed some large pores (visible in Figure 35) which are not unexpected in an ingot produced in this manner. Primary dendrite growth can be seen to extend approximately 1 mm from the edge towards the centre after which a region of random dendritic growth occurs with secondary dendrite arms forming. As would be expected, the scale and directionality of the microstructure were controlled by the solidification conditions, within a sample of small volume.

4.2.2 Rapidly cooled followed by Heat Treatment Sample

A section was taken from the rapidly cooled ingot and heat treated. As such, the rapidly cooled sample acted as a direct comparison to demonstrate the changes in the microstructure that has been induced by the heat treatment.
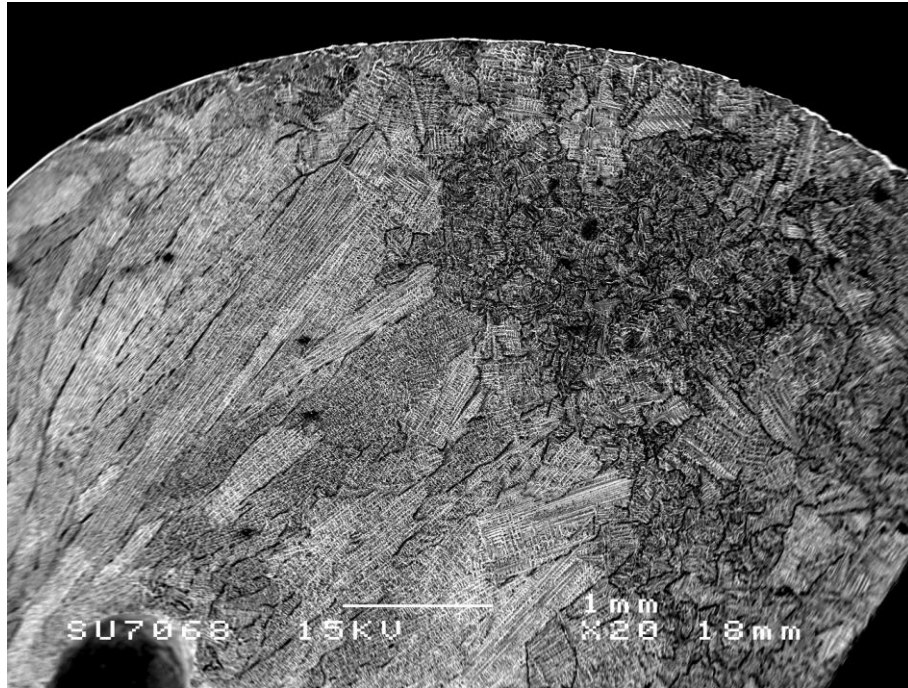
Figure 36. SEM image of a cross section of the rapidly cooled followed by heat treatment sample. This sample has been etched to reveal the microstructure.

It is clear from Figure 36 that the microstructure of the sample had undergone a change from the pre heat treatment structure; some columnar grains have transformed and columnar regions had grown in size.

4.2.3   Slow Cooled Sample

In order to proces a sample which had under gone a slower cooling rate, the alloy was first cast into 8 mm diameter ingot in the same process as the rapidaly cooled sample. The ingot was then remelted using an induction furnace under an argon atmosphere and allowed furnace cooled to room temperature, this processed formed in a round button shaped sample. A cross section through the centre was used for further analysis.
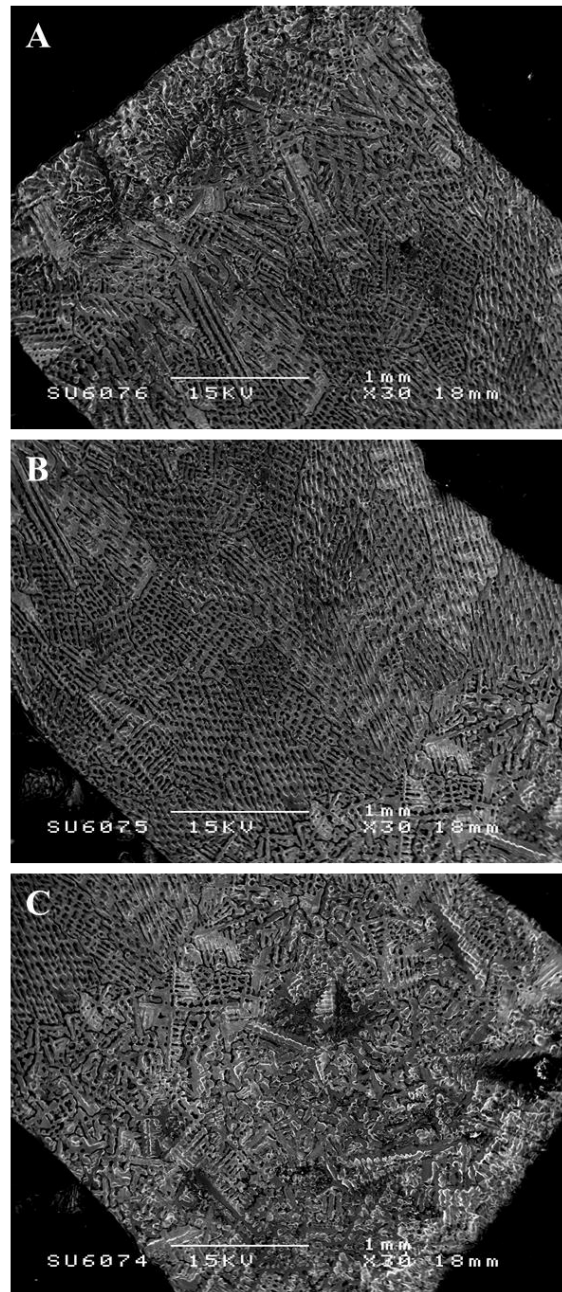
Figure 37. SEM images of the cross section through the slow cooled sample, after etching. A) showing one surface, the middle section in B) and C) showing the surface on the opposite side of the section.

The outer region of a sample in contact with furnace environment must experience the fastest cooling rate. This can be seen in Figure 37A, with the slowest cooling rate occurring in the center of the sample. This variation of cooling rates had produced a variety of solidification structures. In the outer regions, dendrites are visible, with regions of columnar structures towards the center. There may also be differences in composition that accompany this. The other edge of the sample shown in Figure 37C, shows the same random dendritic. The depth of the random growth extends approcimately 3 mm into the sample where in the other edge it only extends approximately 1 mm into the sample. This is an indication that even in a relatively small sample size, the cooling rates experienced at different points around the sample varied enough to produce different final microstructures. The central portion of the sample (Figure 37B) experienced the slowest cooling rate; this would be expected to result in the longest time being available for the copper to partition to the interdendritic spaces.

The mould used to cast the samples gave a small flash gap between the two halves. The material in this section (Figure 38) experienced a greater rate of cooling and had a structure with very clear directionality, with columnar growth extending from the surface to centre, again terminating in a central region containing dendrites with secondary and some tertiary arms present.
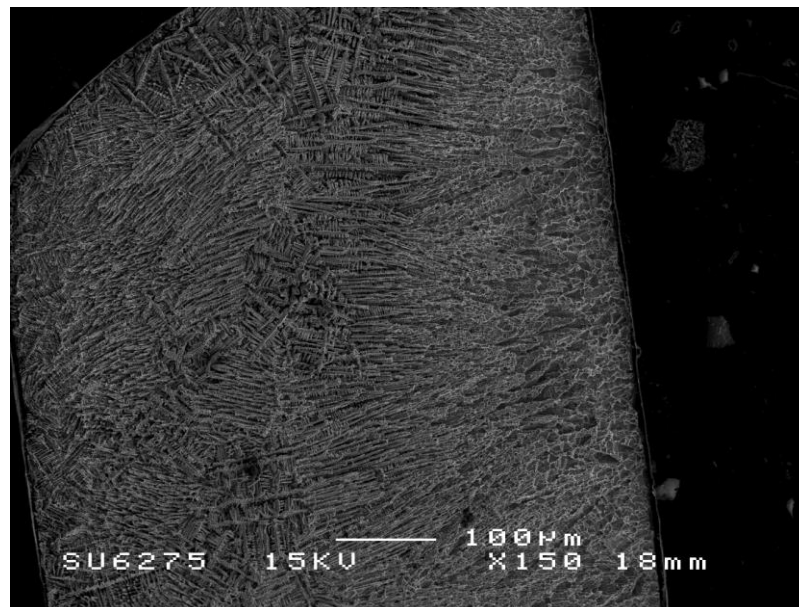
Figure 38. SEM image of the flash region of the two part mould, which displays a large percentage of columnar growth.

On closer inspection the columnar growth was established after approximately 100 μm, see Figure 38.

4.3   Segregation in the Alloys

To remove one phase with good selectivity, it would be important to get good discrimination in the compositions formed before starting dissolution, which in the system investigated would involve the segregation occuring on solidification or subsequent heat treatment.

The solute partitioning and compositional changes of the alloy were investigated using quantitative EDS analysis on samples produced using the three solidification regimes. Each sample had been polished to a mirror finish such that no surface features could be visually identified and influence the sampling or the measurement. Spot analysis (28 µm size) of the composition was performed at 66 random points on the surface of the sample, and these results were then ranked according to the copper content. The theory is that a random selection of points will represent alloy that solidifies at different, random stages in the transition from liquid to solid (some spots will lie in the core of dendrites, being the first solid to form, and some will lie in the interdendritic regions, being the last), and when placed in ascending order should represent the concentration change with distance along a directionally solidified specimen, as predicted by the Scheil equation. In a real, non-directionally solidified specimen, the Scheil equation prediction represents the change in composition that would be expected going from the centre of the primary dendrite arms (the first material to solidify) into the inter dendritic region (the last material to solidify), and hence the solute partitioning that has occurred during the solidification process. A difference in solute partitioning has been measured using this method and is presented in section 4.3.

In parallel with this, EDS mapping was performed; and these results will be discussed with the quantitative EDS results. The rapidly cooled sample is used as a base line comparative sample, followed by the rapidly cooled and heat treated sample, so that the effect of the treatment can be observed, and finally results from the slow cooled sample will be presented.

EDS area mapping was performed at random locations, these maps were used to visually show the extent of the solute partitioning, and to identify the length scale on which it is operating. The same colour reference is used on all maps and separate maps were used to show nickel in red and copper blue, the concentration of only the element being examined is shown on the map.

4.3.1 Rapidly Cooled Sample

The rapidly cooled sample shows the smallest variation from the bulk concentration of the alloy in the compositions of the randomly located test points, Figure 39.
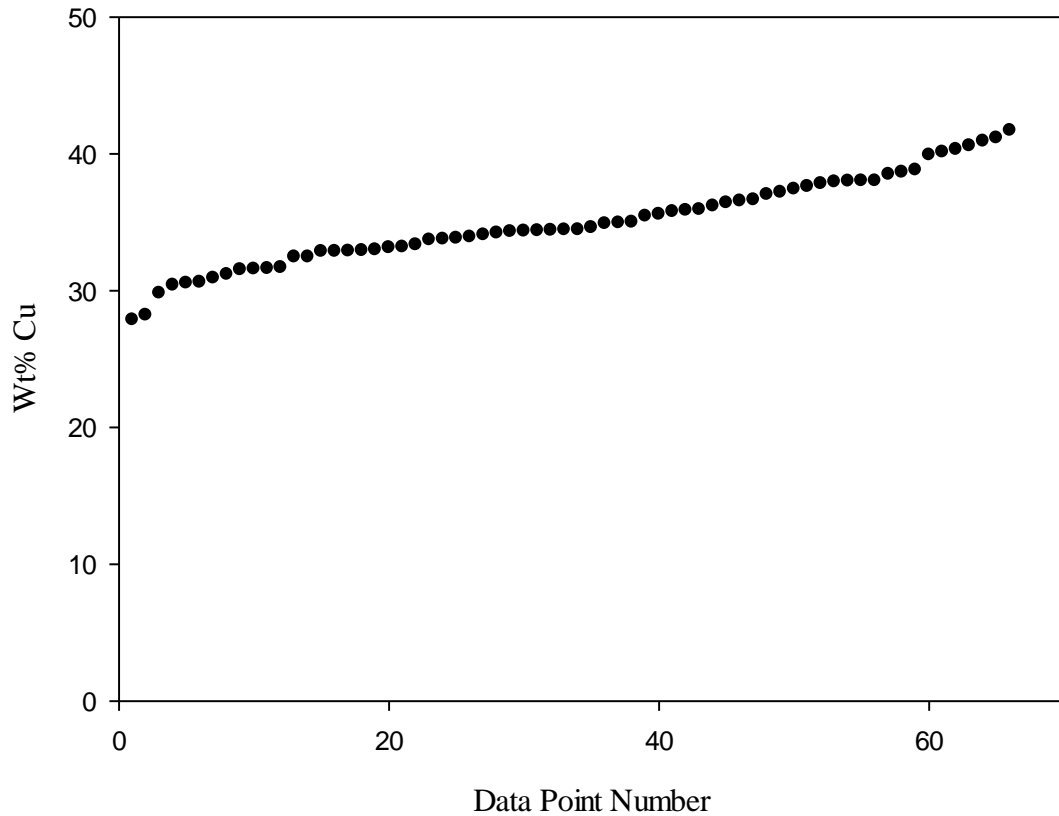
Figure 39. Quantitative EDS analysis of the arc melted rapidly cooled sample. The data has been presented in ascending copper concentration.

The quantitative EDS mapping of the sample, Figure 39, shows the extent of solute partitioning is limited, with the weight percent of copper ranging from 27.86 wt% to 42.71 wt% (alloy mean 35 wt%). There is a difference of 13.85 wt%, between the low and high measured concentrations of copper. From the phase diagram, the first material to solidify is copper poor, and the concentration rises as this element is rejected into the liquid. This variation is expected as the rapid cooling results in a fast-moving solidification front so that there is insufficient time for diffusion in the solid phase and very limited diffusion in the liquid phase, the composition everywhere similar to the bulk.
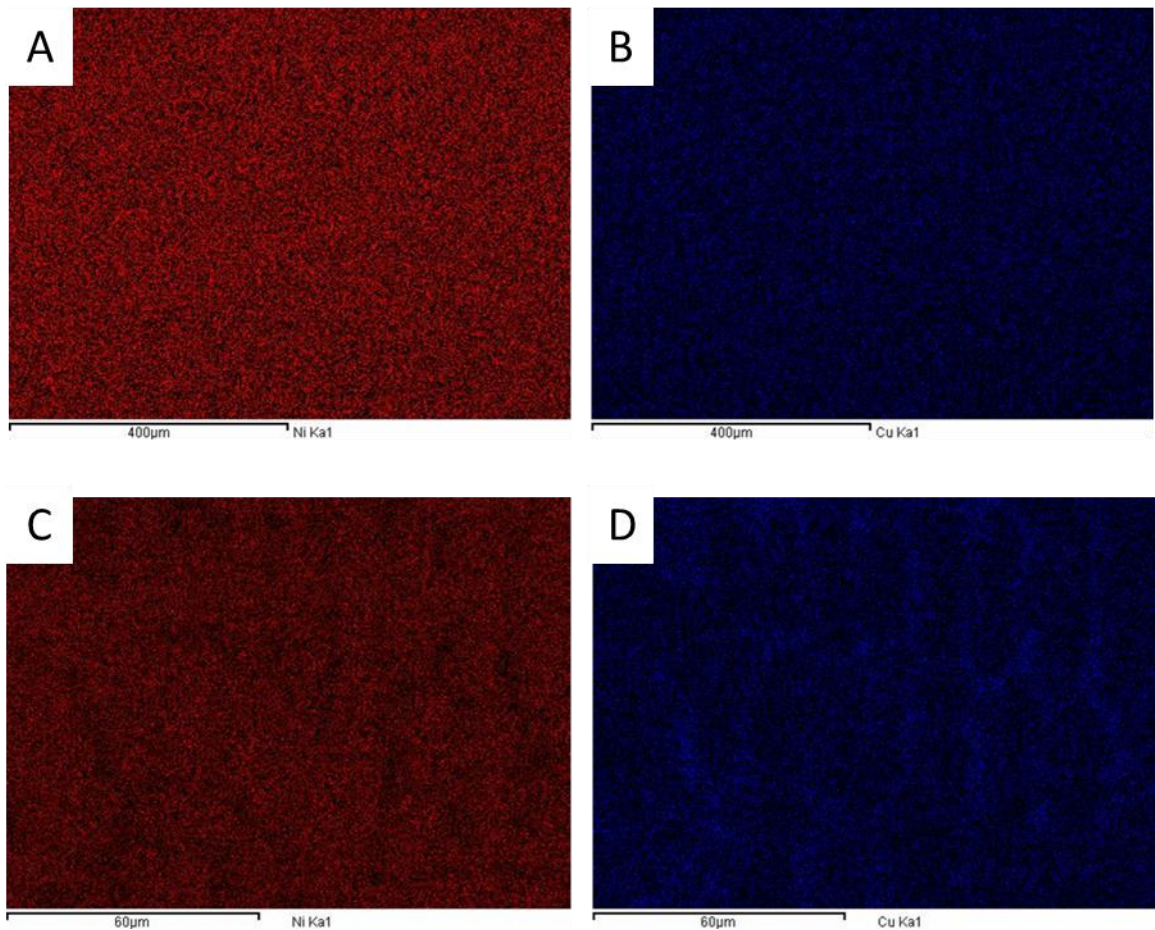
Figure 40. EDS maps of the rapidly cooled sample. Shown at low magnification in image (A) and (B) highlighting the nickel (red) and copper (blue) respectively. Shown at higher magnification in image (C) and (D) highlighting, the nickel (red) and copper (blue) content respectively.

The EDS maps shown in Figure 40, at low magnification ((A) and (B)) appears show a relatively homogenous distribution of copper and nickel in the microstructure. This indicates that the difference in the concentration of copper and nickel recorded by the quantitative data occurs over a fine scale (see the higher magnification maps Figure 40 (C) and (D)), as the maps are uniform and the imaged locations were selected at random, it is likely to be evenly distributed over the whole sample.

The higher resolution scan shown in Figure 40 ((D) and (E)) a shows regions of segregation with complementary regions of low copper and low nickel content now showing on the pairs of maps generated by the scans. However, there is no sharp definition between the regions with some significant amount of the second element always present in either phase.

4.3.2   Rapidly Cooled and Heat Treated Sample

Rapid cooling followed by the heat treatment results in similar variation in bulk concentration as that seen in the alloy which was only subjected to rapid cooling,
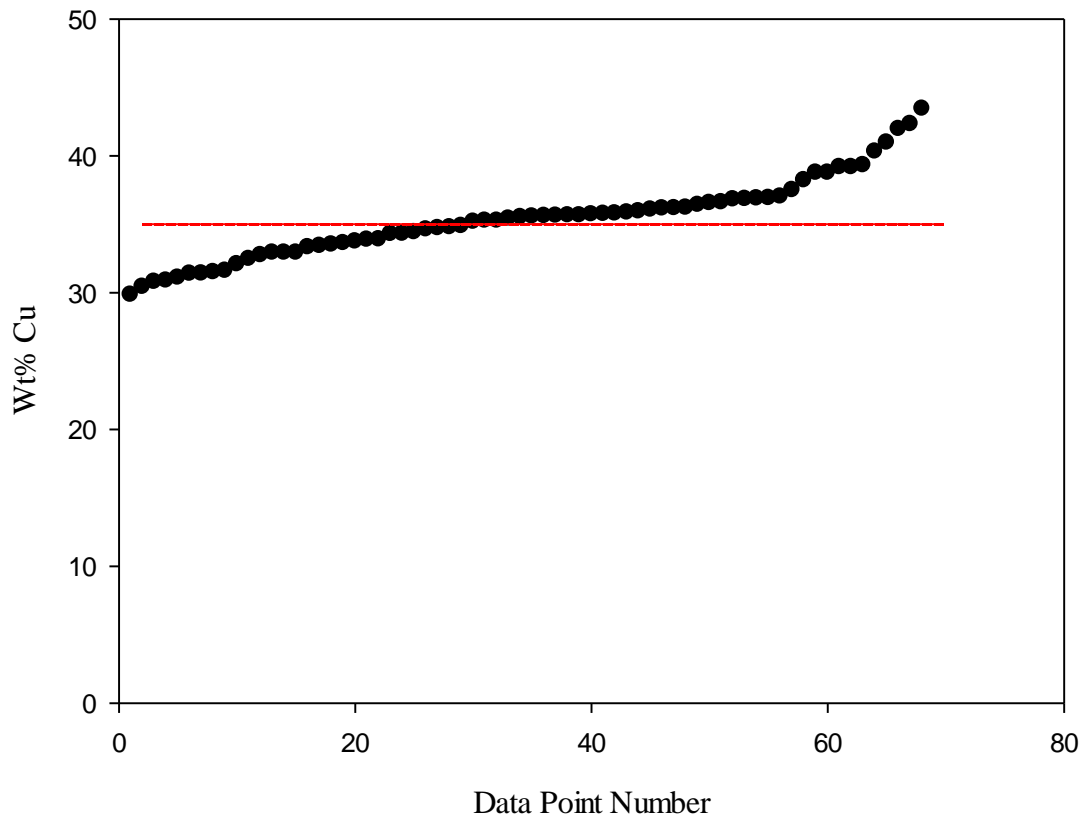
Figure 41. Quantitative EDS analysis of the arc melted rapidly cooled followed by heat treatment sample. The data has been presented in ascending copper concentration.

The quantitative analysis showed the extent of solute partitioning with the weight percent of copper ranging from 29.85 wt% to 43.45 wt%, a range of 13.60 wt%, with a mean value of 35 wt%, Figure 41.

The copper concentration range shows only subtle differences from the sample that did not receive heat treatment, which indicates that the aging treatment had a limited effect on the solute partitioning (overall distribution of composition at different points is little changed). A possible reason for this is the relatively low temperature (compared with the melting temperatures of the components) at which the heat treatment was performed and that the time of the heat treatment which may have not been sufficient for the atoms to diffuse a long enough distance from their

post solidification positions to result in a change in the EDS measurement. The heat treatment was performed on the same casting as the rapidly cooled sample, so the subtle difference in the copper concentration range may be significant and could indicate that some change in the concentration had occurred.

When Figure 40 is compared with Figure 39, the central region of the plots is of slightly different different shape with the sample which had heat treated showing a more gradual change in composition from measurement to measurement. The heat treated sample had changed to produce final structure containing a region similar to that which would be expected in steady state solidification, also displaying the initial and final transients. In this situation this may in fact suggest that the compositional differences at these extremes may have be exaggerated by the beginnings of the phase separation desired from this alloy.
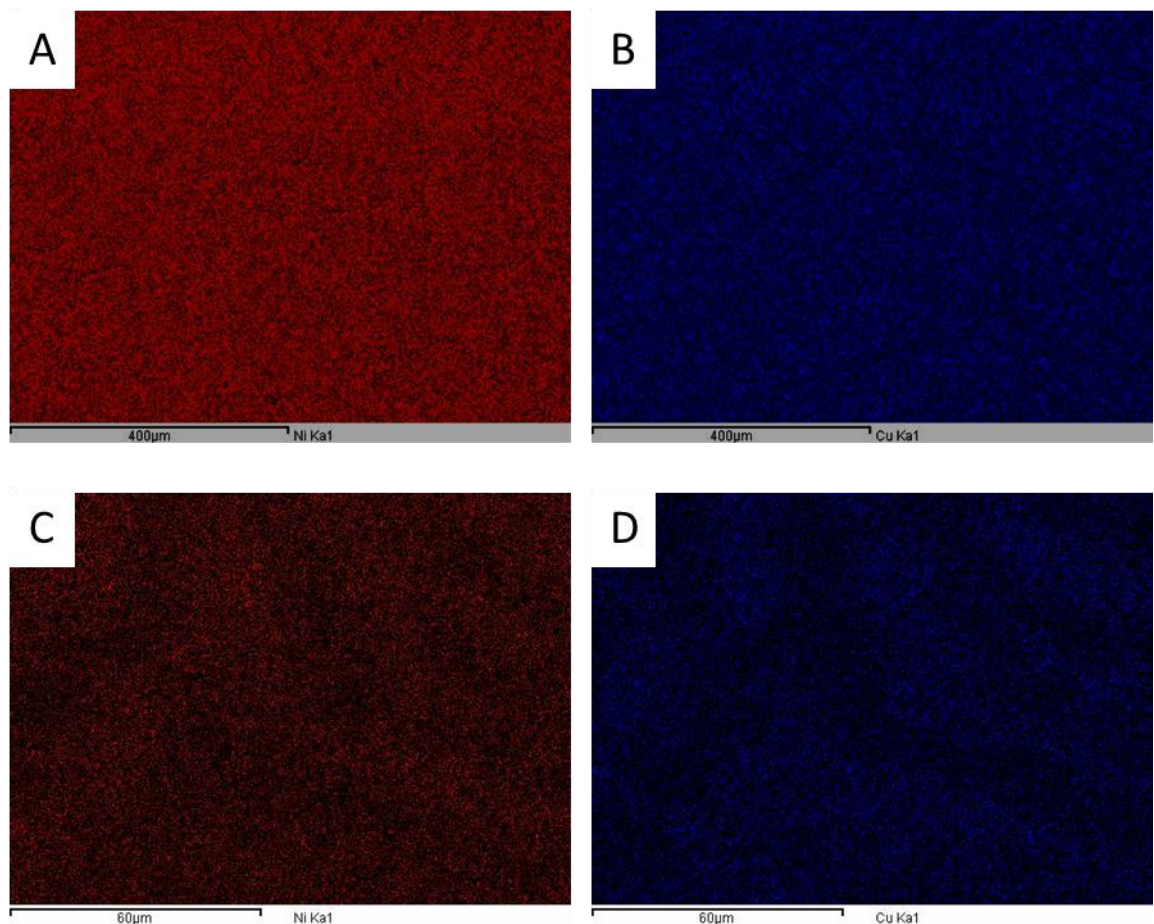
Figure 42. EDS maps of the rapidly cooled and heat treated sample. Shown at low magnification in image (A) and (B) highlighting the nickel (red) and copper (blue) respectively. Shown at higher magnification in image (C) and (D) highlighting, the nickel (red) and copper (blue) content respectively.

The low magnification EDS maps in Figure 42 ((A) and (B)) appears to show a homogenous distribution of copper and nickel in the microstructure, the same as the same sample which had not been heat treated. As before, maps at higher magnification were needed to distinguish the segregation.

The maps taken at increased magnification Figure 42 ((C) and (D)) highlights regions within the scanned area where there was differing concentration caused by solute partitioning; this extent of the concentration change seen was similar to the rapidly cooled sample. When comparing Figure 40 ((C) and (D)) with Figure 42 ((C) and (D)), it appears that the microstructure was different, with Figure 42 ((C) and (D)) having larger regions where the nickel and copper had concentrated, indicated that some diffusion and coarsening of the microstructure had taken place to change the size of these regions.

4.3.3   Slow Cooled Sample

The slow cooled sample showed a significantly different concentration profile to the rapid cooled and rapid cooled and heat treated samples.
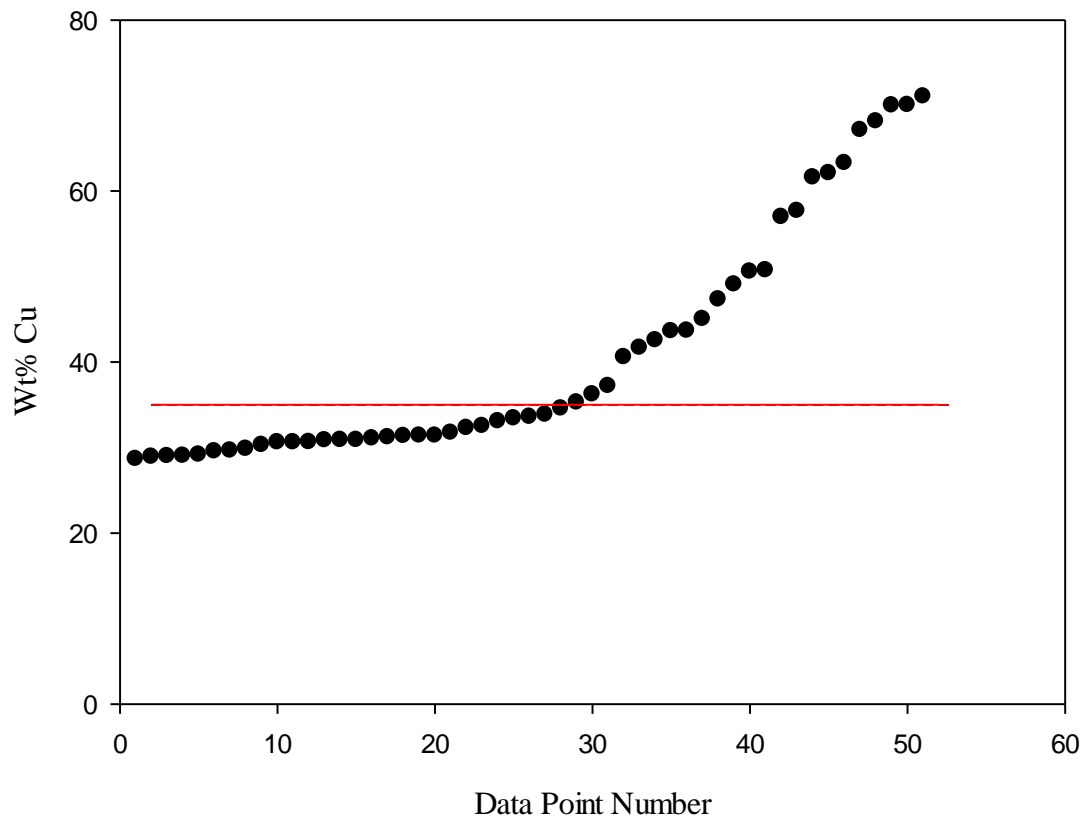
Figure 43. Quantitative EDS analysis of the slow cooled sample. The data has been presented in ascending copper concentration.

The quantitative analysis showed the extent of solute partitioning with the weight percent of copper ranging from 28.66 wt% to 71.06 wt%, and range of 42.4 wt%, Figure 43.

The range of copper concentrations seen is three times larger than that in the two previous cooling regimes showing the extent with which the solidification mechanism has changed. A much greater extent of solute partitioning has occurred with the copper being rejected ahead of the solidification front in concentration greater than in the other cooling rates due to the increased time available for partitioning. It is evident that the conditions of the slow cool have allowed greater partitioning than that was achieved by the heat treating, due to the increased time spent at temperatures approaching (or at) the melting point of the alloy.
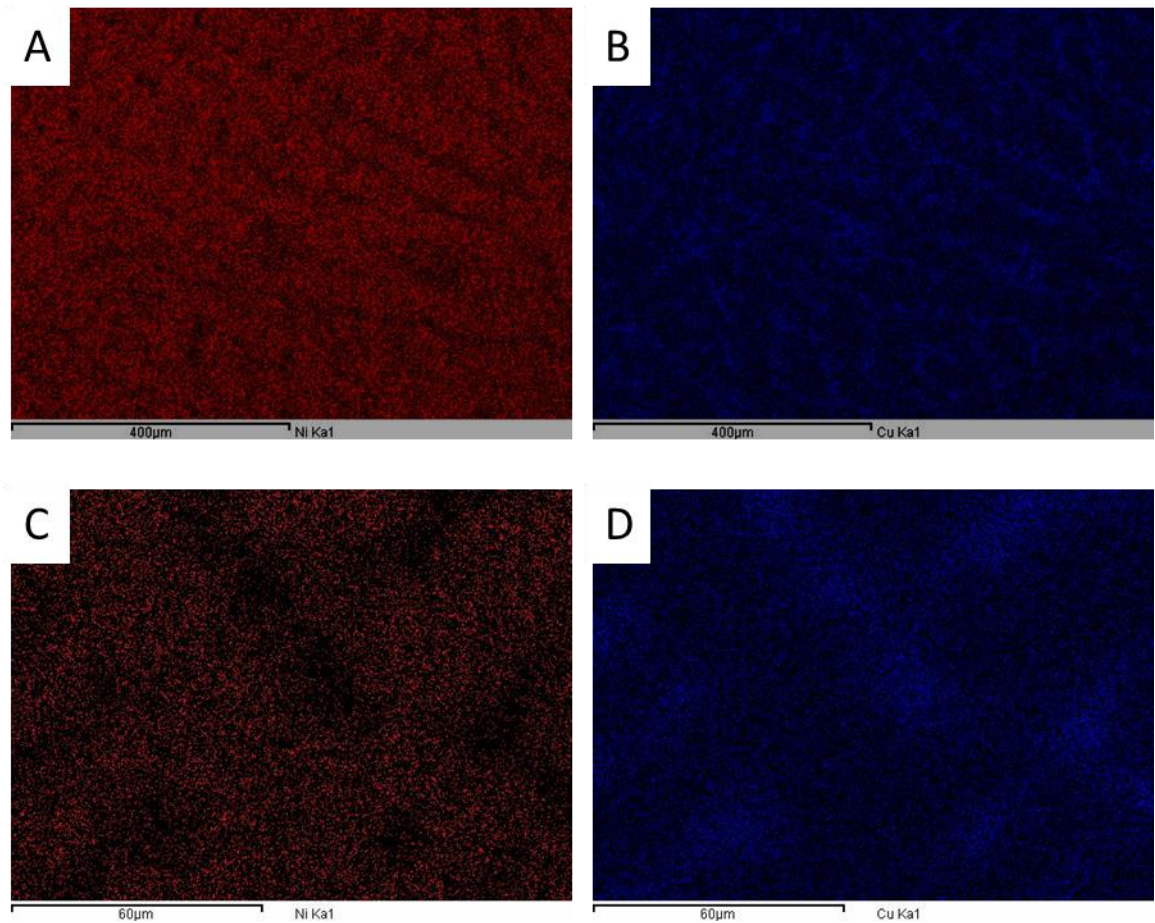
Figure 44. EDS maps of the slow cooled sample. Shown at low magnification in image (A) and (B) highlighting the nickel (red) and copper (blue) respectively. Shown at higher magnification in image (C) and (D) highlighting, the nickel (red) and content respectively.

Segregation under slow cooling rate is also at a coarser scale and shows visible features even at low magnification, Figure 44 ((A) and (B)), in contrast to the other samples; this was an indication of the greater extent of solute partitioning in this sample.

Increasing the magnification, Figure 44 ((C) and (D)) allows for the underlying microstructure of the alloy to become discernible from the homogenous mixture seen in the other samples. The distinct nickel rich and copper rich regions are clearly visible, which would be the preferred structure for chemical etching to produce a porous material. This confirmed the results from the quantitative EDS that there is a greater difference between the low and high concentration values measured. The extent of the partitioning is indicated by the clear regions which do not contain the element being identified (black pixels), indicating the absence of the element.

4.3.4 Comparison between EDS results for the three cooling regimes

When all three solute profiles are compared the difference between them becomes very apparent, Figure 45, the two samples which experienced a rapid cooling showing subtle difference, particularly at the extreme compositions observed, caused by the heat treatment applied.
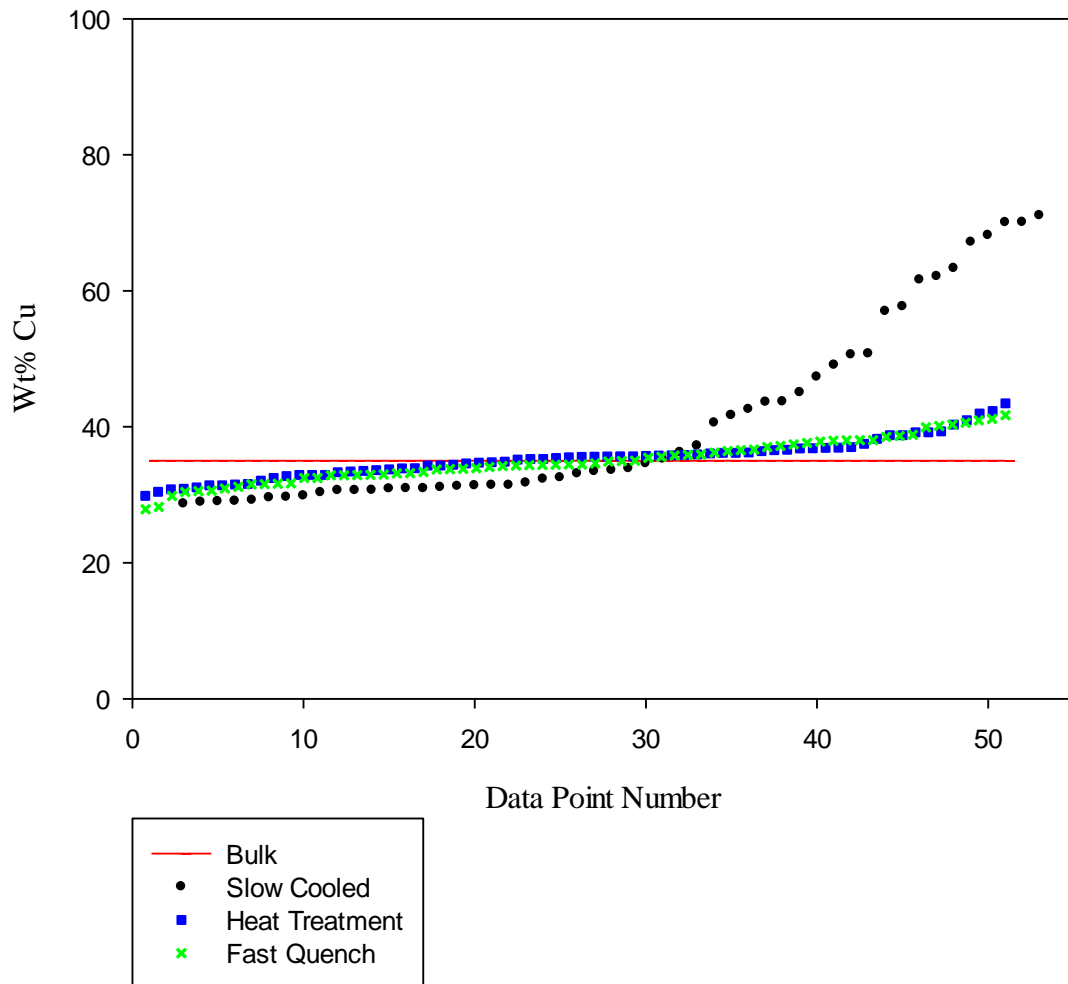
Figure 45. A graph showing solute profiles at three difference cooling rates, which clearly shows the difference in the solute partitioning during slow cooling

When the shape of the profile was compared the rapidly cooled and rapidly cooled and heat treated samples do not have a similar shape to that of the Scheil equation, Figure 21. No initial or final transient was present, only a form closer to steady state with a compositional range of ~13 wt % in both samples, Table 10.

Table 10. Comparison of the minimum and maximum copper measured.

Sample ID	Minimum Cu wt%	Maximum Cu wt%	Range
Rapidly cooled	27.86	42.71	13.85
Rapidly cooled and heat treated	29.85	43.45	13.60
Slow cooled	28.66	71.06	42.4

The slow cooled sample has a much greater range 42.4 wt%, and shows a final transient region of increasing copper concentration. The difference in shape of the profile shows that the solidification mechanism along with the scale is different, between the rapidly cooled and slow cooled samples. The rapidly cooled samples there is little time for diffusion in the liquid, whereas there is time for that to occur in the slow cooled sample hence its better approximation to the Scheil plot shape.
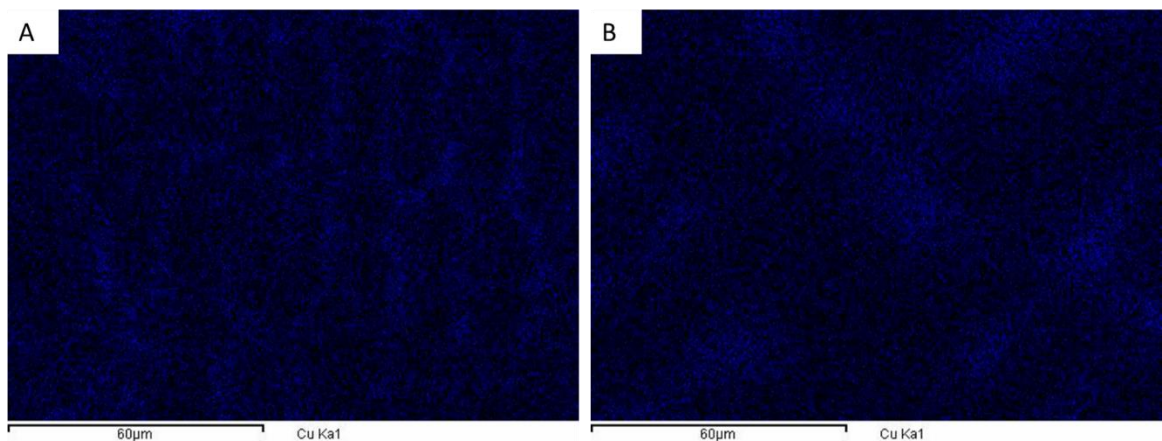
Figure 46. EDS of maps of (A) rapidly cooled sample and (B) slow cooled sample.

This difference, Figure 46, results in smaller regions of high copper content closer together (~20 µm) in the rapidly cooled samples as the copper does not segregate as much and large regions of high copper content further apart (~60 µm) in the slow cooled samples as the copper had time to segregate during solidification. These regions are the cause of the size and distribution of the pores, shown in section 4.4.3.

4.3.4.1 Hardness Mapping

Hardness mapping was conducted only on one polished slow cooled sample as it showed the greatest concentration variations so any trends in hardness were expected to be the most visible. The sample was tested in two locations in order to assess whether the regions of high and low nickel would present themselves as areas of varying hardness, the hardness data were gathered and are presented as an area contour map in Figure 47.
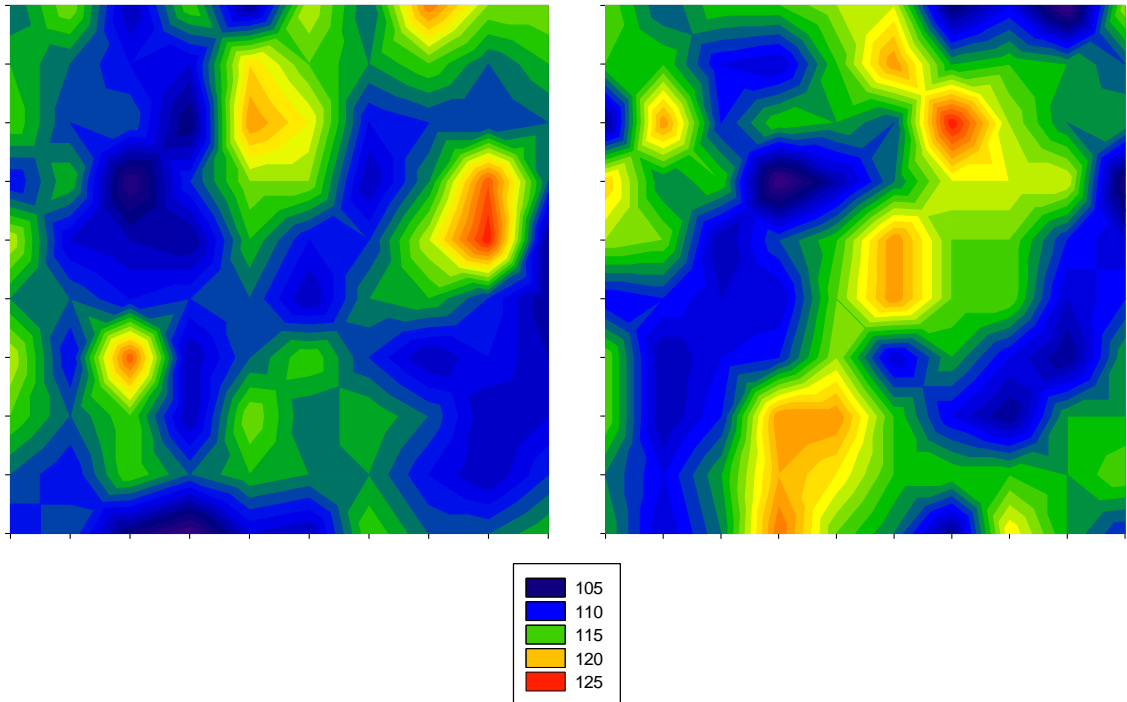
Figure 47. Colour contour map of hardness mapping location 1 and 2. Each map is 600 x 600 µm. Red indicating a high hardness and blue a low hardness.

Although the hardness maps show a variation in hardness with location ranging from a maximum of 125 HV down to 105 HV with a mean value of 114 HV, Figure 47, no obvious structures of scale similar to those observed in Figure 37 are seem. Each point on the hardness map is 60 µm from the surrounding points, the lowest spacing that could be achieved without the indents interfering with each other using this equipment; the result is a resolution that is too low to accurately detect regions of differing hardness on the scale of the microstructure seen in Figure 48.
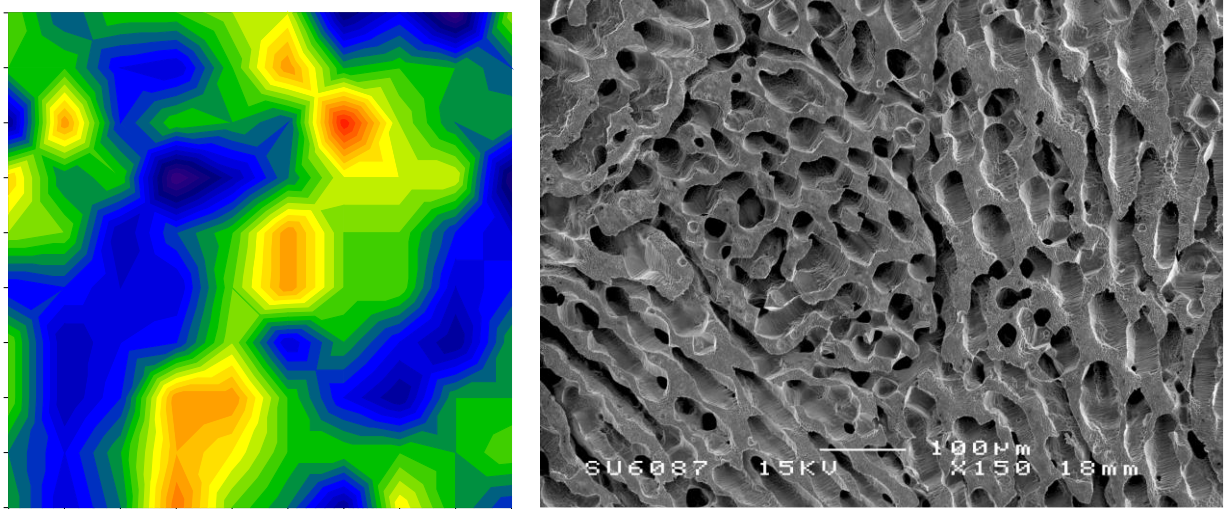
Figure 48. A comparison of hardness mapping and microstructure with both images shown at the same magnification.

The nickel rich areas which were left after the sample had been etched, discussed later and shown for comparison in Figure 48, had a much finer structure than areas of different hardness measured in the mapping, further confirming that the hardness is being influenced by variations on a larger scale than just the segregation of copper and nickel by the slow cooling. This may included local variations beyond composition, such as crystallographic orientation of grains.

4.4   Selective Phase Removal

In order for a porous structure to be created from the segregated nickel-copper alloy samples produced, each sample was etched using the method described in section 3.5. This would remove the copper rich phase of the microstructure preferentially, leaving behind a nickel-rich porous structure. The material removal rate was first assessed in a short experiment conducted on pure nickel and pure copper test samples, consisting of cubes of around a centimeter cut from pure metal bar stock. Each of these was weighed and then placed separately in 50 ml of ferric chloride, the chemical agent selected to have the best discrimination in removal of the copper rich phase while leaving the nickel rich phase unaffected. Each sample was removed from the ferric chloride, washed with distilled water and weighed at 5 minute intervals up to 30 minutes, at 10 minute intervals up to 90 minutes then at 30 minute intervals up to 180 minutes. The mass loss was normalised per unit area and plotted in Figure 49.
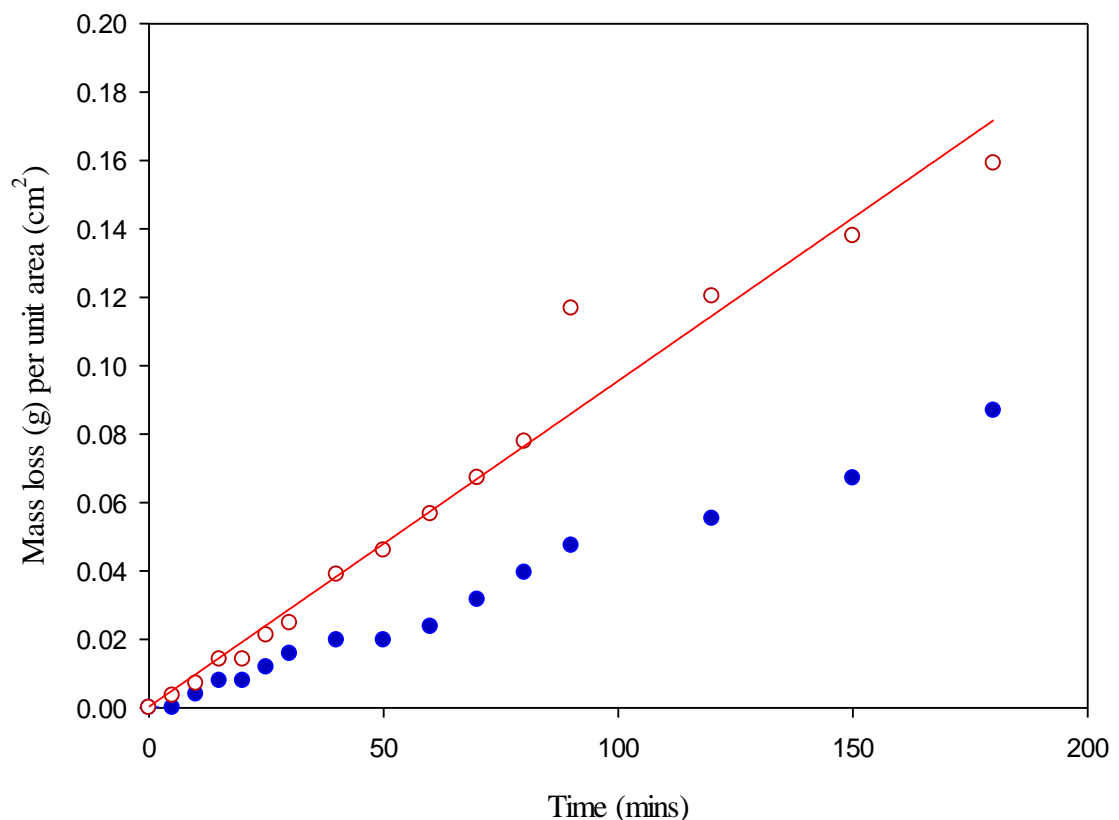
Figure 49. A graph of the mass loss of Ni (blue data) Cu (red data) in ferric chloride, normalised for surface area of the tested samples.

Within experimental scatter the data points are fitted with least squares regression lines of best fit, indicating that the rate of material removal for each is roughly constant throughout the

duration of the test. From the slope of these lines the rate at which the process proceeds may be determined.

Nickel dissolution rate

$$0.0005 \ g.cm^{-2}.min^{-1} \tag{20}$$

Copper dissolution rate

$$0.0001 \ g.cm^{-2}.min^{-1} \tag{21}$$

The results from this experiment confirmed that the ferric chloride does act significantly faster on copper (approximately five times the rate) than nickel, which will permit it to preferentially remove copper. However, the nickel does undergo a measurable rate of degradation as well. A point will come in the process when nickel regions exposed for long time periods to the ferric chloride will have been removed, however the difference in removal rate will allow for segregated copper rich regions to always be removed preferentially and for the structure to present a porous network. The removal of the nickel rich regions will act to reduce the overall mass of the sample, and the depth and extent of the porosity resulting from the copper removal will be proportional.

4.4.1 Level of Porosity Obtained through Selective Phase Removal

The porosity was assessed by preforming point counting on 2 images taken from each sample as described in section 3.9, point counting was conducted on each of the images in two perpendicular directions, in order to evaluate any directionality produced the data shown in Table 11 and Figure 50.

Table 11. The mean relative porosity, standard deviation, standard error and 95 % confidence limits taken for direction 1 and 2

Sample ID	Mean relative porosity direction 1	Mean relative porosity direction 2	Standard deviation direction 1	Standard deviation direction 2	Standard error direction 1	Standard error direction 2	95% confidence limits direction 1	95% confidence limits direction 2
Slow cooled 1	0.55	0.45	0.12	0.051	0.028	0.019	0.058	0.048
Slow cooled 2	0.57	0.49	0.14	0.091	0.032	0.025	0.069	0.055
Rapidly cooled 1	0.50	0.54	0.14	0.058	0.036	0.017	0.076	0.037
Rapidly cooled 2	0.57	0.68	0.081	0.073	0.034	0.030	0.086	0.077
Rapidly cooled and heat treated 1	0.55	0.48	0.12	0.086	0.024	0.020	0.050	0.043
Rapidly cooled and heat treated 2	0.60	0.70	0.11	0.10	0.024	0.023	0.049	0.050

The general trends observed were (i) that direction 1 had a greater standard deviation than direction 2 for all samples. (ii) that direction 1 also has a greater standard error across all samples. These results indicated that the porosity across the sample in direction 1 showed a greater degree of variability compared with direction 2. The standard error for each direction showed that there was less spread in the data in direction 2 compared with direction 1 as in each the sample direction 2 had a lower standard error.
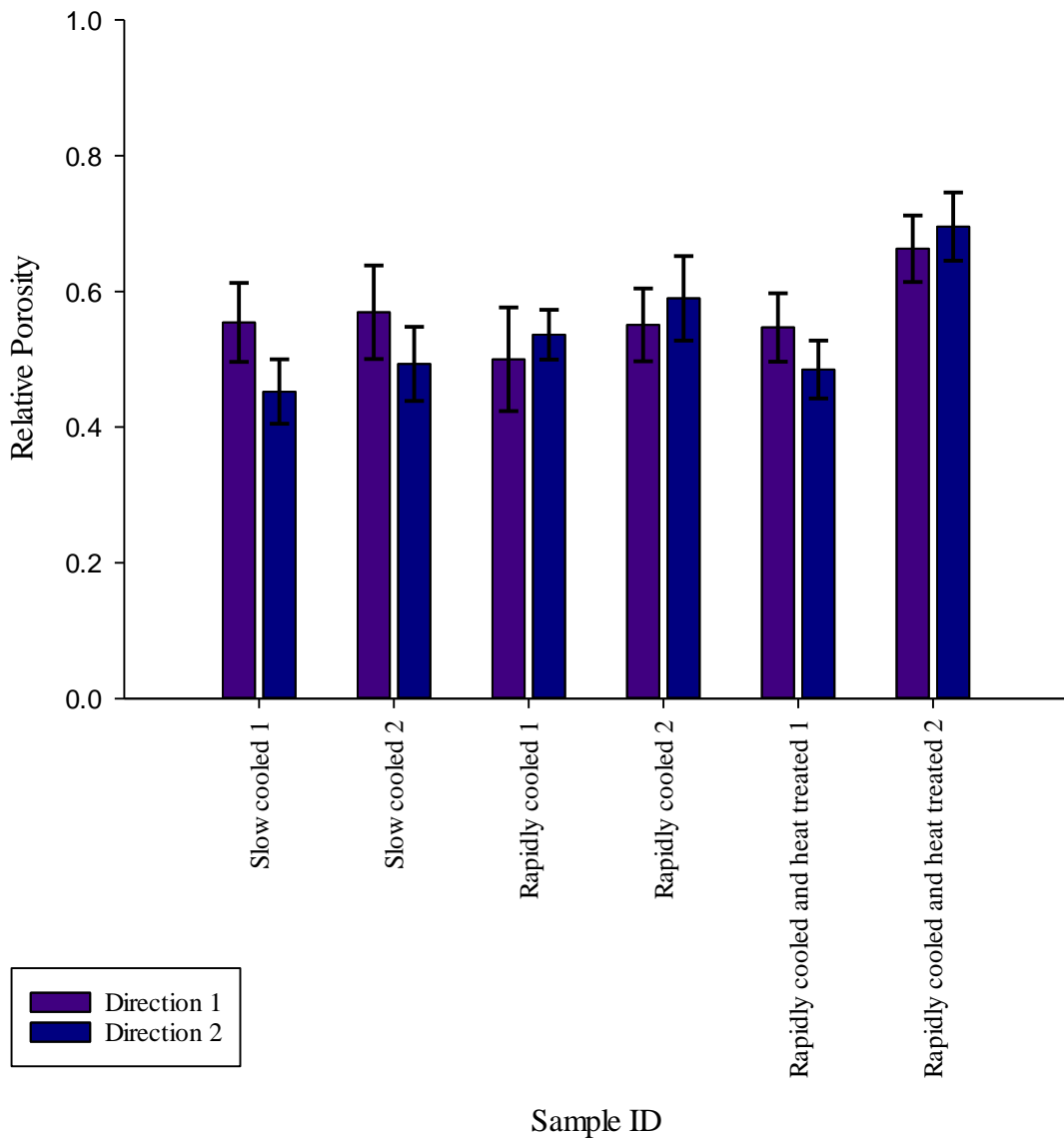
Figure 50. A graph showing the mean relative porosity from two perpendicular directions in each sample, with upper and lower error bars displaying 95 % confidence limits.

When the values for the mean relative porosity of each sample are plotted Figure 50, it becomes clear that there is a small degree of directionality present in the sample measurement however this is a very limited data set. This is further emphasized when the 95% confidence limit is taken into consideration as it shows both sets of data lie within the 95% confidence limits of each other.

The results from each direction were combined so that a mean relative porosity for each sample type (processing route) could be compared. The results are shown in Table 12 and Figure 51.

Table 12. A table of the mean values combining both sample and directions.

Sample ID	Mean relative porosity*
Slow cooled	0.52
Rapidly cooled	0.57
Rapidly cooled and heat treated	0.60

* The mean value for relative porosity was calculated by combining the two data sets and the two directions.

The slow cooled sample presented the lowest value of porosity compared to rapidly cooled samples. Care must be taken in evaluating these values as they were taken from a single plane of the sample and may not be wholly representative of the sample as they do not take into consideration depth. The results show a slight increase in the porosity in the rapidly cooled sample with a subsequent heat treatment, and indicate that the heat treatment had increased the porosity of the sample only by a small amount. It is unclear if this is due to measurement error. The results from the change in concentration with distance measurement in section 4.3 would suggest that this difference was present and has produced high copper concentrations which have then been removed and lead to a higher relative porosity and not due to measurement error.
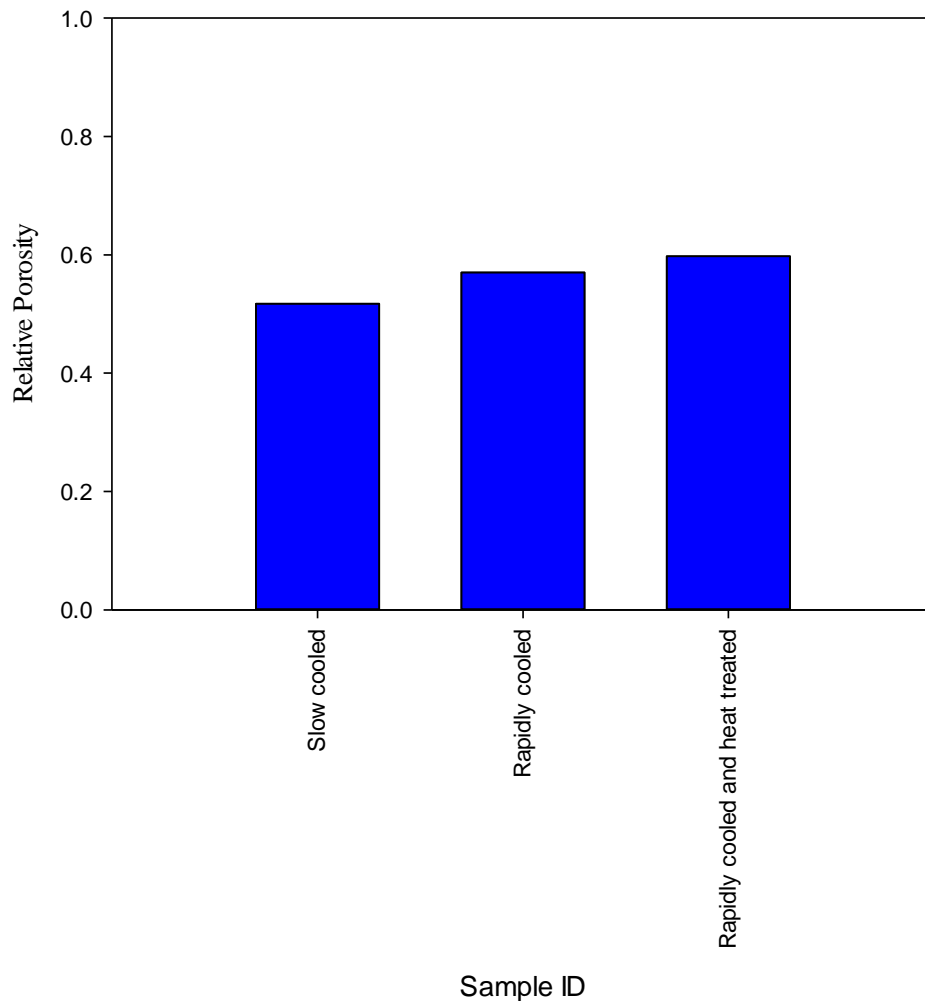
Figure 51. A graph of measured mean relative porosity values.

The difference between all three samples is 8 % a small but significant value that shows that the porosity can be changed by the solidification conditions experienced by the nickel-copper alloy, and crucially heat treating the alloy has a measurable effect and offers a route for changing and controlling the base level of porosity in post processing after solidification has taken place. The levels of porosity present in all three sample also indicate the effect of the base composition of the binary alloy on the final porosity. As all three samples have the same bulk composition it was the partitioning of the solute during the different solidification paths that caused the difference in porosity. It must however be recognised that possible sources of error in the measurement are present which could have a significant effect on the results obtained. As each sample was processed individually for the removal of the copper rich phase each will have slightly different processing conditions. Another likely source of error is in the measurement of the pores themselves as this was done manually (for reasons covered earlier) human error will play a part, but it is likely to be less than the error of a software based measurement as a human can more easily distinguish a pore boundary in a less than perfect image.

4.4.2 Characteristics of the Porous Structure Formed

These investigations were carried out on samples that had been subjected to a significant degree of etching as described earlier, to develop a porous structure.   In all cases, as seen in the following SEM images, porosity has developed corresponding to the copper rich regions in the microstructure. The samples are assessed beginning with the rapidly cooled, then rapidly cooled and heated and finally the slow cooled, to compare the pore structures formed. The same flat polished samples used for EDS mapping were used for SEM imaging to allow for direct correlation between the element partitioning observed from the quantitative scans and the mapping.

Rapidly cooled

In the large field of view images shown previously Figure 37, it can be seen that the columnar region of the ingot apparently displays lower overall porosity compared with the centre dendritic region. The increased cooling rate in this section leads to faster solidification front, reduced time for diffusion in the liquid and trapping the solute and therefore less solute partitioning of the copper to the intercolumnar spacing.
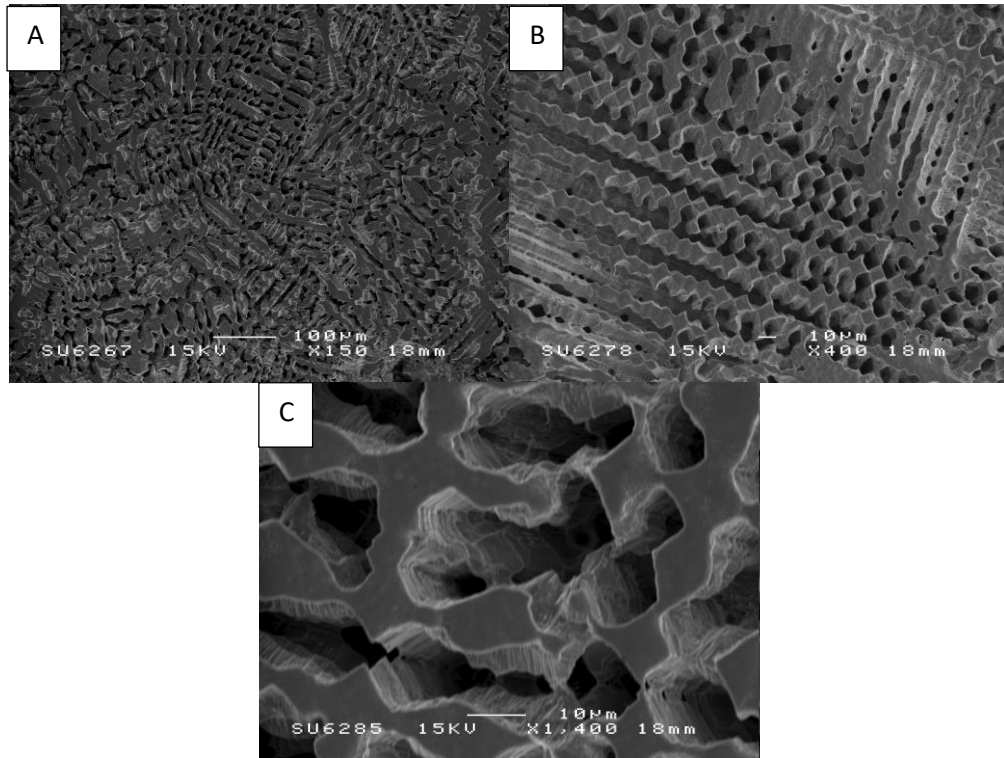
Figure 52. SEM images taken of the central region of the rapidly cooled sample, (A) Showing a porous structure due to the large area of dendritic growth. (B) Showing the high level of periodicitiy of the porosity. (C) displaying the flat surface of the remaining nickel rich region, apparently unaffected by the etching process

The central region, see Figure 52 (A), of the ingot had a dendritic structure as it experienced more uniform, , slower cool rate (in this rapidly cooled sample), allowing more time for solute partitioning and the relative size and copper content of the inter dendritic regions increased. This increase resulted in a larger volume of material being removed by the ferric chloride, hence a higher porosity.

The plane of the image in Figure 52 (B), cuts through dendrite arms. A preferred direction is evident with a periodicity revealing itself. This periodicity once again indicates that the growth of porosity is controlled by the microstructure.

As depicted in Figure 52 (C) within the unremoved nickel rich regions, the original polished surface of the sample is still intact, signifying that the etchant is only acting to a significant extent on the regions to which the copper has partitioned to. In Figure 52 (C), distinct layering can be seen on the structures making up the walls of the pores, these layers have two possible causes, both due to small concentration variations caused during solidification, they are either early stages of lower order dendrite arm formations, if the cooling rate is still relatively slow. The other possible cause is the formation of high solidification front velocity cells that have formed in final stages of cooling.

The depth of the removal is very clear with evidence of more than just removal normal to the surface, with the beginning of a pore network being formed. The extent of the interconnections between pores is limited in this sample, which has been rapidly cooled with the highest number of copper rich regions being removed located in the centre of the ingot where the solidification has occurred via dendritic growth.

An EDS map was taken from an etched sample to highlight the concentration of the constituents remaining after etching.
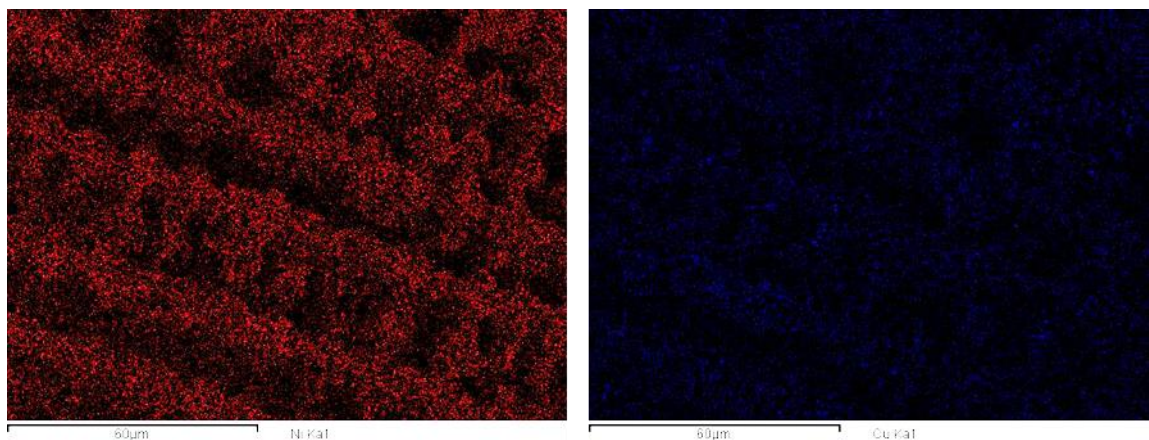
Figure 53. An EDS map illustration the relative levels of copper and nickel remaining post etch.

A mapping was performed (Figure 53) on an etched sample to confirm that the features from the SEM images associated this the nickel rich regions were regions left behind after the ferric chloride treatment, with lower amount of copper contained in these regions. The map clearly shows that the remaining regions has a high nickel content in contrast to the copper content. The scale of the microstructure, the distribution and size of the pores in Figure 53 is the same as that seen in Figure 52.

Rapidly cooled and heat treated

The sample which had undergone heat treatment was investigated to compare the effect of the heat treatment on the pore structure and characteristics that had formed, beyond just the increase in relative porosity (57% to 60%) measured.
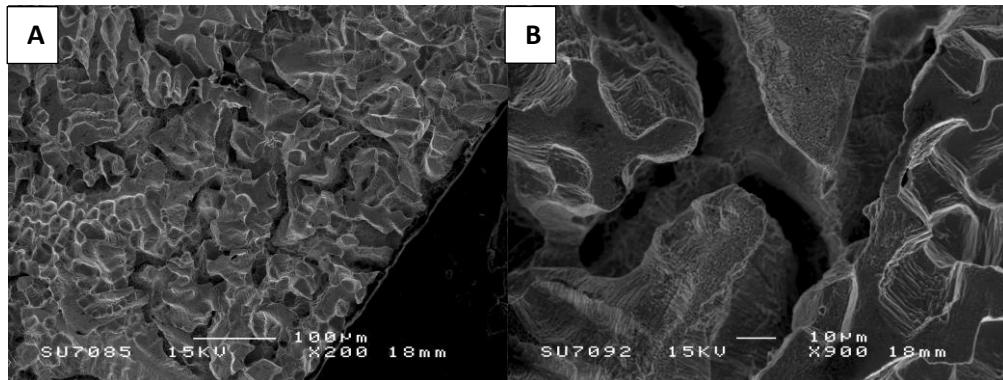
Figure 54. SEM images of the rapidly cooled and heat treated sample (A) A low magnification of the edge region. (B) A higher magnification image of the center showing the depth and complexity of the pore network.

The three dimensional structure and depth of the pore network is discernible in the edge region of the sample in, Figure 54 (A), the more random nature of the solidification microstructure in this region and lack of periodicity results in a more intricate network of pores and channels that have been left visible after the removal of the copper rich inter dendritic spacing. The heat treatment time has been insufficient to cause an observable amount of copper segregation to the grain boundaries during the heat treatment as the grain boundaries are only observable due to the change in dendrite direction. The depth of the etch becomes evident at higher magnifications see, Figure 54 (B). The layering along the inside of the pores seen in the rapidly cooled only sample is still present after heat treatment. The flat plateaus of material on the nickel rich regions show some limited evidence of pitting, this is likely due very localised removal of the copper at the surface. Figure 54 (B) is a good example to illustrate that the removal of the copper rich phase was not just occurring perpendicular to the surface but caused under cutting and the formation of an interconnected pore network, with the bottoms of the pores not visible.

Slow cooled

The slow cooled sample showed the strongest degree of segregation, and the porous structure that developed after the etching treatment was very clear see Figure 55 (A) and (B).
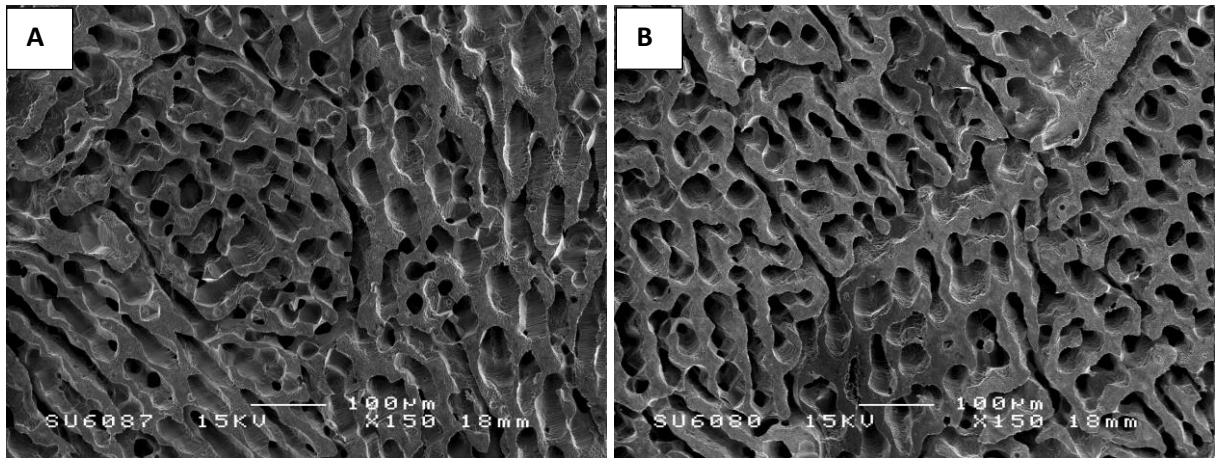
Figure 55. SEM images of the slow cooled sample after etching, in which the underlying the grain structure can be seen.

The underlying grain structure was evident after the removal of the copper rich phase. The original grain boundaries presented themselves as long, thin continuous pores, which indicates that the copper was also partitioning strongly to the grain boundaries. The enhanced grain boundary solute partitioning was only strongly present in the sample which was slowly cooled from the liquid state. The grain boundaries were also identified by the orientation of the pores inside each grain see Figure 55 (B). Each grain was formed from a dendrite growing with a specific orientation, there adjacent grains had a different orientation as dendrites formed. The effect of this growth is present in the pore orientation within the grains. The pores within each grain form in very distinct patterns allowing for each grain to be identified even when the grain boundaries are unclear. The higher degree of partitioning driven by the slow cooling gave rise to a structure which possessed a greater level (or at least more easily visible level) of three-dimensional interconnectivity, Figure 55 which is key requirement for the development of through thickness porosity.
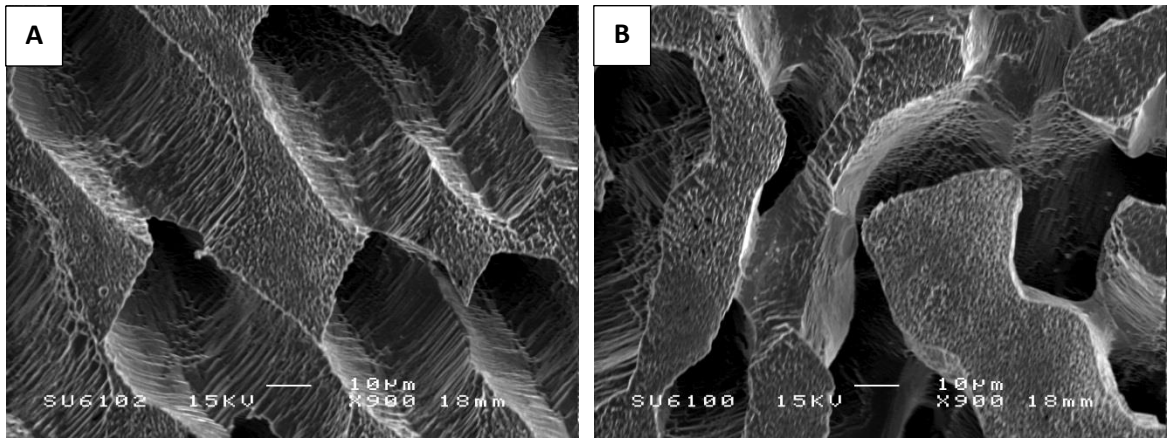
Figure 56. SEM images of pore structure at high magnification, (A) showing pores penetrating into the bulk of the sample. (B) showing parallel pores.

On closer inspection, it could be seen that areas of the sample exhibited pores perpendicular to the surface. This feature was likely to be due to the orientation of the dendrite arms. Grains with other orientations lead to other pore orientations presenting themselves at angles to the prepared surface, see Figure 56 A and B. The layering seen in all previous samples also present, Figure 56 (A), this shows that similar solidification features are present in all samples.

The surface of the sample which remains shows limited signs of attack by the ferric chloride similar to those seen in the rapidly cooled and heat treated sample, see Figure 54 (B). This pitting also likely to be removal of the smaller localised copper concentrations.

4.4.3   Pore Size

The pore sizes were measured using the same images used for point counting. When a pore intersected the vertical grid lines it was measured between those points. This method was used to remove subjective bias in the measurement, but also as the porosity had become joined up into a network this method would allow for the size of the pore network channels to be measured, the results are shown in Table 13.

Table 13. The mean pore size of each of the solidification routes

Sample ID	Mean pore size (µm)	Standard Deviation
Slow cooled	66	45
Rapidly cooled	17	7.7
Rapidly cooled and heat treated	30	24

The mean pore size for the slow cooled sample was twice the size of the rapidly cooled and heat treated sample and four times that of the rapidly cooled sample. This result means that the network of pores in the slow cooled sample was larger as all the samples had similar relatively porosities to each other. The slow cooled sample was expected to have the largest pores owing to the solute partitioning and phase separation during solidification. That resulted in larger copper rich regions that were subsequently removed. The heat treatment of the rapidly cooled sample also had a dramatic effect on the pore size, nearly doubling it. This was good evidence of the effect the heat treatment had on solute partitioning post solidification.

The size of the pores produced using the single etching method described allowed for a comparison between the solidification methods, it is likely that with longer etching time the size of the pores will change. However, the change would have increased depth of the pores, as the near surface region porosity (which has been measured on these samples) is likely to be close to the maximum size as the copper rich phase has already be removed. The pore depth had two limiting factors, the first limit is access for the etchant, thin narrow channels will reduce its effective range. The second is any inhomogeneity present in the alloy will result in regions where the copper it trapped within nickel rich regions and is unable to react with the ferric chloride.

It was also possible to measure the periodicity that is seen in Figure 52, 53 and 55, and compare this across the difficult solidification regimes, Table 14.

Table 14. Mean periodicity of porous structure

Sample ID	Mean Spacing (μm)
Slow cooled	50
Rapidly cooled	17
Rapidly cooled and heat treated	17

The size of the spacing of the periodicity seen in the microstructure follows the same trend seen in the measurements of pore size, with the rapidly cooled having the smallest spacing between the etch repeating structure and the slow cooled having the largest. The rapidly cooled and rapidly cooled and heat treated sample have the same spacing as structures that are being measured and compared are the core of dendrites, coarsening of this is unlikely to have occurred during the heat treatment. The heat treatment has acted most strongly on the composition of the interdendritic region where compositional changes via diffusion are easier due to the distances required for a change to be effective.

4.4.4   Investigations of the structure of the generated porosity from a non-planar surface

To fully assess etching and the dimensions of porous material that have been generated, it is necessary to determine how deep within the material the porous network penetrates, and how constant the structure is over this range. To do this, the slow cooled alloy, which shows the greatest effect, was been examined in a number of different configurations. Two further samples of the slow cooled alloy were prepared. These samples had several polished surfaces at different angles, rather than being a flat planar sample.

4.4.4.1 Wedge Shaped Geometry Porous Sample

A thin wedge of material (with an angle of approximately 30°) was prepared by grinding and polishing a solid sample by hand, which was then etched as before, producing a porous structure in which the pores were continuous through the thickness, Figure 57.
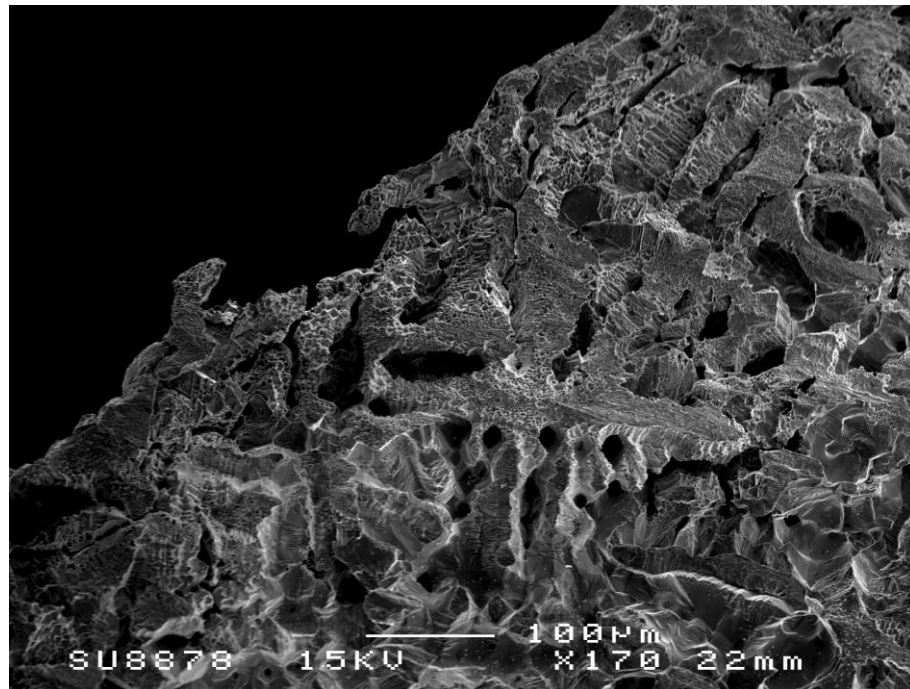
Figure 57. SEM image taken from the edge of the wedge-shaped sample.

The wedge-shaped sample Figure 57, showed all the features that were present in the sample viewed perpendicularly. The dendrite arms were present and at the extreme edge of the sample all the copper rich phase had been removed leaving these arms extending out into free space. It was hoped that observation of how far along the wedge the sample could be seen through would allow the depth of etch to be calculated, knowing the wedge angle. However, as seen in the image above the pore structure of the material generated in this case did not allow viewing through the structure. It was possible to approximate the distance from the edge of the sample that would contain through thickness porosity using simple trigonometry, and assuming that viewing perpendicularly produces a right angle. If the nominal pore size is 66 µm (taken from section 4.4.3) and the angle of the wedge is 30°, then the maximum distance that could be view through thickness (along a single pore) would be 114 µm. This is the distance for a single pore. However, due to the dendritic nature of the porosity, it was feasible for the orientation of a section to be tailored such that the copper rich interdendritic region runs perpendicular to the section surfaces. This method would allow for very large sections to contain through thickness porosity. It was also possible to produce a section where the copper rich regions run parallel to the surface.

4.4.4.2 Pyramid Shaped Geometry Porous Sample

A piece of the slowly cooled sample was also ground and polished by hand into a three sided pyramid, this allowed the apex and the edges (Figure 58) to be viewed to give a more in depth details of the three dimensional structure of the porous structure formed. The sample was etched by placing in the ferric chloride solution such that it was three quarters submerged. It was etched for 5 minutes before being removed and washed with water. A selection of images were taken to characterise the structure.
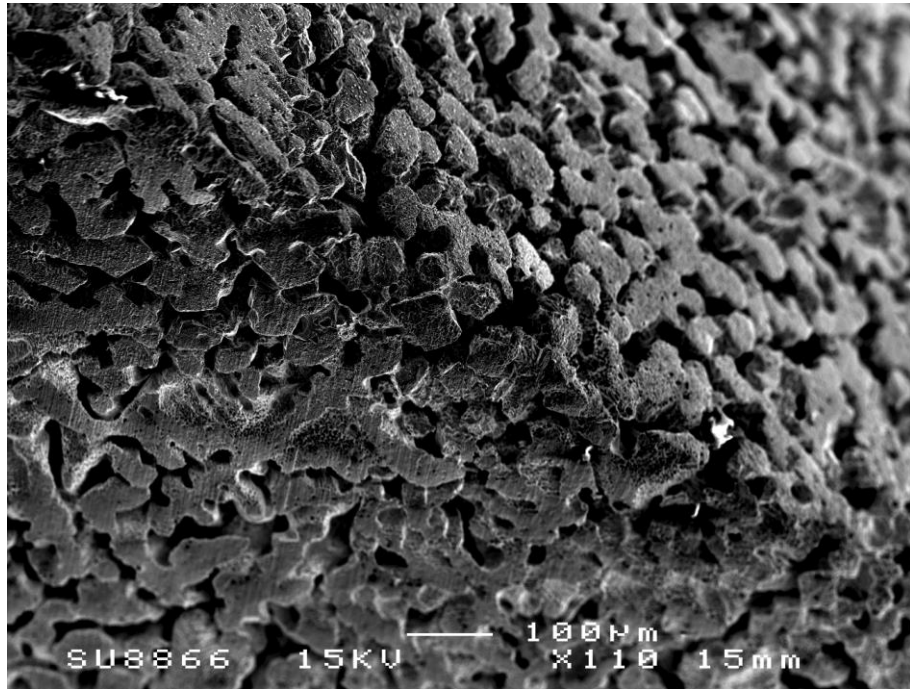
Figure 58. An SEM image of an edge the of the pyramid sample.

Viewing the pyramid shaped sample along one edge, as in Figure 58, allowed for the full three dimensional structure of the pores to be appreciated. The pores were present on both faces of the edge and some continuity of the pore network from one face to the other has been seen. Significantly, scratches are still present from where the sample was ground to shape, confirming that the ferric chloride as acted preferentially on the regions which contain a high level of copper. If this had not been the case the flat surface of the faces of the pyramid would show sides of material removal and the scratches would no longer be evident.
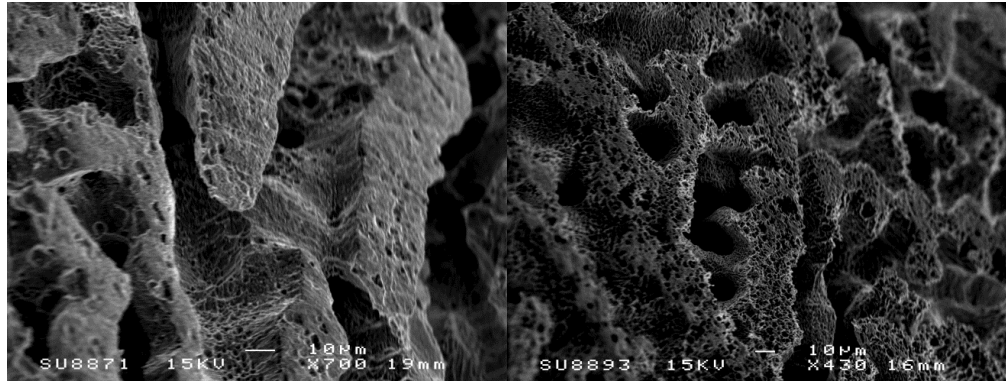
Figure 59. SEM images highlighting (A) the enhanced under cutting of the etchant which led to the porous structure and (B) The removal of copper at a finer scale, on the surface of the remaining strut network.

The angled nature of this sample allowed a greater level of examination of the pores, and Figure 59 (A), shows the under cutting that had occurred within the sample to give rise to a three dimensional porous structure. It is clear from Figure 59, that the pores were not just pits normal to the surface, but also extended laterally in a network. Dendrite arms can be seen to extend freely into empty space, created by the removal of material from underneath them.

In some regions of the sample the flat ground surface of the faces of the pyramid have begun to experience copper removal on a finer scale see Figure 59 (B). This is likely to be the result of the longer time that each section was in contact with the etchant, compared the method used to produce the structures in sections 4.4.1-4.4.3. The longer contact time has caused the ferric chloride to start to act on regions of the sample which had a lower overall copper content and begin to leach the copper from those regions; this is the most probably cause of the texture of the dendrite arms seen in Figure 59 (B).

A pyramid shaped sample of slow cooled alloy was partial submersion in the ferric chloride solution to investigated the process of copper removal a transitional zone formed from bulk material to porous, see Figure 60.
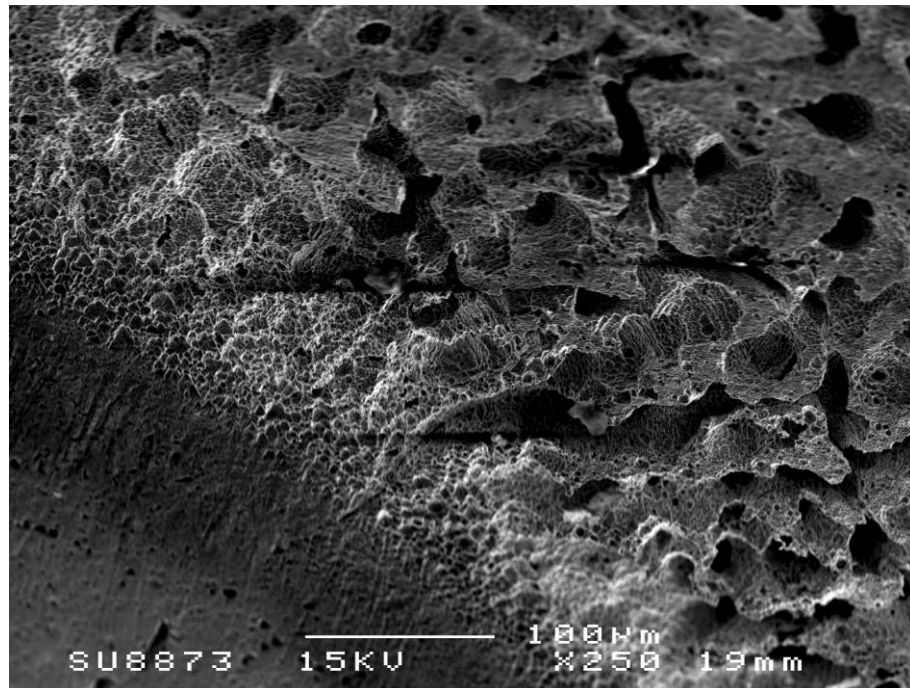
Figure 60. SEM image of transitional zone between the bulk solid and the porous material

In this image the bulk material is clear in the bottom left hand corner and the fully porous structure is visible in the top right corner of the image, with the transitional zone across the center of the image. This zone gives an insight into the removal mechanism. A small proportion of the copper is removed initially, as shown by the change in surface texture. As this copper is removed it will also remove any nickel trapped within it adding to the volume of material that is removed. This "excavation" process continues until only very high nickel-containing alloy is present at the surface and the overall rate of dissolution slows down (likely to become limited by diffusion through the etchant within the pore network as the structure grows deeper). Following this, further copper removal occurs on a fine scale.

4.4.4.3 Surface Porosity Viewed in Cross Section

The depth of the pores network of the slow cooled sample were measured in cross section, this was done optically. The surface of the sample was places as parallel to the bottom edge of each image as the sample would allow (due to the variations in surface shape of each sample) Figure 61. In this measurement, it this total pore network depth that is being assess, for a pore to qualify for a measurement a route to the surface must be visible, and the pore opening at the surface must not be its be the widest part. Only the deepest pores were measured as it was the extent extent the pores penetrate the surface that is of interest see Figure 61. This measurement is subjective open to human error and only used to give a rough insight into whether the pore size measured from the surface is replicated in the depth.
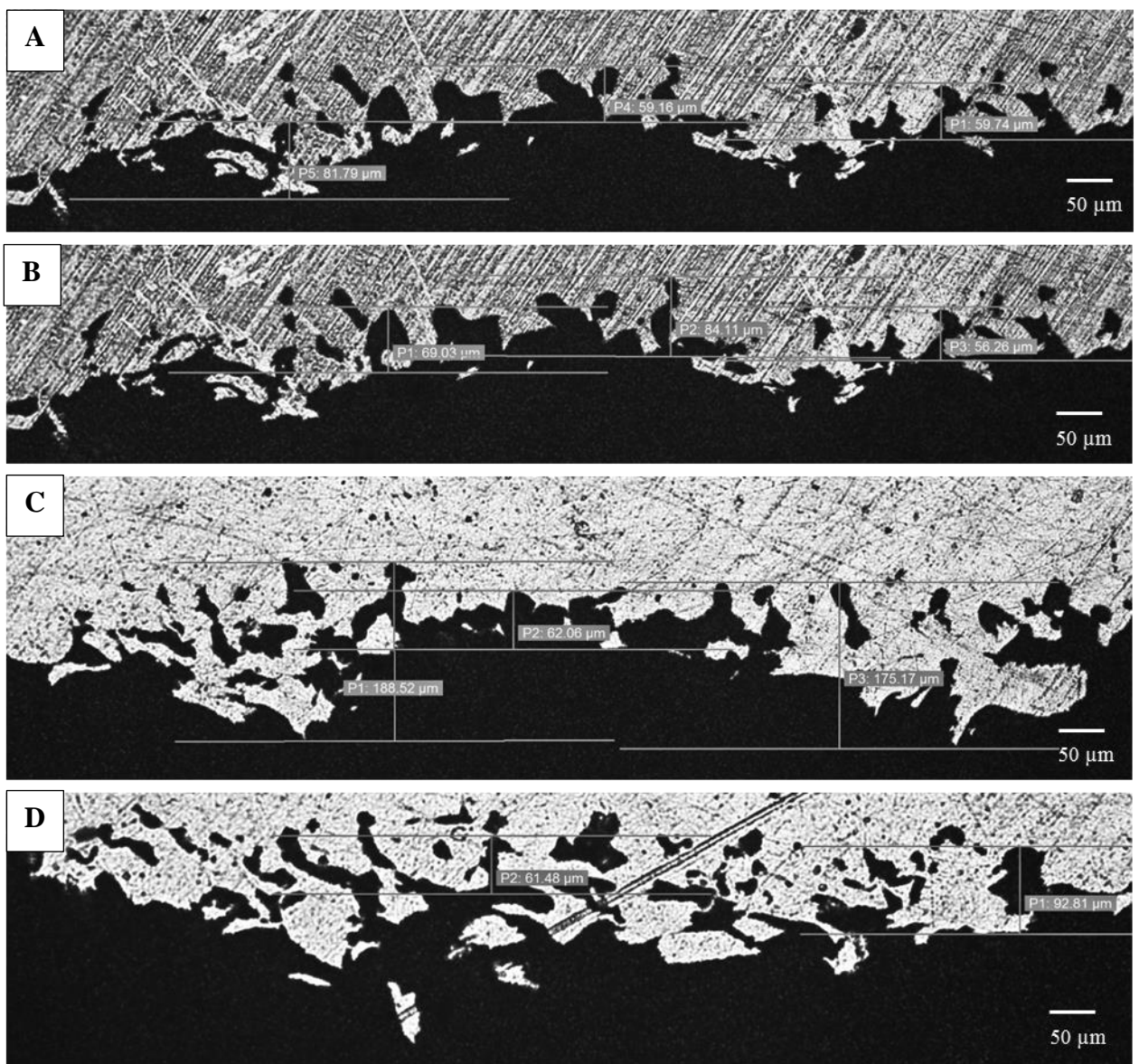
Figure 61. Optical micrographs taken perpendicular to the etched surface.

Table 15. The depth of pores identified in Figure 61

Image	Pore Depth (µm)
A	81.8
A	59.2
A	59.7
B	69.0
B	84.1
B	56.3
C	188.5
C	62.1
C	175.2
D	62.5
D	92.8
Mean	90.1
Standard Deviation	47.0

The results from the cross sectional analysis of pore depth shown in Table 15 indicates pore depth is varied, with some results similar to a single pore (~66 µm) as measured in section 4.4.3, (these pores are still growing) and measurements greater than this illustrate that multiply pores have joined to form a network. However, the large standard deviation 80% confidence limit of ± 20 µm, this results can only be used a rough guide to the pore depth.

4.5   Mechanical properties of the porous structure

A sample with complete through thickness porosity was not produced and so compression testing was not performed as compression testing of the material would only give the strength of the bulk alloy. To assess the strength of the porous structure, hardness testing was used. For materials, such as foams that effectively have zero Poisson's ratio (i.e. they can be compressed without lateral expansion) the results of hardness testing should represent the compressive yield strength, in this case the hardness data is being used as definitive result but as a guide and comparison between the samples.

Vickers hardness testing was performed using a range of weights (1, 2, and 3 kg), to produce indents with different depths, see Table 16. Due to the known fixed geometry of a Vickers indenter, the depth of the indent can be calculated from the diagonal of the indent Table 17.

Table 16. A comparison of the mean Vickers hardness values.

Sample ID	HV1 (1 kg)	HV2 (2 kg)	HV3 (3 kg)	Mean	Standard deviation
Rapidly cooled	99	73	98	90	14
Rapidly cooled and heat treatment	137	119	108	121	15
Slow cooled	149	198	104	150	47

The individual results used to calculate in Table 16 show a large degree of spread, ranging from 50 to 366 HV; this is expected due to porous nature of the sample.

Ideally the indent should cover as large an area as possible so that it is deforming a large number of struts from the porous network. As shown in the previous section the porous structures that have been produced do not extend deep into the material, and as a result the likelihood of the indenter coming into contact with the bulk material and contributing to the result increases. This measured variation will also be due to the position of the indent with respect to the pores themselves. For some indents the tip will enter free space before impacting a lower strut while others will impact a strut directly, this strut will not necessarily be free in space, and it could

extend to the bulk. These complications mean that the hardness values cannot be used in isolation. To aid with interpretation, the indents were observed in the Scanning Electron Microscope which would also allow the deformation to be characterised.

To see if the hardness presented any trends, the mean was calculated both across samples and across HV values, Table 16. The most obvious trend that is present was the increase in hardness from material processed from an alloy that was rapidly cooled to the alloy that was heat treated and slow cooled. This is difficult to explain by reference to the state of the alloy in these different cases, as it would be expected that the finer microstructure caused by fast cooling would in fact be stronger. However, it is well known for foams that the amount of porosity is the most significant parameter in determining the strength.

The slow cooled sample had the lowest relative porosity and largest pore size and the highest hardness, with the largest standard deviation. It is therefore very likely that during the test the indent was not sampling a representative sample size or number of pores but either impacting a strut (which were stronger) or the regions between them and being partly supported by the larger struts. In the rapidly cooled sample the pore size was much smaller but with a similar relatively porosity value, as such the indent is spread across a much larger number of pores and gave a much more representative value of the hardness of the porous region and not the bulk. The rapidly cooled and heat treatment samples results sit between these two extreme, as pore size and the hardness measured were also between these two extremes. This provides evidence of the influence of pore size on the hardness. With the larger pore sizes equating to larger structures in the pore network (struts) which offer a higher level of strength while having a similar relative porosity, to samples with small pores and finer structures.

There is also a variation between the hardness values when different weights are used, in many cases the samples showing lower values for HV3 (3 kg load) than for the other loads. At the higher load the bulk properties of the alloy will begin to have an influence. However, as this is dense material, it would be expected that it would increase the hardness found. It may be that all the indents penetrate too deeply into the sample to solely be influenced by the porous material, which would also help to explain the high level of variability that is seen.

The depth of the indents in the porous samples was calculated using the standard Vickers hardness indenter geometry, the mean of the indent diameter and simple trigonometry. The results are shown in Table 17. The depth of the indent does increase with load.

Table 17. The indent depth evaluated from Vickers hardness testing.

Sample ID	Indent Depth (HV1) µm	Indent Depth (HV2) µm	Indent Depth (HV3) µm
Rapidly cooled	28	46	48
Rapidly cooled and heat treatment	24	36	47
Slow cooled	23	28	45

The calculated indent depth for all the loads used was less than that of the pore size measured for the slow cooled sample but not the others, thus if only a single pore layer is present on the surface the bulk material will be contributing to the hardness values. However, the SEM images indicated that the pore network across all the samples ass extensive and three dimensional. Therefore, it is highly likely that the depth of porous material was close to or greater than the indent depth. However as seen from the hardness results the sample with the smallest pore size (rapidly cooled) had the lowest hardness value so the pore network may well extend deeper into the bulk, and minimize bulk alloy contribution to the hardness.

4.5.1 Deformation as a Result of Hardness Testing

The physical deformation was assessed by taking a series of the SEM images of the hardness indents, see Figure 62, images. They have been displayed systematically to allow for direct comparisons off all the testing conditions, (A) samples are rapidly cooled and the number signifies the load 1=1 kg, (B) samples were rapidly cooled and heated and (C) samples were slow cooled, again the number signifying the load used. The magnification of the images increases with the load.

Due to the different porous structures that have been produced the indents encounter different structures, as
As we move through Figure 62(A), (B) and to (C), the size of the pores and struts increases, and with this increase determination of the precise size and location of the indent becomes more difficult.
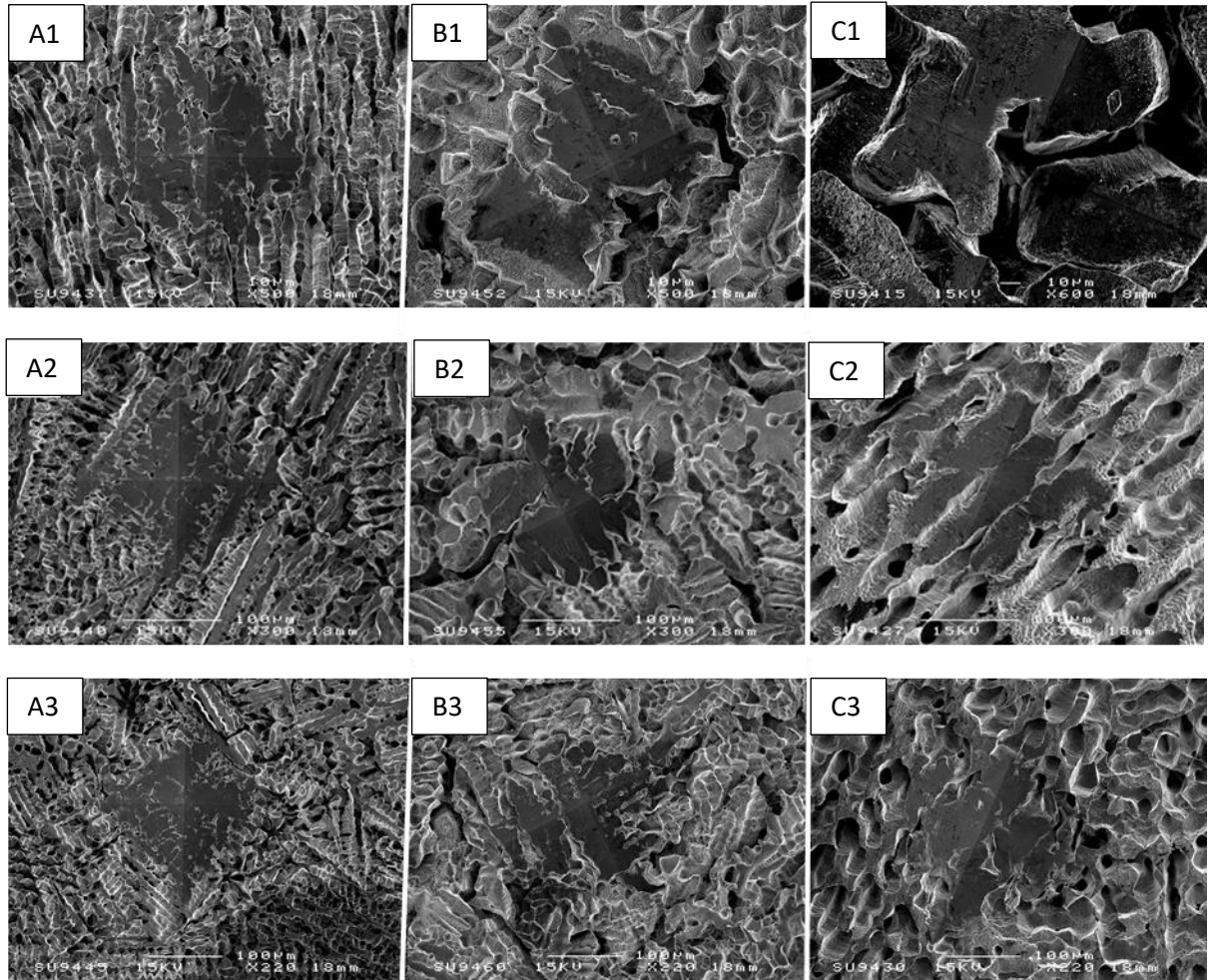
Figure 62. SEM images of indent locations, with A indents taken at 500x, B indented taken at 300x and C indents taken at 220x. (A1) rapidly cooled 1 kg load, (A2), rapidly cooled 2 kg load, (A3) rapidly cooled 3 kg load. (B1) rapidly cooled and heated 1 kg load, (B2) rapidly cooled and heat treated 2 kg load, (B3) rapidly cooled and heat treated 3 kg load. (C1) slow cooled 1 kg load, (C2) slow cooled 2 kg load, (C3) slow cooled 3 kg load.

The software used by the Durascan to identify the exact limits of the indent began to produce many inaccurate results with manual intervention needed to obtain an approximate size of each indent. This is also likely to contribute to the variability seen in the values recorded. From the images in Figure 62 (A1-A3) the porous structure has closed in towards the center of the indent as the result of the deformation caused by the indenter.

As the weight increased the level of deformation and the volume of alloy that deformation occurred over increased, as shown in the images in Figure 62 (A2, B2 and C2), which are at lower magnification than those in Figure 62 (A1, B1 and C1).

The same trend that was present in the 1 kg mass testing is present in the 2 kg mass testing, the deformation appears in the images shown in Figure 62 (A2 and B2) to completely close the structure, removing the porosity. However, in Figure 62 (C2) where the pores have been closed due to the deformation a clear boundary is still visible between them, this is not present in Figure 62(A) or (B).

The magnification used in Figure 62 (A3, B3 and) C3 had further reduced to accommodate the larger indent size that was found after testing with 3 kg load. The large indent now penetrates and affects more bulk material with the size now consistent across all three samples indicated by a similar indent depth (Table 17), the hardness values measured Table 16 are now largely influenced by the underlying non porous bulk alloy.

The hardness of the porous material was highly influenced by the pore size rather than the relative porosity value, as all three samples had a similar relative porosity. This influence was most clear when a low load was used. As this has the minimal indent depth it is most strongly affected by local differences present in the structure. As the load used to indent was increased the contribution from the different structures across the samples was minimized and relative porosity contributes to the reduction in hardness measured compared to the bulk hardness of the alloy.

4.6   Concluding Remarks

The nickel-copper alloy system has through solute partitioning using different solidification regimes produced a two-phase microstructure in which the copper-rich phase was removed to form a porous structure. It has been shown that the relative level of porosity is linked to the alloy composition, with all 3 samples having a similar relative porosity (52%-60%) and the pore size (17µm, 30 µm and 66 µm) linked to the solidification regime as this is responsible for the size of the regions with high enough copper concentration to be removed. It has also been shown that heat treatment can be used to influence copper distribution, locally increasing it and as a result increasing the post cast pore size. Examination of the pore structure on non-planar samples shows that an interconnected network has been produced, while hardness testing has shown that the hardness value and the depth of the indent is both a function of the pore structure and the indent load. The greater the load the more influence the underlying bulk properties have.

5 INFILTRATION CASTING OF Ti-811 RESULTS AND DISCUSSION

The method attempted here to produce a porous alloy is the replication process. In this method, a preform is placed inside a mould and a liquid alloy is cast around it, often with some additional pressure applied to ensure infiltration. The preform is removed after casting with the resultant pores replicating the preform geometry. In this work the selected preform material was sodium aluminate ($NaAlO_2$) it is stable to 1650°C, and can be formed by pressing from powder into the shapes required to produce a preform, crucially it is water soluble, which will enable it to be easily removed from the cast metal post infiltration. The metal selected was titanium alloy (Ti-811) the physical properties of Ti-811 are shown in Table 18.

Table 18. Physical properties of Ti-811

Property	Value
Density (g/cm^3)	4.37
Liquidus (°C)	1540
Beta transus (°C)	1040
Electrical resistivity (μΩ.m)	1.97
Thermal conductivity (W/m.k)	6
Young's Modulus (GPa)	120
Shear Modulus (GPa)	46

These two were selected as a pair of materials which meet the required specification to allow infiltration to occur. The titanium alloy Ti-811 has a liquidus temperature of 1540 °C which is 110 degrees below the temperature at which the $NaAlO_2$ begins to degrade thermally (1650 °C). This is similar temperature difference seen in aluminium infiltrated into NaCl preform (melting temperature difference of 140 degrees). The experimental procedure can be found in section 5.4. A variety of different experimental equipment was used while none of it was ideal or purpose built for replication casting of titanium, it's use could be modified to enable the production of testable samples to validate the process and characterise the results.

5.1   Infiltration by Arc Melting and Suction Casting

To process a metal foam using infiltration the first requirement is for the equipment is to be capable of heating the alloy above its liquidus temperature. Arc melting equipment with suction casting facility was used.

The second requirement is that enough pressure is generated to infiltrate the melt into the cavities between the preform particles. The equipment available can generated an infiltration pressure of approximately 50800 Pa.

The maximum infiltration pressure produced by the rig can be used to calculate the minimum radius of a cavity. Using the Young-Laplace equation:

$$p = \frac{2\gamma cos\theta}{r} \tag{22}$$

where p is the infiltration pressure, γ is the surface tension of the liquid and r is the minimum radius, and taking the most extreme case that the Ti 811 does not wet the sodium aluminate at all, ($\theta = 0$ and $cos\theta = 1$), the equation simplifies to,

$$p = \frac{2\gamma}{r} \tag{23}$$

Taking $\gamma = 1.46$ Nm^{-1} [121], and $p = 50800$ Pa, the minimum r is approximately 57 µm. This value is very small when compared with the particles being used, so good infiltration is theoretically possible at these pressures with particle sizes 1 mm^3 – 5 mm^3. As the alloy infiltrates into the mould is will cool and solidify on contact with the perform, this will reduce the channel (r) that the molten alloy can flow into. This reduction in r will have an impact on the depth of infiltration that is possible at a constant infiltration pressure. Increasing the pressure or increasing the particle size which in term increases the size of the channels between them are methods which can be used to increase the infiltration depth.

The final consideration for the suitability of the equipment concerns the appropriate amount of alloy melt required to fill the mould. This will be the alloy required for the charge. This

calculation is based on the simple volume of the mould and the density of the alloy. The volume of the cylindrical section of the mould is 1.56 cm^3. The mass of Ti 811 alloy required to fill an empty mould is 6.8 g. The mould will be filled 50 vol % with $NaAlO_2$, a charge of at least 6 g will be sufficient for infiltration.

5.1.1 Iterative Process Development, Infiltration aided by Suction Casting

A series of iterative experiments have taken place to produce a metal foam from Ti-811, the process parameters for all iterations is shown in Table 19.

Table 19. Process parameters used for infiltration suction casting of Ti-811.

Casting Iteration No.	1	2	3	4
Mould Fill Level	2/3	Full	3/4	3/4
Evacuated Cylinder Volume (cm^3) or Vacuum Pump	25	250	250	Vacuum Pump
NaAlO$_2$ Particle Size (mm)	1-1.18	1-1.18	1-1.18	1-1.18
Arc Power (V)	550	550	550	550
Infiltration Pressure (Pa)	50800	50800	50800	50800

* Greyed boxes are parameters which were not changed.

The infiltration over pressure was constant across all iterations, the maximum available, this would allow for the deepest infiltration. The arc power used to melt the sample was also set to 550 V this value was sufficient to melt the alloy. Finally, the particle size was not changed as this size provided a preform that could produce more that twos cells in across the diameter of the mould. The two conditions that were changed, the mould fill level and the strength suction these were varied to establish the optimum balance between the volume of the preform to be infiltrated and the pressure required to infiltrate that volume.

Iteration 1 - Benchmark Infiltration

The conditions for the first iteration acted as a benchmark for the infiltration suction casting, with both the fill level (preform volume) and suction pressure at middle at the lower end of the what was available. The results for each iteration casting are discussed in turn, along with the process development changes which were made.

The first mould assembly was produced by placing the two halves together and half filling the cylindrical section with the NaAlO$_2$ particles and allowing them to settle naturally. The copper mould was only half filled as a precaution against the alloy being superheated during melting due to the lack of any temperature sensing in the arc melter equipment. The assembly was then

placed in the fixed humidity chamber for 24 hours, then removed and placed in a furnace at 50°C for 24 hours to dry out the sodium aluminate and help bond the particles together.

Once the casting operation was complete it was observed that a large proportion of the alloy had solidified above the mould cavity, see Figure 63 (A). The copper mould assembly was removed and opened to reveal the cast.

Figure 63. A photograph of the first replication casting iteration. Sodium aluminate can clearly be seen on the left of the casting. (A) with the residual Ti-811 in place. (B) with the residual allot removed.

In Figure 63 (A) and (B), sodium aluminate can clearly be seen on the far left of the photograph with the Ti 811 alloy infiltrating a small extent (5-10 mm). A lustrous surface was present on the button with little oxidation visible on the surface; the same was seen on the Ti getter, confirming the casting had taken place in a clean atmosphere. The residual alloy was cut without the use of lubricant to preserve any sodium aluminate present; the result is shown in Figure 63 (B).

The most important observation was that the stem of the infiltration was not a solid lump of Ti 811 alloy but a hollow tube with an infiltrated section at the bottom.

This small extent of infiltration may be attributed to the preparation of the first assembly; the sodium aluminate particles were not packed into the cavity but allowed to settle under gravity to a depth of 25 mm; this resulted in the melt having to travel down the cooled mould reaching the freezing range of the alloy before it contacts the $NaAlO_2$. This travel to the $NaAlO_2$ could be the reason for the limited infiltration as the decrease in temperature, will increased viscosity of the alloy that results making infiltration more difficult.
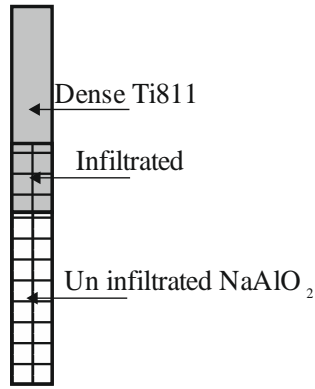
Figure 64. A schematic diagram of the $NaAlO_2$ fill level shown by the patterned section and the amount of infiltration shown by the grey area.

The depth of infiltration into the $NaAlO_2$ was approximately 10 mm, however this was observed from outside before the $NaAlO_2$ was dissolved, giving no indication of the extent of internal infiltration. It is possible that the sodium aluminate may have been packed down during the viscous melt infiltration, which could also have hindered a deeper infiltration as more densely packed beds of particles will be harder to infiltrate into.

The sodium aluminate was removed by placing the partially infiltrated casting into a heated (80°C) water bath for 4 hours, with the water changed every hour. A final 2 hours in an ultrasonic bath was used to remove any residue from with the casting. Once the casting was free from sodium aluminate the depth of infiltration is shown in Figure 64. The sample was prepared for SEM imagining by removing the excess material forming the tube.
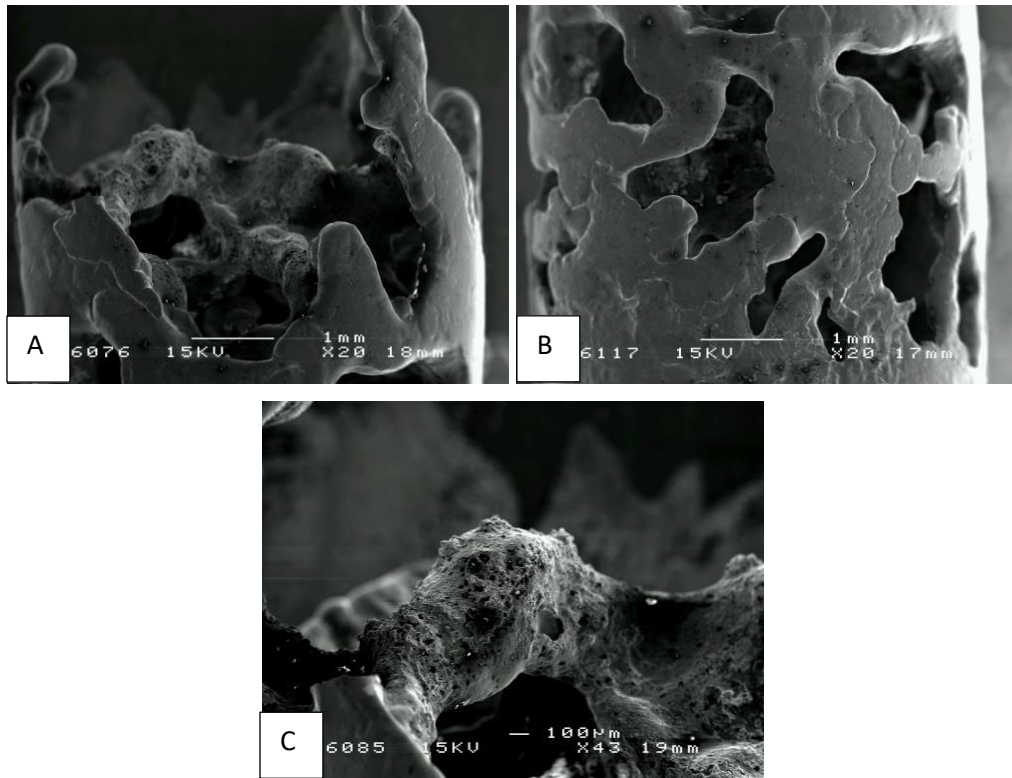
Figure 65. SEM images of replication cast Ti811, (A) Showing the infiltration tendrils, (B) From the side of the replication casting showing pores on the surface open the center cavity and (C) An image of a strut which was in direct contract with the $NaAlO_2$

The material that infiltrated the greatest distance through the sodium aluminate is shown in Figure 65 (A) and (B), the ends of these tendrils are rounded providing evidence that they are the very tips formed during solidification, and have not been broken off and have solidified in free space (not in contact with the preform)

The smooth surface seen in Figure 65 (B) was produced from the solidifaction of the Ti811 alloy on the water-cooled copper mould surface. The large pores (approximately the particle size 1-1.18 mm) seen on the surface were caused by the molten alloy flowing around groups of sodium aluminate particles touching the mould surface preventing uniform flow of the alloy down the inside of the mould.

An interconnected network of struts can clearly be seen in Figure 65 (A). This network was formed by the infiltration of Ti811 alloy between particles or groups of bonded particles of sodium aluminate. This confirmed that the infiltration pressure was sufficient to force the Ti811 alloy between the particles to some degree.

The surface struts are shown in Figure 65 (C). This surface was in direct contact with the sodium aluminate during solidification processing. The surface is uneven and textured; this texture is mostly likely a replication of the surface of the sodium aluminate particles which were crushed and as such have an angular fractured surface.

Figure 66. An optical image of a cross section of the replication casting.

The replication casting was vacuum impregnated with epoxy resin then ground and polished to show the cross section at the center, which allowed the central pore network to be viewed in profile. This revealed that the extent of infiltration was less than the observation of the surface would suggest, see Figure 66. It also appears that the internal struts themselves contain large amounts of porosity. It could be that chill cooling of the molten metal as it comes in contact with the copper wall or sodium aluminate blocks the ingress of further melt preventing complete infiltration.

Increased Suction and Maximum Fill Level - Iteration 2

For the second iteration, the following changes were made to the casting procedure in order to address the issue of premature freezing of the alloy during infiltration. Firstly, the $NaAlO_2$ was packed into the copper mould filling to a depth of 50 mm and the temperature the drying furnace was set to, the temperature was increased from 50°C to 150°C, this increase was to ensure the particles were more fully bonded and thus better able to resist the pressure of the melt during infiltration. The reasoning for this increase in depth was to mitigate the cooling of the alloy melt as it travelled towards the $NaAlO_2$. If the alloy melt is at a higher temperature it will be less viscous and remain liquid for longer and able to better infiltrate the $NaAlO_2$. The force of the infiltration was also increased, by increasing the evacuated chamber size from 25 cm^3 to 250 cm^3, to increase the speed of the molt alloy so that it travels further into the preform before solidifying.

Figure 67. A photograph of the copper mould ready to be placed into the arc melter, with the $NaAlO_2$ visible at the top of the opening

The two part copper mould was joined to the base plate before being placed into the hearth; the $NaAlO_2$ is visible in Figure 67, indicting the very short depth the alloy will have in which to cool before infiltration.

The second iteration did not result in a successful casting, to investigate this, the copper mould was removed from the heath after the casting operation, the base plate was removed and the copper mould separated to investigate the effect the casting process had on the $NaAlO_2$. No

infiltration occurred in this casting, which was indicated by the mass of Ti811 alloy remaining above the casting cavity before the mould was separated.

Figure 68. A photograph of the copper mould after casting with NaAlO2 still in-situ showing zero infiltration.

It is clear from Figure 68, which shows half of the assembly after casting. This failure was caused by changes that were made based on the knowledge gained from the first casting.

These changes resulted to zero infiltration depth. There was some evidence of melting of the NaAlO$_2$ visible within the top 5 mm of the assembly once it was opened; this is likely to be the major factor preventing the infiltration, combined with the larger depth of the NaAlO$_2$ bed, which will have a reduced permeability to gas and so could reduce the effective pressure seen by the molten metal. It would even be possible that the presence of particles near the mould opening would prevent a good seal between metal and mould being obtained.

Increased Suction and Optimised Fill Level - Iteration 3

The third infiltration casting iteration used a different strategy to address the problem of limited infiltration. The increased drying temperature was used again for preform preparation, as there was no evidence that this had a detrimental effect and gave increased strength to the preform. To address the problem of potential melting of the $NaAlO_2$, the mould was packed to a depth of 30 mm (3/4) with the $NaAlO_2$, allowing some space for the alloy to melt before coming into contact with the $NaAlO_2$. The speed and driving pressure of the infiltration was kept at the maximum (using the large evacuated cylinder) by to draw the molten alloy into the $NaAlO_2$, this was to counter the chill cooling of the alloy before it becomes too viscous to flow into the pores between $NaAlO_2$ particles.

The casting operation resulted in much less residual alloy above the mould, with the formation of a hollow tube in the alloy. The copper mould was opened to reveal the extent of the infiltration, Figure 69.
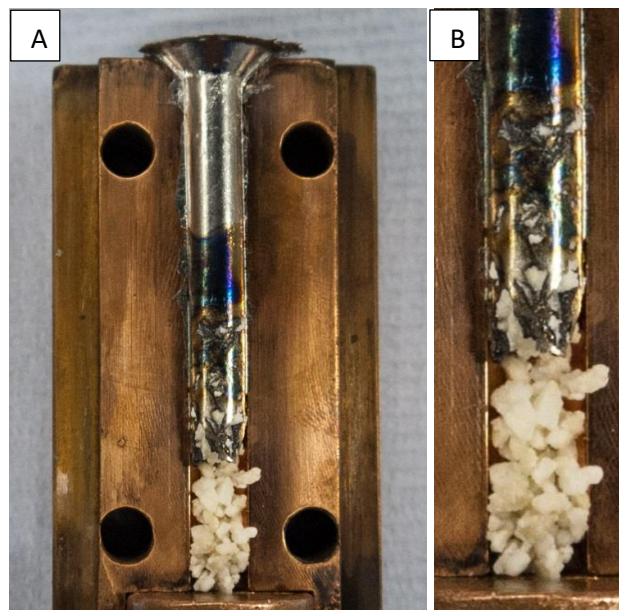
Figure 69. (A) A photograph of the opened copper mould (6 mm diameter) with the casting still in place. (B) an enlarged view of the infiltration, The extent of the infiltration can clearly be seen.

The $NaAlO_2$ remaining at the bottom of the copper mould which had not been infiltrated did not show any signs of melting or of being compacted, in Figure 69 (B) the open pore networks could still be seen. This confirmed that the modifications to the preform preparation method, performed as expected and these conditions were kept in future iterations.

The Ti811 alloy had infiltrated to a depth of 15 mm, this value was measured externally from where the $NaAlO_2$ could first be seen penetrated by the alloy to the furthest depth the alloy reached. There is depth 15 mm of $NaAlO_2$ remaining.

Optimised Suction and Optimised Fill Level – Iteration 4

In order to improve the depth of infiltration the evacuated cylinder of the equipment was replaced with a vacuum pump. Rather than depleting all the suction pressure as soon as the process was begun, the vacuum pump continued to pull on the liquid alloy until it solidifies. This continuous suction should draw the alloy deeper into the $NaAlO_2$ and produced a larger porous sample.

The sample was cut without lubricant to remove the excess alloy. To reveal the internal pore structure it was ground half way through its diameter.

20 mm
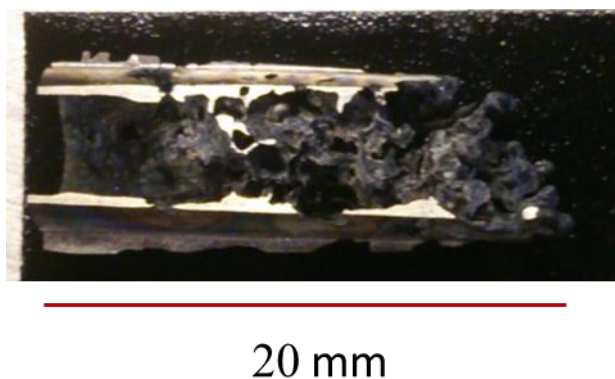
Figure 70. A photograph taken of the cross section of the infiltration cast Ti-811

A compact and extensive internal pore network can be seen in Figure 70, on the inside of the casting. The section was then imaged under the SEM to look at the details of this network see Figure 71 (A) and (B).
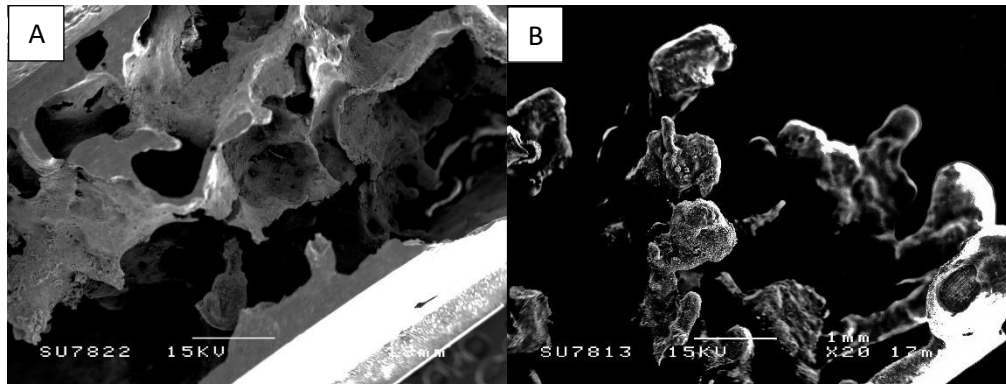
Figure 71. A SEM image of the cross section of the infiltrated Ti-811 alloy, (A) showing the network of struts on the inside that have formed. (B) Showing the tips of the infiltration tendrils from the deepest infiltrated Ti-811 alloy. (Scale bar shown 1 mm)

The higher magnification image shown in Figure 71 (A), allows the full extent of the infiltration to be seen. Relatively large volumes of material had moved between the $NaAlO_2$ particles, with some of the structure which had been formed clearly the result of solidifying around a particle which has been subsequently removed. The casting showed a well-developed solid outer skin which may indicate that the molten alloy had flowed down the mould outer diameter. The fact that alloy had formed a hollow tube of material while it travelled down the mould before it had reached and begun to infiltrate supports this.

The rounded ends of the deepest infiltration tendrils shown in Figure 71 (B), indicate than they have solidified freely supporting the case that the high cooling rate of the water mould on the alloy is the main cause in this case for the relatively shallow infiltration depth achieved.

5.1.2   Summary of Infiltration Casting by Arc Melting and Suction Casting

The work using the arc melter proved that the molten Ti811 alloy can infiltrate the $NaAlO_2$ and that a porous structure can be produced. The process was refined over 4 casting operations with the final casting producing an infiltration depth of 15-20 mm, the center of the porous metal had an extensive pore network. However, the arc melter has several limitations which are restricting what can be produced using the equipment, the high cooling rate of the mould results in a very short window for the infiltration narrowed further as the alloy cannot be continually heated during the infiltration process. The size of the final casting is taken from the mass of alloy which can be processed in the arc melter which is limited to around 12 g of material. The challenges of narrow processing window due to alloy cooling can be improved by changing the heating method used to melt the alloy. A second benefit of moving to a different heating system is the increased volume of material that can be processed.

5.2   Infiltration by Induction Melting

When moving to use induction melting the following changes were made compared with arc melting; the copper mould assembly was replaced with a quartz crucible. The specification for the induction heating equipment available requires the crucible to fit into a two part copper jacket with a two rubber gaskets in order for argon gas to flow into the crucible and provide the infiltration pressure. The infiltration pressure supplied by the argon gas to the quartz crucible ranges from 1-6 bar (100000-600000 Pa), this is a greater driving force than used with the arc melting equipment (50800 Pa), which proved sufficient to produce some infiltration. The maximum diameter for the quartz crucible is 14 mm, thus this size was used to maximise the size of porous alloy that could be produced, the volume available increases from 1.56 cm^3 to ~5 cm^3. The clear nature of the quartz allows for the melting to be observed and the infiltration process to be initiated as soon as the alloy is liquid to prevent significant super heating and the potential for melting the NaAlO$_2$, Figure 72.
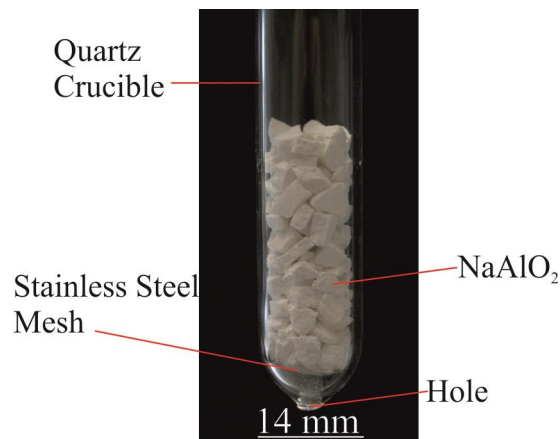
Figure 72. A photograph of the quartz crucible with large NaAlO$_2$ particles in-situ before infiltration.

The height to which the NaAlO$_2$ was packed was chosen due to the restriction of the equipment, as the alloy must be placed on top of the NaAlO$_2$ and the induction coil must be placed around this section in order for it to melt. To ensure the alloy location matches that of the induction coil the maximum packing height shown in was used see, Figure 72.

5.2.1   Iterative Process Development, Induction Melting and Infiltration Casting of Ti-811

A series of iterative experiments have taken place to produce a metal foam from Ti-811 suing induction melting, the process parameters for all iterations is shown in Table 20. The results for

each iteration are presented along with a discussion on changes which were made and the reasoning behind those changes as part process development.

Table 20. Process parameters used for induction melting and infiltration casting of Ti-811.

Casting Iteration	1	2	3	4	5	6	7	8
NaAlO$_2$ Size (mm)	1-1.18	5	5	5	5	5	5	5
Crucible Material	Quartz	Quartz	Quartz	Quartz	BN	BN	BN	BN
Infiltration Argon Pressure (bar)	3	4	4	4	5	4	2	1
Infiltration Pressure Application Method	Burst	Burst	Flowing from the start	Flowing from the start	Flowing from the start	Flowing from the start	Flowing from the start	W slug and gas flowing from the start
Time for Melting in (s)	15	15	15	15	15	15	20	20
Induction Power	800	780	780	780	780	780	780	780

Benchmark Induction Melting Infiltration – Iteration 1

The first iteration of induction melting used same size of the NaAlO$_2$ particles Figure 73 (A), as used with the arc melter suction cast experiments to allow the results to be compared. A pressure of 3 bar was chosen to give scope for it to increased or decreased as required, which the instant application (burst) similar the pressure application of suction casting.
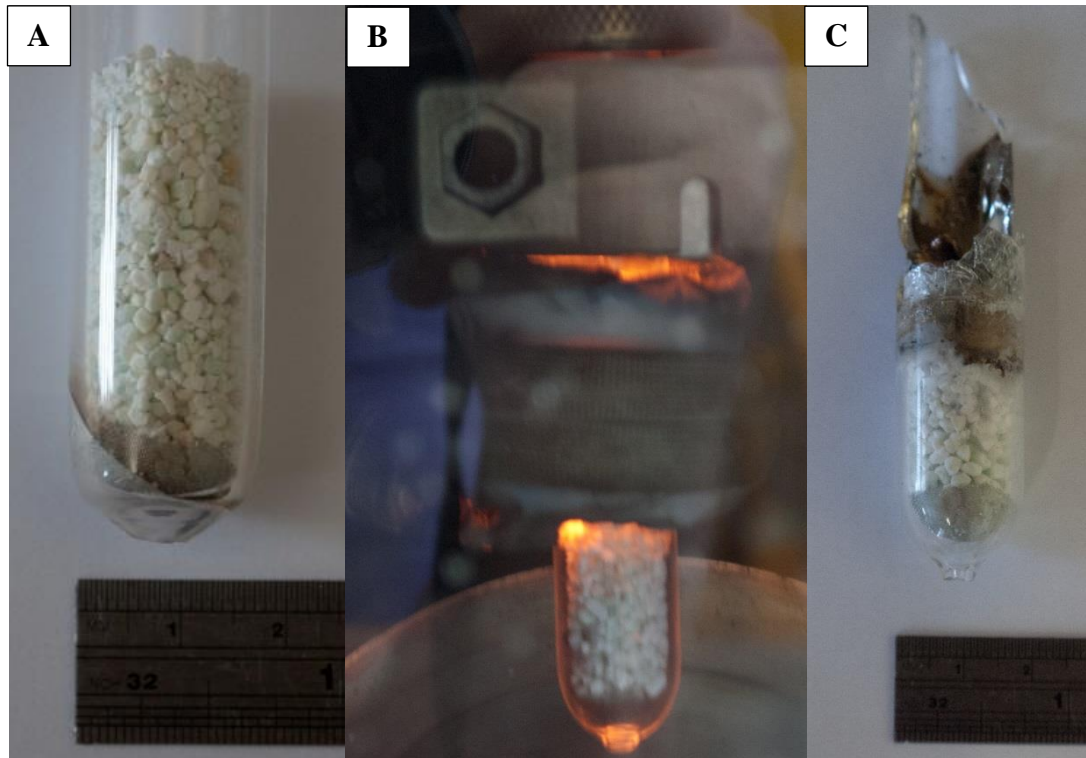
Figure 73. (A) A photograph of a quartz crucible with sodium aluminate particles (1-1.8 mm) in place ready for infiltration. (B) A photograph taken through the observation window during induction heating. (C) A photograph of the quartz crucible with Ti-811 alloy in-situ taken after the inflation operation.

The first casting showed limited success, with little infiltration visible from outside the crucible. The thermal shock from the casting caused the crucible to shatter around the molten alloy, Figure 73 (C). The quartz crucible was broken open to remove the cast alloy, which revealed no infiltration in the sodium aluminate preform. The conditions of processing had to be changed for the next infiltration to improve the depth of infiltration.

Increased Preform Particle Size and Increased Infiltration Pressure - Iteration 2

The changes made for the second iteration were increasing the sodium aluminate particle size to approximately 5 mm square. These larger particles when packed offered larger channels, which would allow the alloy to flow more easily, and thus lower pressures will be needed for infiltration. The lower outwards pressure should help to preserve the integrity of the crucible for longer and hence allow for deeper infiltration.

Figure 74. A photograph post infiltration using larger particles than the previous infiltration.

The results of the infiltration of iteration 2 can be seen in Figure 74. The large particles did not on their own result in a greater depth of infiltration; tendrils of alloy can be seen on the inside of the crucible, in Figure 74. The prolonged time of the infiltration had acted to push the molten alloy out against the crucible. As the softening temperature of the quartz (1670 °C) is close to the casting temperature used, the stress of the infiltration pressure appears to have caused it to fail; the alloy solidified with a bulge showing where it pushed outwards against the softened crucible. This failure of the crucible was attributed to the poor depth of infiltration, as the pressure could not be relieved in the intended manner of metal progressing through preform.

The location of the fracture made removal of the casting sample, however the extent of infiltration was limited and lost integrity when removed, meaning this sample could not be characterized further.

Continuous Infiltration Pressure Delivery - Iteration 3

In iteration 3, the delivery of infiltration pressure to the set up was changed. In the first two iterations the pressure was applied after the 15 seconds heating time and Ti811 alloy melted, it was felt that this sudden burst of pressure will exacerbate the issues of crucible softening. In iteration 3 the argon was set flowing before the induction melting took place, so that as soon as the alloy was liquid it began to infiltrate the $NaAlO_2$.

Figure 75. Two photographs of the large particle continuous argon infiltration which show tendrils of alloy in at least two locations

The changes made resulted in a greater degree of infiltration than the first castings. This crucible did not fail during the casting but afterwards as it cooled, possibly due to differential thermal expansion induced stresses. The casting was fixed in the crucible, so the $NaAlO_2$ dissolution step had to be performed before removal. This was done by placing the whole crucible in a beaker of water at 60 °C and stirring it with a magnetic flea (300 rpm). The water in the beaker was replaced every 15 minutes as it becomes saturated over time with reaction products $NaAl(OH)_4$ (equation 17), Figure 76.

Figure 76. A photograph of in-crucible dissolution of $NaAlO_2$.

The sodium aluminate dissolved to a point where the Ti-811 alloy could be released from the crucible and the dissolution continued freely within the confines of the crucible.
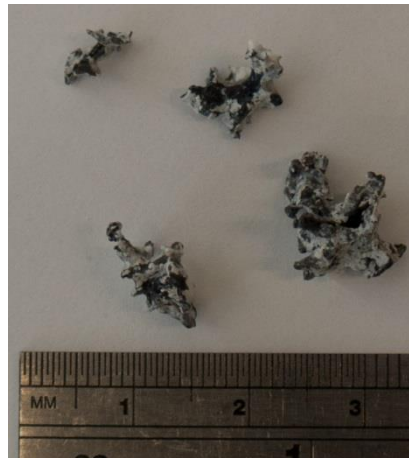
Figure 77. A photograph of the infiltrated Ti-811 that was removed from Figure 76.

The $NaAlO_2$ was acting to hold the alloy together, as when it was removed the casting lost structure due to its limited integrity. Nevertheless, a significant volume of the alloy had infiltrated into the preform, Figure 77. The structure of the infiltrated sections which held together show that production of a porous structure was possible using this method. The largest of these central infiltrated sections was prepared for optical microscopy (as described in section 3.6) see Figure 78.
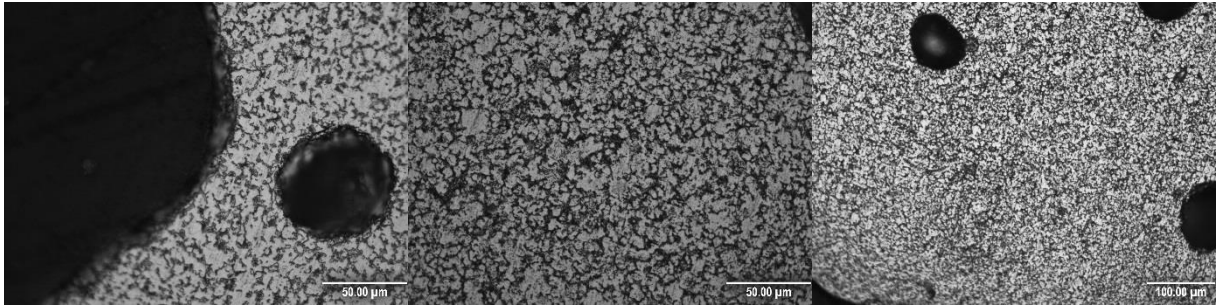
Figure 78. Optical micrographs of the central strut network produced during infiltration into the NaAlO$_2$ preform.

The network of struts formed in the internal structure had low porosity with only a limited number of large pores likely caused by gas bubbles (as they are round). The microstructure is globular alpha, the light areas in Figure 78, is a alpha/beta matrix with little retained beta due to the low levels of beta stabilising (1 Mo and 1 V) elements in the alloy, the globular microstructure is due to the relatively slow cooling rate [122].
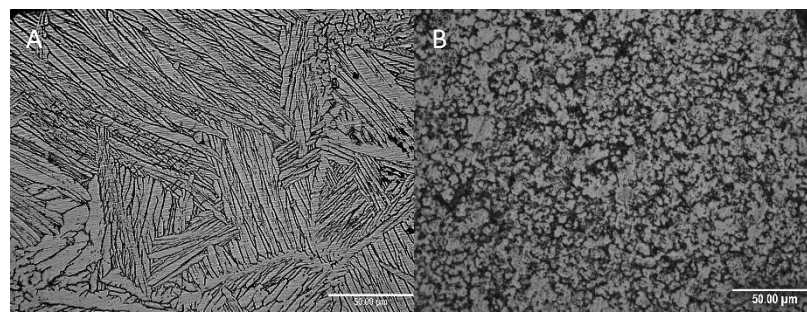
Figure 79. (A) An optical micrograph of Ti-811 alloy taken after processing in the arc melter. (B) An optical micrograph of Ti-811 alloy after processing in the induction melter.

In contrast a sample of Ti-811 alloy produced in the arc melter Figure 79 (A) has a basket weave structure of alpha lamellae, again with little retained beta phase, indicating that this alloy was cooled at much faster rate that the induction melted sample, which is the case with these two variations in melting and processing techniques.

Improving the Post Infiltration Metal integrity - Iteration 4

In iteration 4 the same process conditions as iteration 3 were used as these showed promise and did produce some level of infiltration, in order to improve the integrity and toughness of the casting so it would remain intact on removal from the crucible, the sample was heat treated post cast while still inside the quartz crucible. The stress relieving heat treatment parameters used were 650°C for 90 mins followed by an air cool as described in [122]. The casting was removed from the quartz crucible and the $NaAlO_2$ dissolved away.

Figure 80. (A) A Photograph of infiltrated Ti-811 alloy while still in a quartz crucible pre heat treatment (B) Post heat treatment and removed from the quartz crucible

The stress relieving heat treatment did improve the strength of the infiltrated part as the fine structures produced did not break off during the dissolution of the $NaAlO_2$, Figure 80 and Figure 81. An additional cause of the embrittlement could be oxygen uptake during processing. To investigate this possible cause, a sample of the cast alloy was sent to LSM, Sheffield for chemical analysis with the results shown in Table 21.

Table 21. A chemical analysis comparing a sample taken from an infiltration experiment against the Ti-811 specification.

Element	Sample Analysed (wt%)	Ti-811 Specification (wt%) [122]
Ti	86.92	Bal
Al	8.39	7.5-8.5
V	0.85	0.75-1.25
Mo	1.85	0.75-1.25
Fe	0.21	0.3 max
Cu	<0.05	----
W	<0.05	----
C	0.130	0.1 max
N	0.038	0.04 max
O	1.6	0.15 max
H	0.055	0.015 max

The results from the chemical analysis show, that the concentrations of several elements in the composition were greater than specification, and a slight excess of molybdenum. The measured oxygen content of the alloy was 10 times the maximum specified level, this high oxygen level will have contributed to the embrittlement seen in the infiltrated alloy. The probable source of oxygen is the $NaAlO_2$ preform material as this will have been in direct contact with the alloy in a molten state at these temperatures titanium has a high affinity for oxygen, another potential source of oxygen pick up would quartz crucible itself. Sodium was not detected in the alloy after casting, so is not being incorporated into the alloy from the preform. The aluminum content is still within specification so it is unlikely that aluminium is being removed from the preform either.

Figure 81. A photograph of heat treated Ti-811 after removal of $NaAlO_2$

The infiltrated Ti-811 alloy in, Figure 81 indicates that once again the alloy can make its way into the larger spaces between the preform particles and that continuous argon pressure was providing a sufficient driving force for the infiltration to take place. However, the short infiltration time due to the quartz crucible softening and breaking off before the molten alloy has made is way deep into the preform is now the limiting factor on the scale of the porous metal that can be produced. In order to create a large porous structure the alloy needs to remain molten and under pressure for a longer time to allow it to flow deeper into the preform.

Improved Crucible Material and Increased Infiltration Pressure- Iteration 5

In iteration 5 and all following iterations the material used for the crucible was changed to boron nitride due to its much higher maximum working temperature of above 2000 °C. This means it should retain its strength at high temperature and not break during the infiltration, allowing for the infiltration to take place over a longer time and for the melt to travel further into the preform. The increased high temperature strength of BN over quartz allowed for the infiltration pressure was increased to 5 bar (from 4 bar) to drive the alloy deeper into the preform.
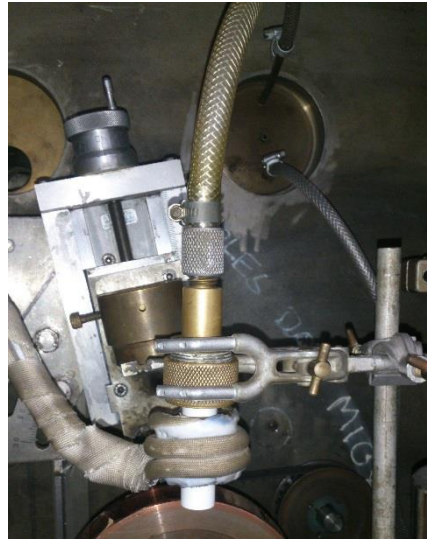
Figure 82. A photograph of a BN crucible in place in the induction heated infiltration rig

The infiltration rig was set up as shown in Figure 82, the argon line coming into the top of gas tight connecter joining the crucible to the argon supply to provide the infiltration pressure. The induction coil surrounded the crucible at the height of the alloy. The new crucible has a bright white appearance

Figure 83. A photograph of a BN crucible intact after being processed. Some surface degradation is present.

Once the infiltration was complete the crucible was removed from the rig, Figure 83. The crucible was still intact and retained its strength post infiltration, a significant improvement over the quartz crucible. Heating had caused some discolouration, mainly on the top half of the crucible where the induction coil was situated. The infiltrated alloy was easily removed from the crucible. Using a twisting motion and light pressure it was pulled free of the crucible further confirming the benefits of BN over quartz for this process.
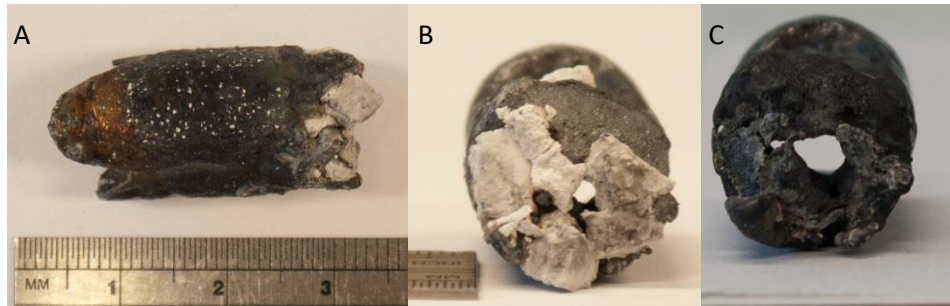
Figure 84. (A) A photograph side on of the infiltrated alloy removed from the BN crucible. (B) A photograph face on of the alloy removed from the BN crucible (C) A photograph face on of the alloy after the $NaAlO_2$ was removed.

The alloy was removed from the BN and the depth of infiltration became apparent, Figure 84 (A), a side on view, illustrates this effectively, viewing at the infiltration interface the most obvious feature is the hole down the center, Figure 84 (B) this has likely been caused by the flowing argon used to drive the molten alloy into the preform. The hole produced becomes more prominent once the $NaAlO_2$ has been removed, Figure 84 (C), as does the limited amount of infiltration in the core region of the casting.

Reduction in Infiltration Pressure - Iteration 6

Iteration built on the successful substitution of quartz with BN as the crucible material resulted in extending heating time during the infiltration, because of the improved high temperature resistance of the BN. However, this increased time lead to the formation of a hole in the casting where the argon gas was injected, the infiltration pressure was reduced from 5 bar to 4 bar to reduce size and depth of the hole that may be produced in the center of the casting during the infiltration process.
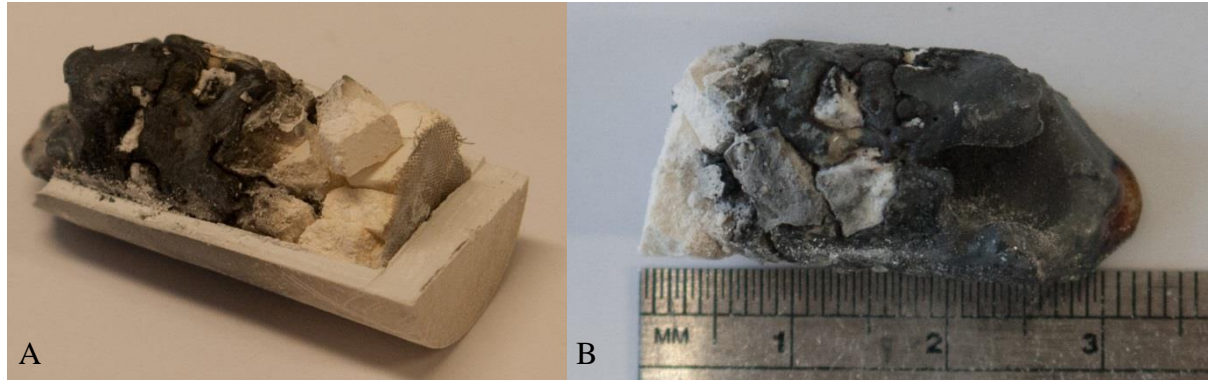
Figure 85. (A) A photograph of an infiltration with the crucible sectioned to view the alloy and preform in place before removal. (B) A photograph after removal from the BN crucible before the NaAlO$_2$ had been removed

The BN crucible could be cut with a standard hacksaw, from around an infiltrated casting to view how the molten alloy and the preform have interacted Figure 85 a). Cutting away the crucible resulted in less disturbance to the structure than sliding it free. The preform had retained its structure and importantly the infiltration pressure from the alloy had not caused the preform to collapse, meaning there was still the same amount of space between the particles. Once the casting was removed from the crucible, Figure 85 b), the extent of the infiltration was visible. The alloy has flowed between the particles to a depth of approximately 15 mm.

Figure 86. A photograph taken during the dissolution of the $NaAlO_2$ preform

The $NaAlO_2$ was removed using the method described previously. In Figure 86 it can be seen dissolving into solution from the bottom section of the casting as a white stream.

Figure 87. A photograph taken of the infiltration cast Ti-811 after $NaAlO_2$ removal

The removal of the majority of the $NaAlO_2$ from the infiltrated alloy revealed that the infiltration path of the molten alloy was predominately around the circumference as the center section again displayed a hole taking up roughly a third of the diameter. The infiltration that had taken place around the circumference did also show sign of moving towards the center than resulting in a limited network of strut and tendrils, Figure 87.

Increased Heating Time and Further Reduction in Infiltration Pressure - Iteration 7

Iteration 7 built on the lessons learned from all the previous castings, the infiltration gas pressure was further reduced and the process time increased. This would have a twofold effect; the reduced pressure would prevent a hole being blown in the center of the alloy and the increased time at temperature would give the alloy longer to infiltrate into the preform. The changes were intended to compensate each other, keeping the alloy molten for longer would facilitate material flow without the additional driving force of a large pressure gradient.

Figure 88. (A) A photograph of an infiltration cast with long tendrils of alloy. (B) An alternative view of the infiltration. (C) A photograph of the central pore network that formed

The conditions used to produce this casting resulted in the deepest infiltration at a single location, this spur can be seen to branch at multiple points along its length as it has made its way into the preform, Figure 88 (A) and (B). The sample also displays the same tendency for the molten alloy to flow down the side of the crucible before moving towards the center, this may reflect the general flow direction of the argon gas.

This sample represents the best that was achieved by the induction melting infiltration route, and illustrates the limitation of this method. As the pressure is applied on the molten alloy, it will progress down the largest spacing in the preform, as the threshold pressure required for these is

greatest. Even if the alloy is maintained in the liquid state for a long time, it may not allow the whole preform to become filled. At some point, a finger of alloy will reach the exit hole and the process is then likely to stop, as it will not be possible to evacuate further air from the crucible. For a fully successful infiltration therefore, a process that can press the molten alloy into the preform against a vacuum is required.

Modified Pressure Application Method - Iteration 8

In iteration 8, a modified method to apply pressure to the molten alloy to increase the driving force for infiltration was to place a tungsten cylinder above the alloy in the crucible. As the alloy melts tungsten applied a uniform pressure across the surface of the charge (353 Pa from the mass of the W slug and 100000 Pa from the 1 bar gas pressure) forcing the molten alloy into the preform.
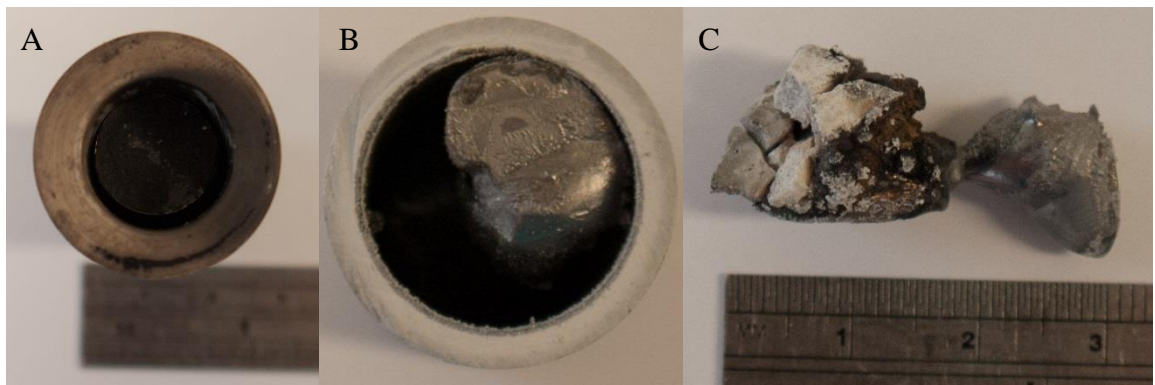
Figure 89. (A) A photograph viewing down the crucible with the W cylinder in place. (B) A photograph viewing down the crucible once it had been cut above the infiltrated alloy. (C) A photograph of the infiltrated alloy using a W cylinder to apply pressure

The infiltration took place using the processing conditions in Table 20. In Figure 89 (A) the top of the tungsten cylinder after processing can be seen. The tungsten cylinder had dropped approximately 15 mm into the crucible post processing, a strong indication that the alloy had also moved into the preform. The tungsten cylinder did not melt or bond to the alloy so could be slid out of the crucible, which was then cut at the level of the infiltrated alloy to allow the easier removal. The top of the alloy showed very limited signs of melting. If complete melting had occurred the alloy would completely fill the crucible, whereas in Figure 89 (B) it is still intact and has not flowed to fill the crucible. The infiltrated alloy was removed from the crucible. Figure 89 (C) shows infiltration had occurred to an approximate depth of 10 mm. However, this infiltration was more likely been caused by gravity as one part of the bulk alloy placed into the crucible remained separate (two pieces of Ti-811 were used to charge the crucible). If the total

mass of Ti-811 had melted it would have agglomerated into a single piece. The probable cause of this uneven heating is that the heating zone of the induction coil is limited, and in order to help the molten alloy flow in the preform the coil sits partly at the alloy charge location and partly over the preform so that when the alloy melts and flows it can be continually heated and kept molten during the whole infiltration. This positioning was to limit any effects on the heating/cooling of the molten alloy caused by the placement of the tungsten. This explains why only the bottom section of the charge has melted fully and begun to infiltrate and why the top section has only been heated enough to deform from the weight of the tungsten cylinder but not flow onto the bottom section and create a single molten mass. The cooling effect of the contact with the tungsten cylinder may have reduced the effectiveness of the induction heating in the time (20 s) given for the melting to occur.

5.2.2   Summary of Infiltration casting by Induction Melting

The use of the available induction melting equipment to melt and infiltrate Ti-811 into the preform was very challenging. Infiltration and the early formation of a porous structure has been demonstrated to some degree in some samples and the sodium aluminate preform material has shown that it can be removed from the infiltrated alloy. The process conditions were refined with varying levels of success, indicating that some amount of process control is possible with the equipment used. However, no samples were produced large enough for testing or characterising.

5.3 Infiltration by Vacuum Furnace Melting

To overcome the limitations of the induction melting equipment to heat a large quantity of alloy uniformly, a further experiment using a tungsten cylinder to provide the infiltration pressure was performed in a vacuum furnace to provide the heat input to melt the alloy. This would heat the whole of the alloy charge and facilitate total melting and infiltration into the preform. The processing conditions were a vacuum lower than $5x10^{-9}$ mbar, heating rate of 10°C/min to a temperature of 1600 °C followed by an immediate furnace cool. Figure 90 (A) is a photograph of the BN crucible prior to being placed in the furnace, a larger volume of preform was used as there was a larger mass of Ti-811 alloy to allow for maximum chance of infiltration, as such the tungsten cylinder sits proud of the crucible opening.
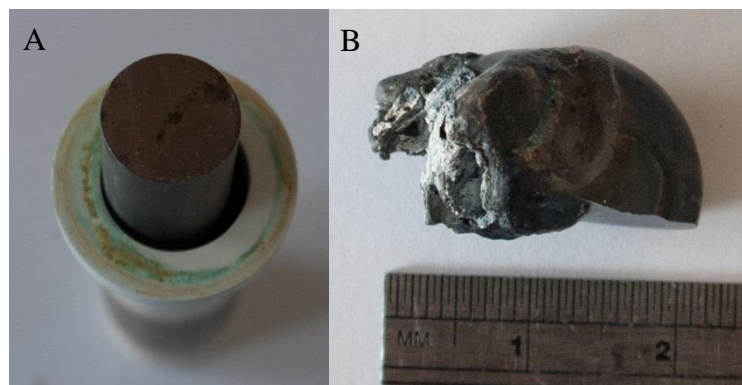
Figure 90. (A) A photograph of the BN crucible prepared for the furnace with the tungsten cylinder in place resting on the Ti-811 alloy. (B) A photograph of the alloy after it had been removed from the crucible

The reason for the minimal hold time at the maximum temperature was the proximity of the Ti811 alloys liquidus and thermal stability of the preform, as such any superheating of the alloy would have resulted in collapse of the pore structure in the preform. The risk of collapse was increased due to the tungsten mass continuously acting on the alloy and the preform. The short minimal hold was expected to allow the alloy to melt and flow with the aid of the pressure from the tungsten cylinder into the preform. However, when the infiltrated alloy was removed, Figure 90 (B), only a very limited amount of infiltration had occurred, with the alloy only progressing a short distance into the preform. The removed alloy shows signs that limited melting had taken place. The limited melting is most likely to have been a result of the alloy not getting to the required temperature, as the control thermocouple was not touching the alloy but the plate the crucible was sat on and thus not reading the temperature of the alloy accurately. The result will have been the alloy not reaching the correct temperature given the tight tolerance on the temperature range required to melt the alloy and not affect the preform.

The use of an alternative method to apply pressure required for infiltration showed some initial success, in the case of placing the tungsten cylinder on top of the alloy and using the induction heating method, some though limited infiltration had taken place. This method may be suitable for development in the future as a way to more evenly apply pressure once the alloy has melted. The use of a vacuum furnace to melt the alloy and of a tungsten cylinder to apply pressure was unsuccessful in the one trail run, this has be attributed to the alloy not fully melting during the process so it was impossible for it to infiltrate the preform, no further trails were run in the vacuum furnace as the development of a new set of testing and evaluation parameters would have been needed.

5.4 Concluding Remarks on Infiltration Casting of Ti-811

None of the casting iterations results in full infiltration of the melt into the preform, this was due mainly to the limitations of the equipment which were not fully overcome. Chief among these limitations was control over the heating of the alloy, the alloy and preform location did not allow for the Ti-811 to be melted separately then poured into the preform in the liquid state. Replacing the quartz with BN solved the issues with crucible stability but prevented the viewing alloy and preform during the melting process. This observation of the during the melting process offered a very limited level of control, this control was removed when the crucible changed, and impacted the quality of the infiltration produced. A larger induction heating coil would have allowed for a larger mass of alloy and preform to be heated, increasing the available liquid and preheated preform form infiltration. Further study into the use of the vacuum furnace and novel crucible preform and alloy location design may have resulted in greater levels of infiltration that seem in the induction melting process. The ideal equipment for this type of infiltration casting operation would be a vacuum induction heath with temperature measurement for melting larger (100-500 g) quantities of Ti-811, with the ability to pour the molten alloy into a preheated mould containing the preform. This would increase the level control of the melting and casting so that the focus could shift to the production, control and testing of the porous metal produced.

6   CONCLUSIONS

The aim of this thesis was to investigate the current materials and methods used in the production of porous metals (metal foams), and how they may be improved and adapted to meet the needs of processing metals with higher (>1000°C) melting point. The objectives that were set were to:

- Investigate current and novel porous metal manufacturing methods.
- Select at least one method which could be used directly or modified for use with a high temperature metal.
- Produce porous metal samples using the methods selected, and select appropriate testing methods to characterise the porous metal produced.

The first objective was fully achieved, the second was achieved with two methods selected. The use of selective phase removal using a nickel-copper alloy produced porous structures which could be characterised even though a large enough sample was not produced for mechanical testing. The use of infiltration casting of Ti-811 into an $NaAlO_2$ was in hindsight a high-risk selection given the available in-house equipment and this work details the development process as the objective of producing any testable porous samples was not achieved.

Detailed conclusions for the work presented in this thesis are separated into the two themes of the work, with Chapter 4 focusing on the production and characterisation of a porous metal produced by selective phase removal and Chapter 5 discussing the process development and evolution of a method for infiltration casting a high melting temperature titanium alloy in order to produce a porous structure.

6.1 Selective Phase Removal in a Nickel-Copper Binary Alloy

- The binary nickel-copper alloy system selected are suitable to provide a two phase microstructure. This microstructure was manipulated through the use of different solidification schedules and heat treatment. This was confirmed using both EDS point analysis and EDS area mapping.

- A method has been applied for the successful preferential removal of the selected phase within the binary alloy to produce a porous structure.

- The microstructure of the alloy has been manipulated to change the measured porosity, when cooled slowly the porosity produced was 52%. Solidifying the alloy rapidly increased the porosity to 57%, with a subsequent heat treatment the porosity was further increased to 60%.

- The microstructural modifications have resulted in changes to the size of the pores produced. Where a slow cooled regime has been applied a greater amount of solute partitioning has resulted in larger concentrations of copper rich regions forming which on removal have produced larger pores. The size of the pores present in the alloy having under gone rapid cooling has been measured and the sample further processed through heat treatment in order to enlarge them. This proved that further diffusion and separation of the two phases was possible after initial solidification.

- The hardness of the produced porous sample has been tested and follows the trends observed from the physical structures produced, with the hardness also varying in accordance with the pore size, lager pores have a courser surround structure which results in a stronger structure.

- The structure and depth of the produced porosity has been investigated, with all solidification regimes producing complex interconnected networks of pores in three dimensions.

The ability to produce a porous structure in a bulk solid after it has been processed and shaped into a component has the potential to open up a large number of exciting potential uses and it overcomes the difficulty in joining a porous structure to a bulk structure. The component can provide its own mechanical strength from a bulk center with the surface porous and functional. It may be possible to produced grade porosity by introducing localised differences in heat treatment parameters.

6.2 Infiltration Casting of High Melting Temperature Alloy

- A preform material and alloy combination were selected which showed required compatibility in melting temperatures above 1000°C. The sodium aluminate meets the requirement that it can be removed by means of its solubility in water, it is also stable at high enough temperatures for the casting of Ti-811 alloy.

- It has been demonstrated that sodium aluminate can be processed into the required size and shape to act as an infiltration casting preform.

- Arc melter and suction casting has been used to melt and infiltrate Ti-811 alloy into a sodium aluminate preform which was subsequently removed to produce a porous sample. This sample showed good infiltration into the center created a definite but limited internal pore network.

- Induction melting equipment was used to overcome the size limitations of the arc melting equipment, to produce large porous sample via infiltration casting. Two crucible materials were trialed with the induction melting equipment, quartz was used initially but proved unsuitable due to the softening temperature of the quartz being similar to that of the liquidus temperature of Ti-811 alloy. The second material to be trialed was boron nitride, this proved to be able to withstand the high temperature required.

- Processing parameters were refined over a series of iterations until the produced castings showed extensive signs of infiltration in the preform material, with larger pores than those produced in the arc melter. The casting parameters used unfortunately did not produce what could be considered a porous metal casting.

- An alternative method of applying the pressure required for infiltration was trialed, the use of a tungsten cylinder place onto the alloy before melting. This method was successful in overcoming the short comings of using a gas jet, and provided a more even distribution of pressure.

- The use a vacuum furnace was trailed as an alternative method of melting the alloy in combination with the tungsten cylinder to apply pressure. However, this only resulted in superficial infiltration into the preform material.

Infiltration casting of high temperature metals if it can be perfected will open up a lower cost route of production and given design engineers a material whose density can be tailored (through the preform) and in turn the mechanical properties can be tailored. With the benefits of the higher operation service temperatures than the currently available porous aluminium, and lower cost than the currently additively manufactured methods used.

7 FURTHER WORK AND RECOMMENDATIONS

7.1 Selective Phase Removal in a Nickel-Copper Binary Alloy

- In order to investigate the extent that the porosity can be controlled through phase separation on solidification, strict solidification regimes should be used in order to find the maximum and minimal relative porosity and pore size that can be produced from this alloy composition.

- Investigations of directionally solidified alloys.

- A range of alloy compositions processed using the same conditions would allow for the investigation into the limits of potential porous structures that can be produced. By combining different solidification regimes, a large degree of control may be possible.

- The limits of the etching method used need to be established in order to find the maximum size that a fully porous structure can be produced.

- Further testing of the mechanical and physical properties of the porous materials produced to identify potential uses.

- Finally, investigations into this alloys ability to undergo spinodally decomposition, the alloy shows has the characteristic required. If this can be proved to be present or induced it opens the possibly up for multi scale porosity, with the large macrostructure of pores from dealloying or nano porosity on its surface from spinodal decomposition.

7.2 Infiltration Casting of Ti-811

- Change the heating method to a more vacuum induction melting with casting ability to enable larger quantities of alloy at consist temperatures to be used.

- Large sized samples are needed for mechanical testing to assess the properties of the produced porous metals with the goal of identifying a use for a high temperature low mass structure.

- Once the parameters are refined and consistent samples can be produced the chemical effect of the sodium aluminate on the titanium alloy must be further investigated.

- Work is required on the preform material with respect to complexity of preform geometries can that be produced in sodium aluminate.

- A full study of the use of a vacuum furnace as the heat source as this will add the temperature control required for the production of large scale items.

An important outcome of this work is the idea that it would be possible to combine the two methods presented and infiltration cast a copper nickel binary alloy, remove the perform and then process that porous metal again. This could potentially produce a structure with porosity across a wide range of scales.

8 REFERENCES

[1]   Gibson LJ. Mechanical behavior of metallic foams. Annu. Rev. Mater. Sci. 2000;30:191.

[2]   CES Selector. GRANTA, 2017.

[3]   Castro G, Nutt SR. Synthesis of syntactic steel foam using mechanical pressure infiltration. Mater. Sci. Eng. A-Struct. Mater. Prop. Microstruct. Process. 2012;535:274.

[4]   Banhart J. Aluminium foams for lighter vehicles. Int. J. Veh. Des. 2005;37:114.

[5]   Miyoshi T, Itoh M, Akiyama S, Kitahara A. ALPORAS aluminum foam: Production process, properties, and applications. Advanced Engineering Materials 2000;2:179.

[6]   Dobesberger F, Flankl HJ, Leitlmeier D, Flankl H. Metal molded body useful in crumple zone of automobiles, consists of metallically connected areas from metal foam, metal and insert elements with higher melting point than base material of the metal foam and metal. Hutte Klein Reichenbach Gmbh, Dobesberger F,Flankl H J, Leitlmeier D. p.2046519.

[7]   Bansiddhi A, Sargeant T, Stupp S, Dunand D. Porous NiTi for bone implants: A review. Acta Biomaterialia 2008;4:773.

[8]   Akiyama S, Ueno H, Imagawa K, Kitahara A, Nagata S, Morimoto K, Nishikawa T, Itoh M. Foamed metal, esp. aluminium(alloy) - useful as sound absorbing and electromagnetic shielding material. Agency of Ind Sci & Technology (Agen) Shinko Wire Co Ltd (Shia). p.210803.

[9]   Saadatfar M, Garcia-Moreno F, Hutzler S, Sheppard AP, Knackstedt MA, Banhart J, Weaire D. Imaging of metallic foams using X-ray micro-CT. Colloids and Surfaces A: Physicochemical and Engineering Aspects 2009;344:107.

[10]   Bock J, Jacobi AM. Geometric classification of open-cell metal foams using X-ray micro-computed tomography. Materials Characterization 2013;75:35.

[11]   Masso-Moreu Y, Mills NJ. Impact compression of polystyrene foam pyramids. International Journal of Impact Engineering 2003;28:653.

[12]   Jiang L, Xiao H, An W, Zhou Y, Sun J. Correlation study between flammability and the width of organic thermal insulation materials for building exterior walls. Energy and Buildings 2014;82:243.

[13]   Barrios M, Van Sciver SW. Thermal conductivity of rigid foam insulations for aerospace vehicles. Cryogenics 2013;55–56:12.

[14]   Baumeister J, Banhart J, Weber M. Aluminium foams for transport industry. Materials & Design 1997;18:217.

[15]   Ashby M. Metal Foams: A Design Guide: Butterworth-Heinemann, 2000.

[16]   Banhart J. Manufacture, characterisation and application of cellular metals and metal foams. Prog. Mater. Sci. 2001;46:559.

[17]   Salimon A, Brechet Y, Ashby MF, Greer AL. Selection of applications for a material. Advanced Engineering Materials 2004;6:249.

[18]   Banhart J. Light-Metal Foams - History of Innovation and Technological Challenges. Advanced Engineering Materials 2013;15:82.

[19]   Banhart J, Seeliger HW. Aluminium Foam Sandwich Panels: Metallurgy, Manufacture and Applications. Lancaster: Destech Publications, Inc, 2008.

[20]   Davies GJ, Zhen S. Metallic Foams - Their Production, Properties and Applications. Journal of Materials Science 1983;18:1899.

[21]   Simone AE, Gibson LJ. Aluminum foams produced by liquid-state processes. Acta Mater. 1998;46:3109.

[22]   Byakova A, Bezim'yanny Y, Gnyloskurenko S, Nakamura T. Fabrication Method for Closed-cell Aluminium Foam with Improved Sound Absorption Ability. Procedia Materials Science 2014;4:13.

[23]   Mukherjee M, Ramamurty U, Garcia-Moreno F, Banhart J. The effect of cooling rate on the structure and properties of closed-cell aluminium foams. Acta Mater. 2010;58:5031.

[24]   Mukherjee M, Garcia-Moreno F, Banhart J. Collapse of Aluminum Foam in Two Different Atmospheres. Metall. Mater. Trans. B-Proc. Metall. Mater. Proc. Sci. 2010;41:500.

[25]   Haesche M, Lehmhus D, Weise J, Wichmann M, Mocellin ICM. Carbonates as Foaming Agent in Chip-based Aluminium Foam Precursor. J. Mater. Sci. Technol. 2010;26:845.

[26]   Gergely V, Curran DC, Clyne TW. The FOAMCARP process: foaming of aluminium MMCs by the chalk-aluminium reaction in precursors. Composites Science and Technology 2003;63:2301.

[27]   Papadopoulos DP, Omara H, Stergioudi F, Tsipas SA, Michailidis N. The use of dolomite as foaming agent and its effect on the microstructure of aluminium metal foams-Comparison to titanium hydride. Colloid Surf. A-Physicochem. Eng. Asp. 2011;382:118.

[28]   Gergely V, Clyne B. The FORMGRIP process: Foaming of reinforced metals by gas release in precursors. Advanced Engineering Materials 2000;2:175.

[29]   Du H, Song G, Nakajima H, Zhao Y, Xiao J, Xiong T. Study on lotus-type porous copper electroplated with a Ni coating on inner surface of pores. Applied Surface Science 2013;264:772.

[30]   Liu X, Li X, Jiang Y, Xie J. Effect of casting temperature on porous structure of lotus-type porous copper. Procedia Engineering 2012;27:490.

[31]   Liu X-H, Liu X-F, Xie J-X. The Investigation of Fabrication Processing for Lotus-type Porous Magnesium by the In-situ Reaction and Unidirectional Solidification Method. Procedia Engineering 2012;36:270.

[32]   Nakajima H, Suzuki S. Fabrication of Lotus-type Porous Metals. In: Buschow KHJ, Cahn RW, Flemings MC, Ilschner B, Kramer EJ, Mahajan S, Veyssière P, editors. Encyclopedia of Materials: Science and Technology (Second Edition). Oxford: Elsevier, 2010. p.1.

[33]   Kashihara M, Yonetani H, Kobi T, Hyun SK, Suzuki S, Nakajima H. Fabrication of lotus-type porous carbon steel via continuous zone melting and its mechanical properties. Materials Science and Engineering: A 2009;524:112.

[34]   Alvarez K, Sato K, Hyun SK, Nakajima H. Fabrication and properties of Lotus-type porous nickel-free stainless steel for biomedical applications. Materials Science and Engineering: C 2008;28:44.

[35]   Mori K. Finite element simulation of powder forming and sintering. Comput. Meth. Appl. Mech. Eng. 2006;195:6737.

[36]   Olevsky EA, Tikare V, Garino T. Multi-scale study of sintering: A review. J. Am. Ceram. Soc. 2006;89:1914.

[37]   Maximenko AL, Olevsky EA. Effective diffusion coefficients in solid-state sintering. Acta Mater. 2004;52:2953.

[38]   Pan J, Le H, Kucherenko S, Yeomans JA. A model for the sintering of spherical particles of different sizes by solid state diffusion. Acta Mater. 1998;46:4671.

[39]   Ashby MF. First Report on Sintering Diagrams. Acta Metallurgica 1974;22:275.

[40]   Oh IH, Nomura N, Masahashi N, Hanada S. Mechanical properties of porous titanium compacts prepared by powder sintering. Scr. Mater. 2003;49:1197.

[41]   Nomura N, Kohama T, Oh IH, Hanada S, Chiba A, Kanehira M, Sasaki K. Mechanical properties of porous Ti–15Mo–5Zr–3Al compacts prepared by powder sintering. Materials Science and Engineering: C 2005;25:330.

[42]   Ryan G, Pandit A, Apatsidis DP. Fabrication methods of porous metals for use in orthopaedic applications. Biomaterials 2006;27:2651.

[43]   Mondal DP, Patel M, Das S, Jha AK, Jain H, Gupta G, Arya SB. Titanium foam with coarser cell size and wide range of porosity using different types of evaporative space holders through powder metallurgy route. Materials & Design 2014;63:89.

[44]   Hassani A, Habibolahzadeh A, Bafti H. Production of graded aluminum foams via powder space holder technique. Materials & Design 2012;40:510.

[45]   Torres Y, Pavón J, Trueba P, Cobos J, Rodriguez-Ortiz JA. Design, Fabrication and Characterization of Titanium with Graded Porosity by using Space-holder Technique. Procedia Materials Science 2014;4:110.

[46]   Ye B, Dunand DC. Titanium foams produced by solid-state replication of NaCl powders. Mater. Sci. Eng. A-Struct. Mater. Prop. Microstruct. Process. 2010;528:691.

[47]   Conde Y, Despois JF, Goodall R, Marmottant A, Salvo L, San Marchi C, Mortensen A. Replication Processing of Highly Porous Materials. Advanced Engineering Materials 2006;8:795.

[48]   Gaillard C, Despois JF, Mortensen A. Processing of NaCl powders of controlled size and shape for the microstructural tailoring of aluminium foams. Materials Science and Engineering: A 2004;374:250.

[49]   Yamada Y, Shimojima K, Sakaguchi Y, Mabuchi M, Nakamura M, Asahina T, Mukai T, Kanahashi H, Higashi K. Processing of cellular magnesium materials. Advanced Engineering Materials 2000;2:184.

[50]   Yamada Y, Shimojima K, Sakaguchi Y, Mabuchi M, Nakamura M, Asahina T, Mukai T, Kanahashi H, Higashi K. Processing of an open-cellular AZ91 magnesium alloy with a low density of 0.05 g/cm(3). Journal of materials science letters 1999;18:1477.

[51]   Wen CE, Mabuchi M, Yamada Y, Shimojima K, Chino Y, Asahina T. Processing of biocompatible porous Ti and Mg. Scr. Mater. 2001;45:1147.

[52]   Manonukul A, Muenya N, Léaux F, Amaranan S. Effects of replacing metal powder with powder space holder on metal foam produced by metal injection moulding. Journal of Materials Processing Technology 2010;210:529.

[53]   Shimizu T, Matsuzaki K, Nagai H, Kanetake N. Production of high porosity metal foams using EPS beads as space holders. Materials Science and Engineering: A 2012;558:343.

[54]   Esen Z, Bor S. Processing of titanium foams using magnesium spacer particles. Scr. Mater. 2007;56:341.

[55]   Kotan G, Bor AS. Production and characterization of high porosity Ti-6Al-4V foam by space holder technique in powder metallurgy. Turkish Journal of Engineering and Environmental Sciences 2007;31:149.

[56]   Wen CE, Yamada Y, Shimojima K, Chino Y, Hosokawa H, Mabuchi M. Novel titanium foam for bone tissue engineering. Journal of Materials Research 2002;17:2633.

[57]   Imwinkelried T. Mechanical properties of open-pore titanium foam. Journal of Biomedical Materials Research Part A 2007;81A:964.

[58]   Mansourighasri A, Muhamad N, Sulong AB. Processing titanium foams using tapioca starch as a space holder. Journal of Materials Processing Technology 2012;212:83.

[59]   Materialise. Software for additive manufacturing. Materialise.

[60]   Li JP, de Wijn JR, Van Blitterswijk CA, de Groot K. Porous Ti6Al4V scaffold directly fabricating by rapid prototyping: Preparation and in vitro experiment. Biomaterials 2006;27:1223.

[61]   Kim TB, Yue S, Zhang Z, Jones E, Jones JR, Lee PD. Additive manufactured porous titanium structures: Through-process quantification of pore and strut networks. Journal of Materials Processing Technology 2014;214:2706.

[62]   Mellor S, Hao L, Zhang D. Additive manufacturing: A framework for implementation. International Journal of Production Economics 2014;149:194.

[63]   Heinl P, Müller L, Körner C, Singer RF, Müller FA. Cellular Ti–6Al–4V structures with interconnected macro porosity for bone implants fabricated by selective electron beam melting. Acta Biomaterialia 2008;4:1536.

[64]   Li X, Wang L, Yu X, Feng Y, Wang C, Yang K, Su D. Tantalum coating on porous Ti6Al4V scaffold using chemical vapor deposition and preliminary biological evaluation. Materials Science and Engineering: C 2013;33:2987.

[65]   van Grunsven W, Hernandez-Nava E, Reilly G, Goodall R. Fabrication and Mechanical Characterisation of Titanium Lattices with Graded Porosity. Metals 2014;4:401.

[66]   Quadbeck P, Kümmel K, Hauser R, Standke G, Adler J, Stephani G, Kieback B. Structural and Material Design of Open-Cell Powder Metallurgical Foams. Advanced Engineering Materials 2011;13:1024.

[67]   Olurin OB, Wilkinson DS, Weatherly GC, Paserin V, Shu J. Strength and ductility of as-plated and sintered CVD nickel foams. Composites Science and Technology 2003;63:2317.

[68]   Levine BR, Sporer S, Poggie RA, Della Valle CJ, Jacobs JJ. Experimental and clinical performance of porous tantalum in orthopedic surgery. Biomaterials 2006;27:4671.

[69]   Jiang M, Zhu D, Zhao X. Electrolysis of ammonia for hydrogen production catalyzed by Pt and Pt-Ir deposited on nickel foam. Journal of Energy Chemistry 2014;23:1.

[70]   Antenucci A, Guarino S, Tagliaferri V, Ucciardello N. Improvement of the mechanical and thermal characteristics of open cell aluminum foams by the electrodeposition of Cu. Materials & Design 2014;59:124.

[71]   Jung A, Lach E, Diebels S. New hybrid foam materials for impact protection. International Journal of Impact Engineering 2014;64:30.

[72]   Murphy M. Electrodeposited metals: Nickel and nickel alloys. Metal Finishing 1995;93:34.

[73]   Murphy M. Electrodeposited metals: Copper and copper alloys. Metal Finishing 1995;93:33.

[74]   Tian Q-h, Guo X-y. Electroless copper plating on microcellular polyurethane foam. Transactions of Nonferrous Metals Society of China 2010;20, Supplement 1:s283.

[75]   Yang W, Luo S, Zhang B, Huang Z, Tang X. Electroless preparation and characterization of magnetic Ni–P plating on polyurethane foam. Applied Surface Science 2008;254:7427.

[76]   van Drunen J, Napporn TW, Kokoh B, Jerkiewicz G. Electrochemical oxidation of isopropanol using a nickel foam electrode. Journal of Electroanalytical Chemistry 2014;716:120.

[77]   Santos VEO, Celante VG, Lelis MFF, Freitas MBJG. Chemical and electrochemical recycling of the nickel, cobalt, zinc and manganese from the positives electrodes of spent Ni–MH batteries from mobile phones. J. Power Sources 2012;218:435.

[78]   Zhang C, Li J, Hu Z, Zhu F, Huang Y. Correlation between the acoustic and porous cell morphology of polyurethane foam: Effect of interconnected porosity. Materials & Design 2012;41:319.

[79]   Dressler M, Reinsch S, Schadrack R, Benemann S. Burnout behavior of ceramic coated open cell polyurethane (PU) sponges. Journal of the European Ceramic Society 2009;29:3333.

[80]   Corp EA. Duocel Foam vol. 2013, 2013.

[81]   Brothers AH, Dunand DC. Density-graded cellular aluminum. Advanced Engineering Materials 2006;8:805.

[82]   Nieh TG, Higashi K, Wadsworth J. Effect of cell morphology on the compressive properties of open-cell aluminum foams. Mater. Sci. Eng. A-Struct. Mater. Prop. Microstruct. Process. 2000;283:105.

[83]   Brothers A, Scheunemann R, Defouw J, Dunand D. Processing and structure of open-celled amorphous metal foams. Scr. Mater. 2005;52:335.

[84]   Rugolo J, Erlebacher J, Sieradzki K. Length scales in alloy dissolution and measurement of absolute interfacial free energy. Nature Materials 2006;5:946.

[85]   Erlebacher J, Aziz MJ, Karma A, Dimitrov N, Sieradzki K. Evolution of nanoporosity in dealloying. Nature 2001;410:450.

[86]   Sun Y, Balk TJ. A multi-step dealloying method to produce nanoporous gold with no volume change and minimal cracking. Scr. Mater. 2008;58:727.

[87]   Hayes JR, Hodge AM, Biener J, Hamza AV, Sieradzki K. Monolithic nanoporous copper by dealloying Mn?Cu. Journal of Materials Research 2006;21:2611.

[88]   Li HX, Hao XJ, Zhao G, Hao SM. Characteristics of the continuous coarsening and discontinuous coarsening of spinodally decomposed Cu-Ni-Fe alloy. Journal of Materials Science 2001;36:779.

[89]   Mozingo R. Catalyst, Raney nickel. Org. Synth 1941;21:15.

[90]   Tian H, Zhao H, Cao X. Catalytic transfer hydrogenation of 7-ketolithocholic acid to ursodeoxycholic acid with Raney nickel. Journal of Industrial and Engineering Chemistry 2013;19:606.

[91]   Chang N-S, Aldrett S, Holtzapple MT, Davison RR. Kinetic studies of ketone hydrogenation over Raney nickel catalyst. Chemical Engineering Science 2000;55:5721.

[92]   Wilson BP, Lavery NP, Jarvis DJ, Anttila T, Rantanen J, Brown SGR, Adkins NJ. Life cycle assessment of gas atomised sponge nickel for use in alkaline hydrogen fuel cell applications. J. Power Sources 2013;243:242.

[93]   Depo JK, Okido M, Capuano GA, Harris R. The Preparation of Modified Raney Alloys for Electrolysis Production of Hydrogen. Can. Metall. Q. 1994;33:369.

[94]   Rodella CB, Kellermann G, Francisco MSP, Jordao MH, Zanchet D. Textural and Structural Analyses of Industrial Raney Nickel Catalyst. Ind. Eng. Chem. Res. 2008;47:8612.

[95]   Terentyuk GS, Maksimova IL, Dikht NI, Terentyuk AG, Khlebtsov BN, Khlebtsov NG, Tuchin VV. 22 - Cancer laser therapy using gold nanoparticles. In: Jelínková H, editor. Lasers for Medical Applications. Woodhead Publishing, 2013. p.659.

[96]   Jing L, Liang X, Deng Z, Feng S, Li X, Huang M, Li C, Dai Z. Prussian blue coated gold nanoparticles for simultaneous photoacoustic/CT bimodal imaging and photothermal ablation of cancer. Biomaterials 2014;35:5814.

[97]   Khlebtsov BN, Khanadeev VA, Panfilova EV, Inozemtseva OA, Burov AM, Khlebtsov NG. A simple Mie-type model for silica-coated gold nanocages. Journal of Quantitative Spectroscopy and Radiative Transfer 2013;121:23.

[98]   Feis A, Gellini C, Salvi PR, Becucci M. Photoacoustic excitation profiles of gold nanoparticles. Photoacoustics 2014;2:47.

[99]   Haruta M. New Generation of Gold Catalysts: Nanoporous Foams and Tubes—Is Unsupported Gold Catalytically Active? ChemPhysChem 2007;8:1911.

[100]   Jenei P, Choi H, Tóth A, Choe H, Gubicza J. Mechanical behavior and microstructure of compressed Ti foams synthesized via freeze casting. Journal of the Mechanical Behavior of Biomedical Materials 2016;63:407.

[101]   Hao GL, Han FS, Li WD. Processing and mechanical properties of magnesium foams. Journal of Porous Materials 2008;16:251.

[102]   Ryan GE, Pandit AS, Apatsidis DP. Porous titanium scaffolds fabricated using a rapid prototyping and powder metallurgy technique. Biomaterials 2008;29:3625.

[103]   Ozdemir Z, Hernandez-Nava E, Tyas A, Warren JA, Fay SD, Goodall R, Todd I, Askes H. Energy absorption in lattice structures in dynamics: Experiments. International Journal of Impact Engineering 2016;89:49.

[104]   Liu H, Wei J, Qu Z. Prediction of aerodynamic noise reduction by using open-cell metal foam. Journal of Sound and Vibration 2012;331:1483.

[105]   Zhao CY. Review on thermal transport in high porosity cellular metal foams with open cells. International Journal of Heat and Mass Transfer 2012;55:3618.

[106]   Wang W, Burgueño R, Hong J-W, Lee I. Nano-deposition on 3-D open-cell aluminum foam materials for improved energy absorption capacity. Materials Science and Engineering: A 2013;572:75.

[107]   Salimon A, Brechet Y, Ashby MF, Greer AL. Potential applications for steel and titanium metal foams. Journal of Materials Science 2005;40:5793.

[108]   Singh R, Lee PD, Jones JR, Poologasundarampillai G, Post T, Lindley TC, Dashwood RJ. Hierarchically structured titanium foams for tissue scaffold applications. Acta Biomaterialia 2010;6:4596.

[109]   Caruso G, Naviglio A, Principi P, Ruffini E. High-energy efficiency desalination project using a full titanium desalination unit and a solar pond as the heat supply. Desalination 2001;136:199.

[110]   Wang SH, Peng J, Lui WB. Surface modification and development of titanium bipolar plates for PEM fuel cells. J. Power Sources 2006;160:485.

[111]   Wang SH, Peng J, Lui WB, Zhang JS. Performance of the gold-plated titanium bipolar plates for the light weight PEM fuel cells. J. Power Sources 2006;162:486.

[112]   K.E.Easterling DAPa. Phase Transformations in metals and alloys: Taylor & Francis, 1992.

[113] Iakubov IT, Khrapak AG, Pogosov VV, Trigger SA. The surface tension of liquid metals and its temperature dependence. Solid State Communications 1985;56:709.

[114] Egry I, Ricci E, Novakovic R, Ozawa S. Surface tension of liquid metals and alloys — Recent developments. Advances in Colloid and Interface Science 2010;159:198.

[115] Miller MK, Hyde JM, Hetherington MG, Cerezo A, Smith GDW, Elliott CM. Spinodal Decomposition in Fe-Cr Alloys, Experimental Study at the Atomic Level and Comparison with Computer Models. 1. Introduction and Methodology. Acta Metall. Mater. 1995;43:3385.

[116] Findik F. Sidebands in spinodal Cu-Ni-Cr alloys and lattice parameters inquiries. Journal of materials science letters 1993;12:338.

[117] Boonyongmaneerat Y, Dunand DC. Ni-Mo-Cr Foams Processed by Casting Replication of Sodium Aluminate Preforms. Advanced Engineering Materials 2008;10:379.

[118] NPL. Hygrometry. Kaye & Laby, 2011.

[119] Higginson RL. Worked examples in quantitative metallography: London : Maney, 2003 2003.

[120] Committees AIAPDaH. Alloy Phase Diagrams: Metals Handbook: ASM International, 1992.

[121] Zhu J, Kamiya A, Yamada T, Shi W, Naganuma K, Mukai K. Surface tension, wettability and reactivity of molten titanium in Ti/yttria-stabilized zirconia system. Mater. Sci. Eng. A-Struct. Mater. Prop. Microstruct. Process. 2002;327:117.

[122] R.Boyer. Materials Properies Handbook: Titanium Alloys: ASM International, 1993.